MODELING OF MACHINING USING A COMBINED FINITE ELEMENT (FE) AND SMOOTHED PARTICLE HYDRODYNAMICS (SPH) METHOD.

by

Nishant Ojal

A dissertation submitted to the faculty of
The University of North Carolina at Charlotte
in partial fulfillment of the requirements
for the degree of Doctor of Philosophy in
Mechanical Engineering

Charlotte

2021

Approved by:

_____
Dr. Harish P. Cherukuri

_____
Dr. Ronald E. Smelser

_____
Dr. Alireza Tabarraei

_____
Dr. Shen-En Chen

LLNL-TH-823882

ABSTRACT

NISHANT OJAL. Modeling of machining using a combined Finite Element (FE) and Smoothed Particle Hydrodynamics (SPH) method.. (Under the direction of DR. HARISH P. CHERUKURI)

In this thesis, a combined approach based on the Finite Element (FE) and Smoothed Particle Hydrodynamics (SPH) methods is proposed to model turning operations. The approach exploits the advantages of each method and leads to high-fidelity coupled FE-SPH machining models that are significantly more numerically efficient and are on par with the models based on each of the two methods alone. Both two-dimensional and three-dimensional models are developed and validated by comparing predicted forces and chip morphologies with experimental results. Parametric studies are carried out to fine-tune the model-based parameters in order to avoid numerical stability issues. The three-dimensional models are extended to included modulated tool path (MTP) machining which is a technique for breaking chips during machining by modulating the motion of the tool. The MTP model predictions are shown to agree with the results from an existing analytical model. With this model, various tool paths can be simulated to choose an optimal path that decreases tool-wear without sacrificing productivity. Preliminary results from a three-dimensional turning model incorporating machining dynamics through a spring-damper system are also presented. This model has the potential to be used for studying machining stability for a given set of machining conditions.

Another significant contribution of this thesis is the determination of Johnson-Cook material model parameters for a given material using an inverse method and experimental values of cutting forces and workpiece temperatures. The methodology described in the present work identifies the non-uniqueness of the solution to the inverse problem and proposes an approach that eliminates the non-uniqueness.

ACKNOWLEDGEMENTS

I express my sincere gratitude to my advisor Dr. Harish P. Cherukuri, for mentoring me throughout this work. His persistent encouragement and confidence in me motivated me to move forward. Blessed with his vast knowledge, I enjoyed the opportunities to fly freely. I sincerely acknowledge his constant support and guidance. I would like to thank Dr. Ronald E. Smelser, Dr. Alireza Tabarraei and Dr. Shen-En Chen for serving on my dissertation committee and providing valuable inputs.

I also thank Dr. Tony L. Schmitz and Dr. Ryan Copenhaver for sharing their experimental work and fruitful discussions. I would like to extend my appreciation to Brian Dutterer for training me to operate conventional and CNC machines.

I am extremely grateful to Adam Wayne Jaycox, Kyle Thomas Devlugt, and Kyle S. Beith, who devoted their precious time and shared immense experience. Their feedback during the reviews offered deep insight into this study. They also supported by sharing the data of the experiments conducted at LLNL. I would like to acknowledge the Department of Mechanical engineering and Engineering Science of UNC Charlotte and Lawrence Livermore National Laboratory for their support during this work. This work was performed under the auspices of the U.S. Department of Energy by Lawrence Livermore National Laboratory under Contract DE-AC52-07NA27344.

I am deeply grateful to Dr. Len Schwer, Dr. James M. Kennedy and Dr. Martin Madaj for their suggestions during the model development in LS-DYNA. Special thanks to Mr. Jonathan Halter for the changes suggested in running the simulations on high-performance computing clusters.

I would also like to thank my family and friends for their support. Special thanks to Chinmay, who introduced me to two-dimensional machining modeling using the SPH method. Finally, I would like to thank my labmates, Farjana, Kuldeep, Dhanooj, Maryam and Parth, who helped me throughout this journey.

TABLE OF CONTENTS

LIST OF TABLES

LIST OF FIGURES

CHAPTER 1: INTRODUCTION

Improvement of machining output through a better understanding of the relationship between input variables (such as tool geometry, material to be machined, etc.) and the output variables (such as cutting forces, temperature rise, tool wear, etc.) has been a subject of interest to the manufacturing industry. This becomes more pertinent for utilizing new materials. Both experimental and numerical studies are used to understand the complex physics of machining processes. However, experimental studies have disadvantages due to the difficulties in measuring many physical quantities of practical importance in the cutting zone [15] and also the cost involved [16] in conducting these experiments.

Finite Element Modeling is a numerical technique commonly used for modeling machining. Various approaches such as Lagrangian [17, 18], Eulerian [19] and Arbitrary Lagrangian-Eulerian [20] methods have been used for modelling the process. However, depending upon the approach used, challenges such as high mesh distortions, element deletion and prior prescription of the chip separation path are associated with the use of Finite Element (FE) mesh.

The Smoothed Particle Hydrodynamics (SPH) method eliminates the disadvantages associated with the finite element method because of the lack of physical connection between the particles used for discretizing the domain. Machining models using the SPH method have been developed by various researchers such as Limido et al. [21], Madaj et al. [22], Villumsen et al. [23] and Avachat et al. [24]. Besides proving the ability of the SPH method to model machining, these studies provide insight into the effect of the various process-based parameters and the numerical parameters (associated with the SPH method) on cutting forces, workpiece temperatures, etc.

1.1 Original features of dissertation

Following are the main contributions of this dissertation.

1. Turning operation is modeled using coupled SPH-FE models in two- and three-dimensions. The results of the comparative study for two-dimensional models show that the coupled SPH-FE models are significantly more numerically efficient. The simulation results are validated with experiments by comparing the cutting forces and chip profiles.

2. A detailed parametric study of method-based and process-based parameters has been conducted. This study provides an insight into the effect of various parameters on model predictions and is useful in developing a robust machining model.

3. Three-dimensional models of modulated tool path (MTP) turning operations has been developed. The results of MTP turning are compared with those of the conventional turning simulations, showing the advantages of MTP turning. The results of MTP simulation are validated with an analytical model.

4. Preliminary three-dimensional turning models incorporating machining dynamics through a spring-damper system are developed. These models can be used for studying machining stability for a given set of machining conditions.

5. Non-uniqueness of Johnson-Cook material model parameters using inverse approaches is identified and a solution is proposed to determine these parameters uniquely.

1.2 Dissertation organization

This section introduces the modeling of machining and the motivation behind this research.

Chapter 2 summarizes the relevant previous research carried out in this field. It briefly touches upon different analytical models and finite element formulations used by researchers and explains the advantages of the SPH method over these approaches. Then, it provides a summary of the work done by researchers for two-dimensional and three-dimensional machining modeling using the SPH method.

Next, Chapter 3 highlights the fundamentals of the SPH method, such as the particle approximations, discretization of the conservation equations and calculation algorithm.

In Chapter 4, a complete SPH model of two-dimensional machining is developed. The results of this model are validated with the work of Madaj et al. [22]. A coupled SPH-FE model of two-dimensional machining is also studied. The SPH-FE coupled model produces results that are in close agreement with those of the fully SPH model. However, the coupled model results in a reduction of 40% in simulation time.

A better understanding of SPH parameters through a parametric study is achieved in Chapter 5. The machining model developed in Chapter 4 is used for this study. The study provides a set of SPH parameters that are used in the subsequent works for a robust machining model.

In Chapter 6, based on the result of the validation of the coupled SPH-FE model and parametric study, a three-dimensional coupled SPH-FE machining model is developed. The results of the simulation are validated with machining experimental observations.

In Chapter 7, the modulated tool path (MTP) machining is simulated. The simulated results of the MTP machining are compared with the simulated results of the continuous feed turning simulation.

Dynamic elements such as spring and damper are included in the three-dimensional machining model in Chapter 8. The effect of these elements on the tool vibration and hence machining stability is studied in this chapter.

Chapter 9 studies the aspect of unique determination of the Johnson-Cook material model parameters using inverse methods. A combination of an inverse approach using the results of orthogonal machining experiments and tensile test experiments is proposed for the unique determination of the parameters.

Finally, the dissertation concludes in Chapter 10 with results from the study and the recommendations for future work. The Appendix provides detailed derivations of some of the SPH equations relevant to the simulations presented in this work.

CHAPTER 2: LITERATURE REVIEW

Machining is a term that covers a large collection of manufacturing processes designed to remove unwanted material from a workpiece, usually in the form of chips [25]. Experimental studies on machining date back to 19^{th} century. Cocquilhat [26] measured the work per unit volume required to remove material in drilling operations. Hartig [27] provided a comprehensive reference guide containing tabulated values of feeds and cutting speeds for machining metals. In the book "Mémoirs sur le Rabotage de Métaux", Tresca [28] provided detailed illustrations of metallic chips formed by a variety of metal cutting techniques.

2.1 Analytical models

Based on machining experiments, various investigators started developing analytical models by the end of the 19^{th} century. These models aimed to provide an understanding of the mechanism involved in machining and predict quantities such as the cutting forces and temperatures. The thin-shear zone model and thick-shear zone model are the two popularly used models for orthogonal machining. These models are based on the experimental observations that simple shearing is the primary deformation mode in metal cutting and assume the existence of a primary shear zone extending from the tool-tip to the workpiece surface ahead of the tool.

2.1.1 Thin-shear zone model

The thin-shear zone model, popularly known as Merchant's model, was developed and refined from the works of Ernst and Merchant [11] and Kobayashi and Thomsen [29]. This model idealized the shear zone as a single shear plane represented by line AB in Fig. 2.1. Various cutting forces of orthogonal machining can be calculated

using this model, given the machining conditions such as the tool's rake angle (α), cutting velocity, uncut chip thickness and material properties (shear angle ϕ). Using the assumption that the resultant force R on the chip applied at the shear plane is equal, opposite and collinear to the force applied to the chip at the tool chip interface, the Merchant's circle (shown in Fig. 2.2) was proposed. This is a convenient tool to analytically estimate various machining forces. In the diagram, F_C is the cutting force, F_T is the thrust force, F_S is the shear force in the shear plane, F_N is the normal force to the shear plane, F is the frictional force on the tool and N is the normal force on the tool.

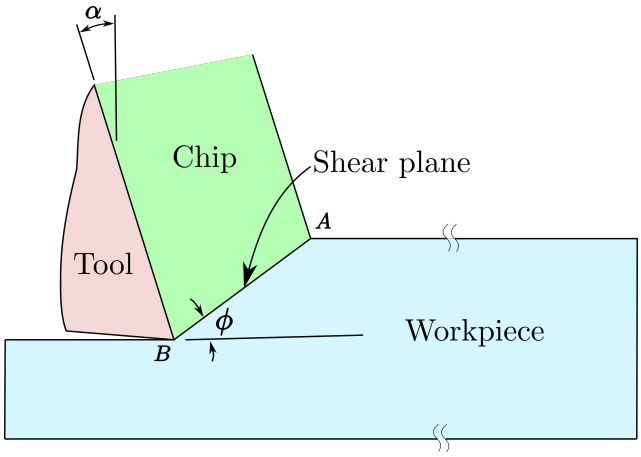

Figure 2.1: Shear plane in Thin-shear zone model [11].

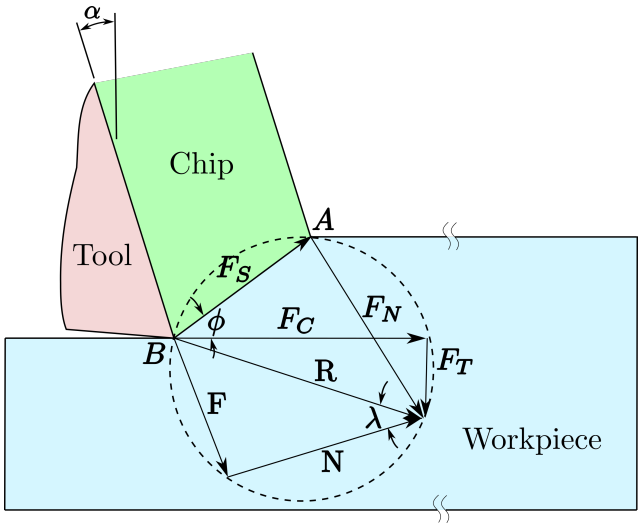

Figure 2.2: Merchant circle diagram [11].

2.1.2 Thick-shear zone model

There is a discontinuity of velocity at the shear plane of the thin-shear zone model. The workpiece enters the shear plane with the cutting velocity and exits with chip velocity. This discontinuity requires a shear velocity V_S along the shear plane AB. The experimental observations by Stevenson et al. [30] show that the deformation process involves a continuous change of velocities and the shear zone during machining does not agree with the thin-shear zone model. Based on the machining experiments at slow cutting speeds, the thick-shear zone model was proposed [31]. In the thick-shear zone model, a large plastic zone is proposed for continuous deformations. Also, the tool-chip contact occurred at some distance away from the tool edge and there is a gap between the tool and the chip on the tool edge side of the contact. The calculated stress field matched with the experimental evidence.

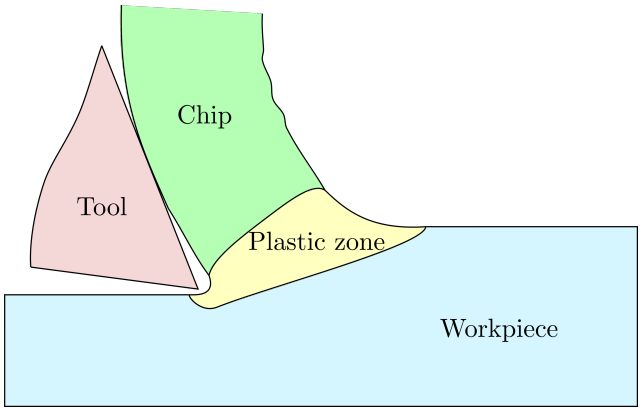

Figure 2.3: Thick shear machining model.

2.2 Finite element method

Analytical models have been used traditionally for quantitative modeling of machining. However, they are based on many assumptions, such as the existence of the shear plane in the thin-shear zone model. These assumptions lead to discrepancies between the predictions of the models and experimental observations. Also, the analytical models are usually limited to two dimensions. With the advancement in

computing, finite element methods have become useful for predicting the machining process outputs. Comprehensive reviews of finite element modeling for the machining process have been done by Arrazola et al. [32] and Sadeghifar et al. [15].

Three finite element formulations, namely Lagrangian, Eulerian, and Arbitrary Lagrangian-Eulerian (ALE) formulations, have been used by researchers for modeling machining. These formulations differ by the assignment of properties in the material coordinate system and spatial coordinate system.

2.2.1 Lagrangian formulation

In the Lagrangian formulation, the mesh is attached to the material. Hence all the properties assigned to the elements are in the material coordinate system. As machining progresses, the tool removes the material of the workpiece in the form of chips. The attached mesh also deforms along with the workpiece. Simulation of chips from the initial time to the steady-state is possible while using this formulation.

There are three major disadvantages of the Lagrangian formulation: high mesh distortions, multiple chip separation criteria, and prior prescription of chip separation path. High mesh distortion occurs in the cutting zone and results in the abnormal termination of the simulation. This is taken care of by using techniques such as pre-distorted meshes [1] and adaptive meshing [33]. Multiple chip separation criteria such as fracture energy criteria [1] and fracture based on maximum displacement [34] have been used in the literature. Also, a chip separation path needs to be prescribed, and the elements are deleted on that path based on the separation criteria. This leads to mass and energy loss, which affects the accuracy of the results.

2.2.2 Eulerian formulation

In the Eulerian formulation, the mesh is fixed in space. The properties under analysis are calculated at these fixed locations as the material flows through the mesh. This spatially fixed mesh eliminates the high mesh distortions observed in

the Lagrangian formulation. However, prior knowledge or assumption of a steady-state mesh configuration is required for the simulation. For example, a steady-state chip geometry needs to be defined for modeling machining [19]. This is a major disadvantage of the Eulerian formulation. The chip geometry is assumed based on the experimental observations or analytical models. Also, the Eulerian formulations cannot simulate serrated and discontinuous chip formation [35].

2.2.3 Arbitrary Lagrangian Eulerian (ALE) formulation

Arbitrary Lagrangian-Eulerian (ALE) formulation combines the advantages of Lagrangian and Eulerian formulation. In this method, a Lagrangian step is followed by an Eulerian step. In the Lagrangian step, the mesh flows with the material. Hence, the chip formation is the result of material deformation. In the following Eulerian step, the results of the Lagrangian step are interpolated onto a new mesh. This remap compensates for the mesh distortions during deformation. However, the computational cost is added due to the Eulerian step. Also, the remapping of state variables adds to the inaccurate results [16, 36].

2.3 Smoothed Particle Hydrodynamics method

Due to the disadvantages associated with the FEM formulations, the smoothed particle hydrodynamics method (SPH) [37] has attracted the attention of many researchers as an alternative. The SPH method is a Lagrangian, particle-based, meshless method and has several advantages over the grid-based approaches. High strains occurring in machining are easily modeled due to the meshless nature of the method. Particles undergoing deformation move without any topological restrictions. Furthermore, a separation model is not required in the SPH method with the relative motion of the particles with respect to each other and with respect to the tool creating a "natural" chip-workpiece separation.

2.3.1 2D machining model

Orthogonal machining using SPH has been studied by various researchers. One of the first orthogonal machining models using the SPH method was developed by Heinstein and Segalman [38]. Simulations were done for the Aluminum 6061-T6 workpiece with different depth of cut of machining and rake angles of the tool. The study concluded that the SPH method is a promising tool for modeling machining in overcoming the difficulties encountered while using FEM, such as mesh distortion and material separation.

Limido et al. [21] compared the results of a 2D orthogonal machining SPH model with the model generated using commercial package AdvantEdge and experiments. The study aimed to explore the advantages of SPH, namely the meshless nature for handling high strains, chip workpiece separation and modeling of friction as particle interaction. Chip morphology and cutting forces are the validation criteria. The SPH model could predict continuous and shear localized chips and all the steps of their formation. The tangential cutting force and normal cutting force respectively are within 10% and 30% of the measured values.

Espinosa et al. [39] modeled 2D orthogonal cutting and 3D oblique cutting using SPH and compared the predicted chip morphology and cutting forces with the experiments. Smooth variation of the von Mises stress is observed when the artificial viscosity was changed from the default value to 0.5. Also, the renormalized formulation resulted in a more realistic prediction of chip shape.

Villumsen et al. [23] developed an orthogonal cutting model of AL 6082-T6 in LS-DYNA using SPH. A detailed setup of the model in LS-DYNA is provided in the paper. Sensitivity analysis to evaluate the model is performed. SPH parameters, namely particle resolution (observed affecting the convergence of result), mass scaling (concluded as not an adequate way to reduce calculation time), process time scaling (concluded as effective with the reasonable assumption for analysis) and friction (ob-

served that forces increase with an increase in the friction coefficient) significantly affected force output. Chip formation and obtained force output are found to be in good agreement with the experimental results.

Schwer [3] modeled ballistic problems using the SPH method. Based on the validation of the simulation results with experiments, some recommendations for the artificial viscosity and the Johnson-Cook failure model in SPH simulations are provided. The linear viscosity coefficient should be increased from a default value of 0.06 to 1.00. Low average particle residual speed (compared to experiments) is observed when the Johnson-Cook failure model is not used in the simulation. Upon inclusion of the failure criteria, the speed was comparable to the experiments. This can be a "calibration" parameter of a model to obtain better agreement with experimental observations.

Avachat et al. [24] investigated orthogonal machining of AISI 1045 with the focus on the effect of the SPH parameters, namely, the smoothing length, particle density and SPH formulation on chip morphology and stress distribution. Different sets of the Johnson-Cook parameters for AISI 1045 steel have been used and their effect on chip morphology and stresses is also investigated.

Madaj et al. [22] performed orthogonal simulations of A2024-T351 alloy using SPH. Variation in chip segmentation is observed on the inclusion of Johnson-Cook failure parameters ($D1$-$D5$ values) and also by varying the value of minimum strain required for failure. They evaluated the effect of friction on cutting forces and concluded that higher friction coefficient led to a higher chip radius, lower shear plane angle and thicker chip, higher plastic strain values and higher average cutting force. They noted the need for the investigation of material models to examine their usability for SPH simulations.

Xi et al. [40] developed machining models to study thermally-assisted machining of Ti6Al4V and studied the influence of the initial workpiece temperature on the chip

formation and cutting force. To reduce the computation time, the coupled SPH-FE model was developed with a workpiece discretized by SPH particles near the tool (high deformation zone) and meshed by the FE mesh away from the tool. Chip segmentation and cyclic cutting force were observed.

2.3.2 3D machining model

The 2D plane strain orthogonal machining model has been the primary focus of the majority of the current studies because of its simplicity. The predicted cutting forces align well with the experimental values. However, the thrust force is highly under-predicted (observed by various researchers [34, 41, 42]). This under-prediction is corrected by increasing the friction coefficient between the tool and the chip to values greater than 1 [43]. Also, the axial force cannot be predicted using this model. Very few studies [44–48] incorporate the 3D machining model. Even in these studies, only a small section of the workpiece has been modeled. Although the cutting forces may stabilize, the chip profile associated with the actual machining operation cannot be predicted. The industrial machining operations are predominantly 3D in nature. Hence, to predict the physical variables such as stresses, strains and temperatures for these operations, a more realistic 3D machining model is needed.

In the following chapters, the machining outputs are predicted by the computational models of machining using the SPH method. The results of the simulation are validated with the experimental observations. Initially, the results of the two-dimensional SPH machining model and coupled SPH-FE model are validated with the results in [22]. Then, using a coupled SPH-FE model, a three-dimensional machining model is prepared. After validating the results of this model, the model is enhanced to include other applications such as the incorporation of machining dynamics and modulated tool path machining.

CHAPTER 3: SMOOTHED PARTICLE HYDRODYNAMICS

Smoothed Particle Hydrodynamics (SPH) is a particle-based, meshless method originally developed in the 1970s by Gingold and Monaghan [37] and Lucy [49] for modeling astrophysical problems. Because of its meshless nature, SPH is being increasingly used for modeling fluid mechanics and solid mechanics problems. The method has several advantages over grid-based methods, including better handling of large deformations and the availability of an intrinsic material separation method for chip separation and crack formation. Due to these advantages, several researchers have applied the SPH method to modeling materials removal processes such as machining.

In this method, a body is discretized using particles. Each particle has an associated set of state variables, e.g., mass, position and velocity, etc. The particle interacts with the neighboring particles which are within its domain of influence. The Smoothing function acts as a weight for the neighboring particles to approximate the state variables of the particle. The discretized conservation equations and constitutive equations are solved to obtain the time variation of the state variables.

3.1 SPH method

The heart of the SPH method is a Smoothing or Kernel function. This function smooths the contribution of the neighboring particle to the property field of a particle, based on the distance from the particle. The influence of the neighboring particle on the particle reduces with the increasing distance from it. Mathematically, the value of a property at a position equals the summation of the multiplication of the property's value at neighboring points by the value of kernel function.

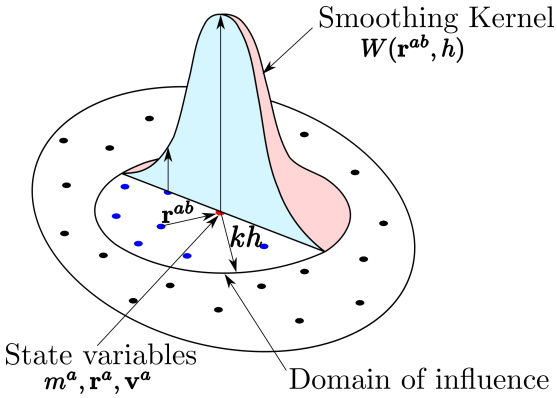

Figure 3.1: SPH method.

3.1.1 Kernel approximation of a function

The motivation of representing any function, $f(\mathbf{r})$ in integral representation and then to kernel approximation comes from Dirac delta function $\delta(\mathbf{r^a} - \mathbf{r^b})$, which is defined as,

$$\delta(\mathbf{r^a} - \mathbf{r^b}) = \begin{cases} \infty, & \mathbf{r^a} = \mathbf{r^b}, \\ 0, & \mathbf{r^a} \neq \mathbf{r^b}. \end{cases} \tag{3.1}$$

The Dirac delta function also has following property,

$$\int_\Omega \delta(\mathbf{r^a} - \mathbf{r^b})\, \mathrm{d}\Omega_{\mathbf{r^b}} = 1. \tag{3.2}$$

Here, $\mathbf{r^a}$ and $\mathbf{r^b}$ are position vectors and $\mathrm{d}\Omega_{\mathbf{r^b}}$ is the volume element associated with the position vector $\mathbf{r^b}$. The integral representation of the function, $f(\mathbf{r})$ is given by,

$$f(\mathbf{r}^a) = \int_\Omega f(\mathbf{r^b})\delta(\mathbf{r^a} - \mathbf{r^b})\, \mathrm{d}\Omega_{\mathbf{r^b}}. \tag{3.3}$$

The Kernel approximation of the function is obtained by replacing the Dirac delta function by a smoothing function or kernel function $W(|\mathbf{r^a} - \mathbf{r^b}|, h)$,

$$\langle f(\mathbf{r}^a) \rangle = \int_\Omega f(\mathbf{r^b}) W(|\mathbf{r^a} - \mathbf{r^b}|, h)\, \mathrm{d}\Omega_{\mathbf{r^b}}. \tag{3.4}$$

Here, $|\mathbf{r^a} - \mathbf{r^b}|$ is the distance between $\mathbf{r^a}$ and $\mathbf{r^b}$ and h is called the smoothing length.

Since the domain is discretized by particles, the integral form of the function can be converted into the summation form or particle approximation given by,

$$\langle f(\mathbf{r}^a)\rangle = \int_\Omega W(\mathbf{r}^{ab}, h) f(\mathbf{r}^b)\, \mathrm{d}\Omega_{\mathbf{r}^b} \approx \sum_{j=1}^{N} W(\mathbf{r}^{ab}, h) f(\mathbf{r}^b) \frac{m^b}{\rho^b}. \tag{3.5}$$

Here, $\mathbf{r}^{ab} = |\mathbf{r}^a - \mathbf{r}^b|$, m^b is the mass and ρ^b is the density of the particle at position $\mathbf{r}^b$.

3.1.2 Smoothing Kernel

The smoothing function, W is of utmost importance in SPH. It determines the shape for the function approximation and defines the zone of influence of a particle. It must satisfy the following condition:

a) Normalization condition:

$$\int_\Omega W(|\mathbf{r^a} - \mathbf{r^b}|, h)\, \mathrm{d}\Omega_{\mathbf{r^b}} = 1 \tag{3.6}$$

b) Dirac delta property:

$$\lim_{h\to 0} W(|\mathbf{r^a} - \mathbf{r^b}|, h) = \delta(\mathbf{r^a} - \mathbf{r^b}) \tag{3.7}$$

c) Compactness:

$$W(|\mathbf{r^a} - \mathbf{r^b}|, h) = 0, \text{when } |\mathbf{r^a} - \mathbf{r^b}| > \kappa h \tag{3.8}$$

where, κh is termed as the compact support.

d) The function should be smooth, monotonically decreasing, positive and axis-symmetric function (even function) and at least second-order derivable.

There are many forms of the kernel function, but the most common are the Gaussian

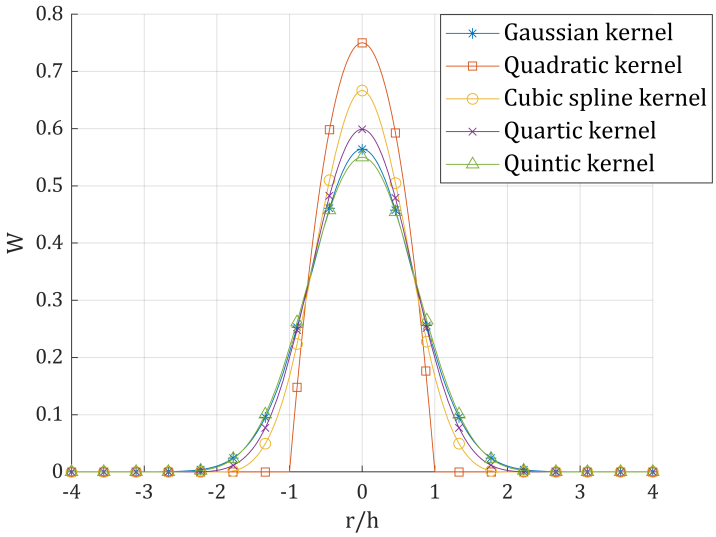

Figure 3.2: Comparison of SPH kernels.

function (because of its physical significance) and the Cubic spline (as it is non-zero only inside the region of compact support). The Gaussian function has the following form:

$$W(\mathbf{r};h) = \Big(\frac{1}{h\sqrt{\pi}}\Big)^{d} e^{-(q^2/h^2)}. \tag{3.9}$$

Here, d is the space dimension (1,2 or 3) of the problem, $\mathbf{r}$ is the distance from a neighbouring particle and $q = \frac{|\mathbf{r}|}{h}$.

The cubic spline has the form:

$$W(\mathbf{r};h) = C \begin{cases} (2-q)^3 - 4(1-q)^3 & 0 \le q < 1, \\ (2-q)^3 & 1 \le q < 2, \\ 0 & q \ge 2. \end{cases} \tag{3.10}$$

where, C equals $\frac{1}{6h}$, $\frac{5}{14\pi h^2}$ and $\frac{1}{4\pi h^3}$ respectively for one, two and three dimension respectively. Because of its' finite compact support, the order of computation reduces from $\mathcal{O}(N^2)$ to $\mathcal{O}(N \times N_{neighbour})$, where $N_{neighbour}$ is the number of neighbourhood particle within the compact support. A comparison of different smoothing kernels is shown in Fig. 3.2.

3.1.3 Kernel approximation of Gradient

The kernel approximation of the gradient of a scalar field $f(\mathbf{r})$ is calculated using the derivative of the smoothing kernel and it's functional value. It is given by,

$$\langle \nabla_{\mathbf{r}^a} f(\mathbf{r}^a) \rangle = \sum_{j=1}^{N} \frac{m^b}{\rho^b} f(\mathbf{r}^b) \nabla_{\mathbf{r}^a} W(\mathbf{r}^{ab}, h). \tag{3.11}$$

There are other formulations of SPH depending upon the definition of the derivative. Two of the most common formulations, asymmetric and symmetric formulation, respectively, are given below.

$$\langle \nabla \cdot \mathbf{f}(\mathbf{r}^a) \rangle = \frac{1}{\rho^a} \left[\sum_{b=1}^{N} m^b [\mathbf{f}(\mathbf{r}^b) - \mathbf{f}(\mathbf{r}^a)] \cdot \nabla W(\mathbf{r}^{ab}, h) \right], \tag{3.12}$$

$$\langle \nabla \cdot \mathbf{f}(\mathbf{r}^a) \rangle = \rho^a \left[\sum_{b=1}^{N} m^b \left[\frac{\mathbf{f}(\mathbf{r}^b)}{(\rho^b)^2} + \frac{\mathbf{f}(\mathbf{r}^a)}{(\rho^a)^2} \right] \cdot \nabla W(\mathbf{r}^{ab}, h) \right]. \tag{3.13}$$

3.1.4 Kernel approximation of Divergence

The kernel approximation of divergence of a vector field $\mathbf{F}(\mathbf{r})$ is obtained by replacing $\mathbf{F}(\mathbf{r}^a)$ by $\nabla \cdot \mathbf{F}(\mathbf{r}^a)$ in Eq. (3.4). The detailed derivation is given in the Appendix. Thus, the gradient of the function is calculated from the value of the function and the gradient of the kernel function and not by the gradient of the actual function.

$$\langle \nabla \cdot \mathbf{F}(\mathbf{r}^a) \rangle = \sum_{b=1}^{N} \frac{m^b}{\rho^b} \mathbf{F}(\mathbf{r}^b) \cdot \nabla W(\mathbf{r}^{ab}, h) \tag{3.14}$$

3.1.5 Accuracy of Kernel approximation

The kernel approximation of a function is of second-order accuracy. This can be shown by Taylor series expansion of $f(\mathbf{r}^b)$ around $\mathbf{r}^a$.

$$
\begin{aligned}
\langle f(\mathbf{r}^a)\rangle &= \int_\Omega f(\mathbf{r}^b) W \,\mathrm{d}\Omega_{\mathbf{r}^b} \\
&= \int_\Omega \Big[f(\mathbf{r}^a) + (\mathbf{r}_i^b - \mathbf{r}_i^a)\frac{\partial f}{\partial \mathbf{r}_i^a} + \frac{1}{2}(\mathbf{r}_j^b - \mathbf{r}_j^a)(\mathbf{r}_k^b - \mathbf{r}_k^a)\frac{\partial^2 f}{\partial \mathbf{r}_j^a \mathbf{r}_k^a} + \mathcal{O}[(\mathbf{r}^b - \mathbf{r}^a)^3] \Big] W \,\mathrm{d}\Omega_{\mathbf{r}^b} \\
&= f(\mathbf{r}^a) + \frac{\partial f}{\partial \mathbf{r}_i^a}\int_\Omega (\mathbf{r}_i^b - \mathbf{r}_i^a) W \,\mathrm{d}\Omega_{\mathbf{r}^b} + \frac{1}{2}\frac{\partial^2 f}{\partial \mathbf{r}_j^a \mathbf{r}_k^a}\int_\Omega (\mathbf{r}_j^b - \mathbf{r}_j^a)(\mathbf{r}_k^b - \mathbf{r}_k^a) W \,\mathrm{d}\Omega_{\mathbf{r}^b} \\
&\quad + \mathcal{O}[(\mathbf{r}^b - \mathbf{r}^a)^3]
\end{aligned}
\tag{3.15}
$$

Here, i, j, k are indices denoting co-ordinate directions, with a repeated index implying summation. The second term equals zero, as the term inside the integral is odd ($\mathbf{r}^b - \mathbf{r}^a$ is odd and W is an even function). Hence, the order of approximation is given by third term onward. The term $(\mathbf{r}^b - \mathbf{r}^a)$ is of $\mathcal{O}(h)$, resulting in an approximation to $\mathcal{O}(h^2)$.

Similarly, the kernel approximation of a gradient of a function is of second-order accuracy, $\mathcal{O}(h^2)$.

$$
\begin{aligned}
\langle \nabla f(\mathbf{r}^a)\rangle &= \int_\Omega f(\mathbf{r}^b) \nabla W \,\mathrm{d}\Omega_{\mathbf{r}^b} \\
&= \int_\Omega \Big[f(\mathbf{r}^a) + (\mathbf{r}_i^b - \mathbf{r}_i^a)\frac{\partial f}{\partial \mathbf{r}_i^a} + \frac{1}{2}(\mathbf{r}_j^b - \mathbf{r}_j^a)(\mathbf{r}_k^b - \mathbf{r}_k^a)\frac{\partial^2 f}{\partial \mathbf{r}_j^a \mathbf{r}_k^a} + \mathcal{O}[(\mathbf{r}^b - \mathbf{r}^a)^3] \Big] \nabla W \,\mathrm{d}\Omega_{\mathbf{r}^b} \\
&= f(\mathbf{r}^a)\int_\Omega \nabla W \,\mathrm{d}\Omega_{\mathbf{r}^b} + \frac{\partial f}{\partial \mathbf{r}_i^a}\int_\Omega (\mathbf{r}_i^b - \mathbf{r}_i^a)\nabla W \,\mathrm{d}\Omega_{\mathbf{r}^b} \\
&\qquad + \frac{1}{2}\frac{\partial^2 f}{\partial \mathbf{r}_j^a \mathbf{r}_k^a}\int_\Omega (\mathbf{r}_j^b - \mathbf{r}_j^a)(\mathbf{r}_k^b - \mathbf{r}_k^a)\nabla W \,\mathrm{d}\Omega_{\mathbf{r}^b} + \mathcal{O}[(\mathbf{r}^b - \mathbf{r}^a)^3] \\
&= \nabla f(\mathbf{r}^a) + \frac{1}{2}\frac{\partial^2 f}{\partial \mathbf{r}_j^a \mathbf{r}_k^a}\int_\Omega (\mathbf{r}_j^b - \mathbf{r}_j^a)(\mathbf{r}_k^b - \mathbf{r}_k^a)\nabla W \,\mathrm{d}\Omega_{\mathbf{r}^b} + \mathcal{O}[(\mathbf{r}^b - \mathbf{r}^a)^3]
\end{aligned}
\tag{3.16}
$$

The $\int_\Omega \nabla W \mathrm{d}\Omega_{\mathbf{r}^b}$ equals zero, as ∇W is odd function. The second term equals the identity matrix, which can be shown by integrating by parts, using the divergence theorem and the compactness and normalization of the kernel function. Hence, using

a similar argument as in the approximation of the function above, the approximation is of $\mathcal{O}(h^2)$.

However, the second-order accuracy of the kernel function and its derivative is true only for the interior points. At the boundary region, there is a truncation of the smoothing function [50]. Several modifications in the original SPH method, such as corrective smoothed particle method (CSPM) [51], discontinuous smoothed particle method (DSPH) [52], etc., are proposed for removing this boundary inconsistency.

Thus, the error consists of an integral term error and a discretization error. The Integral term error can be reduced by decreasing the smoothing length, while the discretization error can be reduced by increasing the number of points in the domain. However, this needs to be balanced by the computation time. Disorder in dynamic systems has little influence on the accuracy of the SPH method. This can be attributed to the SPH formulations, which conserve momentum and energy. Also, the use of a symplectic integrator like the Leapfrog integrator gives accurate results, as it conserves angular momentum and is reversible [53].

3.1.6 Artificial viscosity

A viscosity term Π^{ab} is added to the conservation of linear momentum equation to stabilize the numerical algorithm of SPH for shock wave and contact discontinuities. The most commonly used formulation, introduced by Monaghan and Gingold [54] and is given by,

$$\Pi^{ab} = \begin{cases} [-\alpha \bar{c}^{ab} \mu^{ab} + \beta (\mu^{ab})^2] / \bar{\rho}^{ab}, & \text{for } \mathbf{v}^{ab} \cdot \mathbf{r}^{ab} < 0, \\ 0, & \text{otherwise.} \end{cases} \tag{3.17}$$

Here,

$$\mu^{ab} = \frac{\bar{h}^{ab}\ \mathbf{v}^{ab}.\mathbf{r}^{ab}}{\mid \mathbf{r}^{ab} \mid^2 + \epsilon(\bar{h}^{ab})^2}, \tag{3.18}$$

with $\bar{h}^{ab}, \bar{\rho}^{ab}$and $\bar{c}^{ab}$ are average of the smoothing length, density and the sound speed of the particles at position $\mathbf{r}^a$ and $\mathbf{r}^b$ respectively. The Eq. (3.17) has two parameters α and β to regulate the viscosity. Typically, the values of α is in range of [0,1] and $\beta = 2\alpha$ is given. A small number, $\epsilon \approx 0.01$ prevents a singularity when the particles are very close to each other, i.e. $\mathbf{r}^{ab} \approx 0$. This form conserves linear momentum, as it is symmetric. The summation over all particles of this term with the anti-symmetric kernel derivative is zero. A more detailed account of the artificial viscosity can be found in [53]. Artificial viscosity produces a repulsive force when the two particles approach each other. This prevents the particles from occupying the same position.

3.1.7 Variable Smoothing length

Smoothing length determines the radius of influence of the particles. This governs the interpolation of physical properties in the domain. In general, the number of particles in the neighbor for each particle in the domain is kept the same within a range. For example, a region with a dense distribution particles has a small smoothing length. However, for high deformation applications, for example, machining, there is a large movement of particles. This requires a dynamic variation of smoothing length. In LS-DYNA, two approaches for the calculation of the smoothing length are implemented based on the divergence of the velocity field and are given by,

$$\frac{d}{dt}[h(t)] = \frac{1}{d}h(t)\nabla \cdot \mathbf{v} \tag{3.19}$$

$$\frac{d}{dt}[h(t)] = \frac{1}{d}h(t)\left(\nabla \cdot \mathbf{v}\right)^{\frac{1}{3}}. \tag{3.20}$$

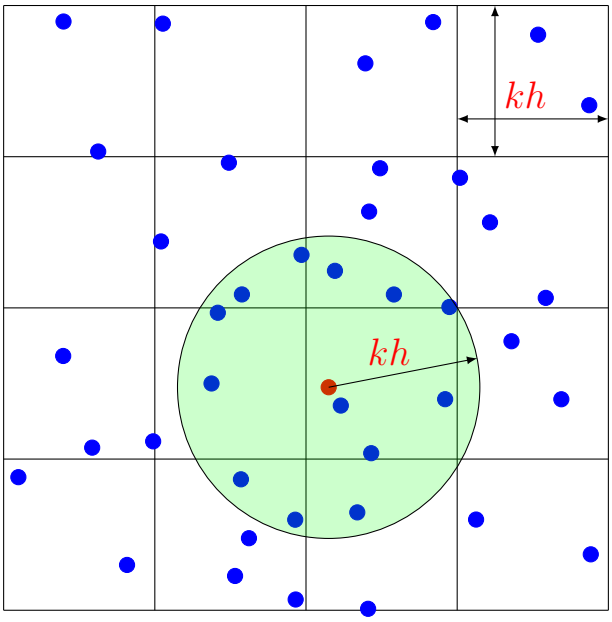

Figure 3.3: Neighbour search by Bucket sort method.

Here, $h(t)$ is the smoothing length at time t, d is the dimension of the domain and $\mathbf{v}$ is the velocity vector.

3.1.8 Bucket sorting

Locating the neighboring particles of each particle is done in SPH for every time step. This is required to find the particles in the influence domain of each particle, i.e., at a distance kh from the particle. This step is a computationally expensive step. Bucket sort [55] is an efficient algorithm for this.

The entire domain is partitioned into a grid or bucket of size kh, as depicted in Fig. 3.3. Based on the initial position of the particles, they are assigned to the corresponding bucket and hence the initial neighbors are found for each particle. As the simulation progresses, the particles may move to the other adjacent bucket. The neighbors for each particle are searched in the same bucket and the adjacent buckets. This saves the computation of the distance between the particles globally for all the particles.

3.2 Conservation laws

Conservation laws namely, the conservation of mass, linear momentum and energy are derived in SPH formulation. Angular momentum is naturally conserved by the SPH formulation.

3.2.1 Conservation of Mass

The continuity (conservation of mass) equation is given by,

$$\frac{D\rho}{Dt} = -\rho \left(\nabla \cdot \mathbf{v}\right) \tag{3.21}$$

This can be written in SPH form as shown below equation. This is derived using the asymmetric formulation of the derivative.

$$< \frac{D\rho^a}{Dt} > = \sum_{b=1}^{N} m^b \left(v_i^a - v_i^b\right) \frac{\partial W^{ab}}{\partial x_i^a} \, . \tag{3.22}$$

Here, ρ is the density, m is mass, $\mathbf{v}$ is velocity and x_i are the co-ordinates. The evolution of density is governed by this equation.

3.2.2 Conservation of Linear Momentum

The conservation of linear momentum is given by

$$\frac{D\mathbf{v}}{Dt} = \frac{1}{\rho} \left(\nabla \cdot \boldsymbol{\sigma}\right). \tag{3.23}$$

In SPH formulation, the equation is given by

$$< \frac{Dv_i^a}{Dt} > = \sum_{b=1}^{N} m^b \left(\frac{\sigma_{ij}^a}{\left(\rho^a\right)^2} + \frac{\sigma_{ij}^b}{\left(\rho^b\right)^2} - \Pi^{ab} \right) \frac{\partial W^{ab}}{\partial x_j^a} \, . \tag{3.24}$$

Here, $\boldsymbol{\sigma}$ is the total stress tensor and Π^{ab} is the artificial viscosity term accounting for numerical instability during a discontinuity, for example, a shock. The equation

of conservation of linear momentum evolves the forces on the particles during the simulation. The above equation is derived using the symmetric formulation of the derivative. It is asymmetric pairwise in a and b, as the gradient of the kernel function is odd, implying that the force exerted by particle a on b is equal and opposite to the force on particle b by particle a.

3.2.3 Conservation of Angular Momentum

Angular momentum is given by $\mathbf{L} = \mathbf{r} \times m\mathbf{v}$. Taking time derivative,

$$\frac{D\mathbf{L}}{Dt} = m\mathbf{v} \times \mathbf{v} + m\mathbf{r} \times \frac{D\mathbf{v}}{Dt} = m\mathbf{r} \times \frac{D\mathbf{v}}{Dt}. \tag{3.25}$$

Converting this equation to SPH form and summing for all the i^{th} particles gives,

$$\frac{D\mathbf{L}}{Dt} = \sum_{i=1}^{N} \frac{D\mathbf{L}_i}{Dt} = \sum_{a=1}^{N}\sum_{b=1}^{N} m^a m^b \mathbf{r}^b \times \left(\frac{\sigma_{ij}^a}{(\rho^a)^2} + \frac{\sigma_{ij}^b}{(\rho^b)^2} - \Pi_{ij} \right) \frac{\partial W^{ab}}{\partial x_j^a}. \tag{3.26}$$

The summation for all particles can be shown to be equal to zero by interchanging i and j in Eq. (3.26) and using Eq. (3.24), thereby conserving the angular momentum.

3.2.4 Conservation of Energy

The rate of change of internal energy equals the sum of stress work (work done by the internal stresses) and rate of thermal energy entering into a body, given by

$$\frac{DU}{Dt} = \frac{\boldsymbol{\sigma}}{\rho} : (\text{grad}\ \mathbf{v}) + Q \tag{3.27}$$

where U is internal energy per unit mass, : denotes the double inner product between two tensors and Q is rate of thermal energy per unit mass.

The SPH form of energy conservation equation is given by,

$$< \frac{DU^a}{Dt} > = \frac{1}{2} \sum_{b=1}^{N} m^b \left(\frac{p^a}{(\rho^a)^2} + \frac{p^b}{(\rho^b)^2} \right) v_j^{ab} \frac{\partial W^{ab}}{\partial r_j^a} + \frac{\mu^a}{2\rho^a} \varepsilon_{ij}^a \varepsilon_{ij}^a + < Q_i > . \tag{3.28}$$

Here, p is the isotropic pressure component of the total stress tensor $\boldsymbol{\sigma}$, μ is dynamic viscosity, and ε is the shear strain rate.

The rate of thermal energy per unit mass is given by,

$$Q = -\int_{\Omega} \nabla \cdot \mathbf{q} \, \mathrm{d}\Omega. \tag{3.29}$$

The conductive heat flux $\mathbf{q}$ is given by the Fourier's law,

$$\mathbf{q} = -k\nabla T. \tag{3.30}$$

Here, k is thermal conductivity and T is temperature of the body.

The SPH form of rate of thermal energy is given by (derivation in Appendix),

$$< Q^a > = \sum_{b=1}^{N} \frac{m^b}{\rho^a \rho^b} \frac{(k^a + k^b)(T^a - T^b)}{\mid \mathbf{r}^{ab} \mid^2} \mathbf{r}^{ab} \nabla W^{ab} \tag{3.31}$$

This form conserves the total thermal energy. Also, heat flows from higher to lower temperature. However, Cleary & Monaghan [56] proposed the below form. This form ensures the continuity of heat flux across the interface of different materials.

$$< Q^a > = \sum_{b=1}^{N} \frac{4m^b}{\rho^a \rho^b} \frac{k^a k^b}{(k^a + k^b)} (T^a - T^b) \frac{\mathbf{r}^{ab}}{\mid \mathbf{r}^{ab} \mid^2} \nabla W^{ab} \tag{3.32}$$

3.3 Solid mechanics

3.3.1 Equation of state

The equation of state (EOS) determines the pressure p as a function of local density ρ and other material property variables. For machining simulations, the Mie-Grüneisen equation has been widely used and is given by the following equations.

For compression ($\mu > 0$),

$$p = \frac{\rho_0 C^2 \mu \left[1 + \left(1 - \frac{\gamma_0}{2}\right)\mu - \frac{b}{2}\mu^2\right]}{\left[1 - (S_1 - 1)\,\mu - S_2 \frac{\mu^2}{\mu+1} - S_3 \frac{\mu^3}{(\mu+1)^2}\right]^2} + (\gamma_0 + b\mu)\, e \;, \tag{3.33}$$

and for tension ($\mu < 0$),

$$p = \rho_0 C^2 \mu + (\gamma_0 + b\mu) e \;. \tag{3.34}$$

Here, C is the bulk speed of sound, $\mu = \rho/\rho_0 - 1$, ρ is the current density, ρ_0 is the reference density, γ_0 is Grüneisen gamma, S_1, S_2 and S_3 are the Hugoniot slope coefficients, b is the first order volume correction to γ_0, and e is the internal energy per initial volume. The parameters $C, \gamma_0, S_1, S_2, S_3$ and b define the EOS of the material.

3.3.2 Material model

The total stress tensor $\boldsymbol{\sigma}$ consists of the hydrostatic pressure p and the deviatoric stress $\mathbf{S}$ and is given by,

$$\sigma_{ij} = -p\delta_{ij} + S_{ij} \;. \tag{3.35}$$

The deviatoric stress is evolved using the Jaumann rate and is expressed as,

$$\dot{S}_{ij} = 2G\left(d_{ij} - \frac{\delta_{ij} d_{kk}}{3}\right) + S_{ik} w_{jk} + S_{jk} w_{ik} \;. \tag{3.36}$$

Here, G is shear modulus, $\boldsymbol{d}$ is the strain rate tensor and $\boldsymbol{w}$ is the rotation tensor given by,

$$d_{ij} = \frac{1}{2}\left(\frac{\partial v_i}{\partial x_j} + \frac{\partial v_j}{\partial x_i}\right), \quad w_{ij} = \frac{1}{2}\left(\frac{\partial v_i}{\partial x_j} - \frac{\partial v_j}{\partial x_i}\right) . \tag{3.37}$$

The inelastic behaviour of the workpiece is modelled using the Johnson-Cook material model given by,

$$\sigma_{eq} = \underbrace{\left(A + B\varepsilon_p^n\right)}_{\text{Strain hardening}} \underbrace{\left[1 + C\ \ln\left(\frac{\dot{\varepsilon}_p}{\dot{\varepsilon}_0}\right)\right]}_{\text{Strain rate sensitivity}} \underbrace{\left[1 - \left(\frac{T - T_0}{T_m - T_0}\right)^m\right]}_{\text{Thermal softening}} . \tag{3.38}$$

Here, σ_{eq} is the flow stress, A, B, C, n, m are material constants. Furthermore, ε_p is the equivalent plastic strain, $\dot{\varepsilon}_p$ is the plastic strain-rate, $\dot{\varepsilon}_0$ is a reference strain-rate, T_m is the melting temperature, and T_0 is a reference temperature. In addition to the constitutive material model, the Johnson-Cook damage model is used by Madaj et.al. [22] to simulate failure and is given by,

$$\varepsilon_f = \underbrace{[D_1 + D_2 \exp{(D_3 \sigma^*)}]}_{\text{Pressure dependence}} \underbrace{\left[1 + D_4 \ln\left(\frac{\dot{\varepsilon_p}}{\dot{\varepsilon}_0}\right)\right]}_{\text{Strain rate}} \underbrace{\left[1 + D_5 \left(\frac{T - T_0}{T_m - T_0}\right)\right]}_{\text{Temperature}} . \tag{3.39}$$

Here, ε_f is the equivalent fracture strain. $D_1 - D_5$ are the damage model constants. The stress triaxiality parameter, σ^* is a ratio of the mean stress (σ_m) and the equivalent stress (σ_{eq}). The Fracture occurs when the cumulative value of the equivalent plastic strain equals ε_f. The damage of an element, D is defined based on a cumulative damage law, represented by,

$$D = \sum \frac{\Delta \varepsilon_p}{\varepsilon_f} . \tag{3.40}$$

When D equals unity, fracture is assumed to occur. The stress tensor in the material undergoing deformation is given by the scalar damage equation,

$$\sigma_D = (1 - D)\sigma_{eq} . \tag{3.41}$$

It is noteworthy that the particles reaching equivalent fracture strain are deleted from the SPH calculations. But, the mass and energy of these particles are retained. This ensures the conservation of mass and momentum. This is contrary to the FEM, where the elements are completely deleted due to high distortion.

3.4 Calculation cycle

A typical SPH calculation cycle [55] is shown in Fig 3.4. The conservation equations along with constitutive equations are solved by an explicit time integration using the LeapFrog algorithm. A bucket sort algorithm is used for the neighborhood search.

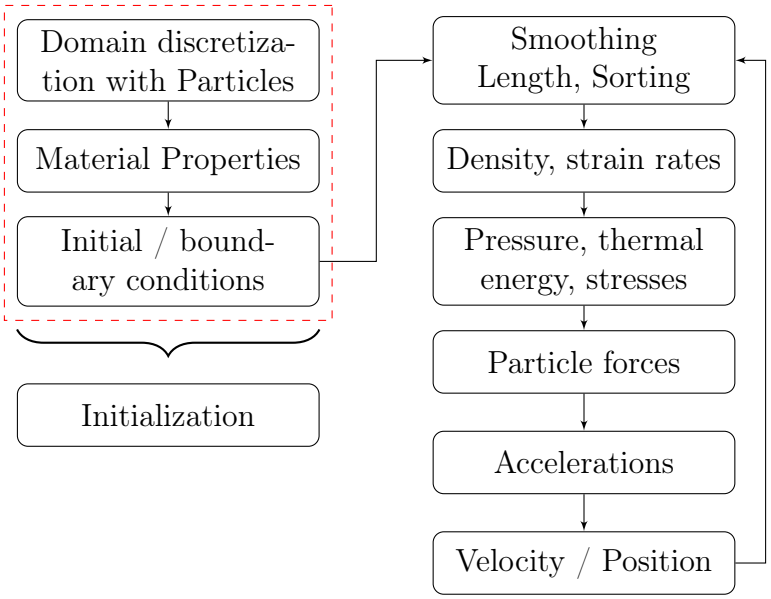

Figure 3.4: The calculation cycle of SPH.

3.5 Time step

The numerical integration of the discretized SPH equation is done by explicit time integration. To have a stable solution, it must satisfy the CFL (Courant-Friedrichs-Levy) condition [57], given by the Eq. (3.42). Physically, it denotes that the time step should be less than the time required for the elastic waves to pass within the spatial separation of the particles (l). The speed of the longitudinal elastic wave is given by c_0 and τ is a time step scaling factor.

$$\Delta t \leq \tau \frac{l}{c_o}. \tag{3.42}$$

For a solid medium, c_0 is given by,

$$c_0 = \sqrt{\frac{K + \frac{4}{3}G}{\rho}}. \tag{3.43}$$

3.6 Time integration

To advance the simulation by a global time step Δt, the acceleration of each particle is calculated from the force acting on the particle. The velocity and position of the particles are calculated using the numerical integration of the acceleration. The Verlet scheme [58] and the Leapfrog integration scheme are the commonly used methods for particle simulations.

3.6.1 Verlet integration scheme

Verlet integration scheme [58] is commonly used for numerically integrating Newton's equations of motion for molecular dynamics simulations. For SPH simulations, this method is used in LAMMPS [59] and SPHysics codes [60]. The position and the velocity are calculated using the Eq. (3.44). This scheme is of second-order accuracy and provides good numerical stability.

$$\begin{aligned} v_{t+\Delta t} &= v_{t-\Delta t} + 2\Delta t\, F_t \\ x_{t+\Delta t} &= x_t + \Delta t\, v_t + \frac{1}{2}\Delta t^2 F_t. \end{aligned} \tag{3.44}$$

3.6.2 Leapfrog integration scheme

Leapfrog integration is a second-order integration method. In this scheme, the velocities are calculated at the mid-points of the time steps. However, the position is calculated for each time step using the equation given by,

$$\begin{aligned} x_{t+\Delta t} &= x_t + \Delta t\, v_{t+\frac{\Delta t}{2}} \\ v_{t+\frac{3\Delta t}{2}} &= v_{t+\frac{\Delta t}{2}} + \Delta t\, a_{t+\Delta t}. \end{aligned} \tag{3.45}$$

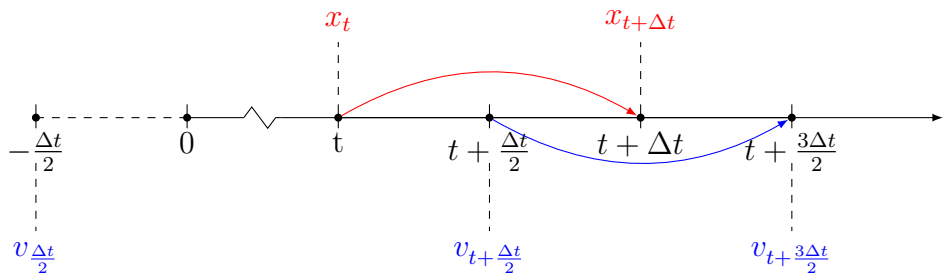

Figure 3.5: Leapfrog integration scheme.

The scheme is depicted in Fig. 3.5.

The initial velocity is calculated using the Euler formula given by,

$$v_{(-\frac{\Delta t}{2})} = v_0 - \frac{\Delta t}{2} a_0. \tag{3.46}$$

The Leapfrog scheme is time-reversible [61]. Also, this scheme satisfies the conservation equations. This limits the propagation of error. This scheme is used in LS-DYNA for time integration [62].

CHAPTER 4: PROBLEM DESCRIPTION AND 2D SPH MODELS

Machining is one of the most common manufacturing processes. Depending upon the part geometry, it can be widely classified into three operations: turning, milling, and drilling. The Turning operation is the focus of this study. In turning, there is a cutting tool and raw material (also called a workpiece). The workpiece is clamped on a lathe chuck and is given a rotational velocity about its axis. The tool is secured on a tool-post and is set with a depth of cut relative to the workpiece. The tool is given a feed motion towards the workpiece. As the tool and workpiece interact, cutting takes place and chips are formed.

Thus, there are two approaches for modeling the turning operation: two-dimensional and three-dimensional approach. Because of the higher complexity associated with the three-dimensional modeling, the two-dimensional modeling is done initially using a complete SPH model. The machining conditions used in this model are taken from Madaj et al. [22], where orthogonal machining has been studied using the SPH method. Another model with a coupled SPH-FE mesh is also developed. The results of the two-dimensional models are presented in this chapter. In subsequent chapters, a parametric study of the SPH parameters is conducted to understand their effects on the simulation results. Thereafter, three-dimensional models are studied.

4.1 Motivation for the coupled SPH-FE model

The SPH method being a meshless method, has several advantages over the grid-based approaches in modeling high strain applications such as machining. Particles undergo deformation move without any topological restrictions. Furthermore, a separation model or contact model is not required in the SPH method. The relative

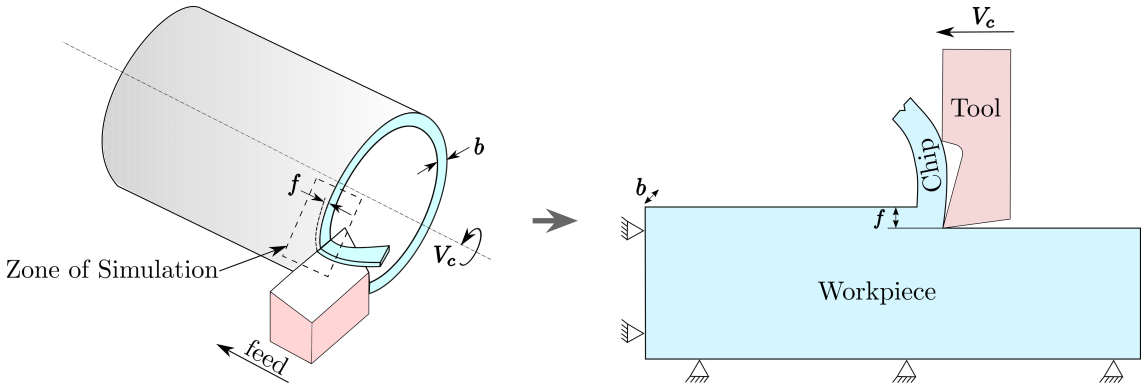

(a) 3D: actual machining. (b) 2D: simulated model.

Figure 4.1: 2D simplification of Turning operation.

motion of the particles with respect to each other and with respect to the tool surface allows for a "natural" chip-workpiece separation.

The SPH method is computationally expensive. The computational time depends on the number of particles in the support domain of each particle. The higher the number of particles in this domain, the longer the simulation takes to run [63]. This run-time can be a severe impediment to considering realistic models of a machining process and obtaining accurate results. To address this concern, a coupled SPH-FE model is studied. The SPH model is used for the region where severe deformations and material removal take place. The FE model is used for the rest of the workpiece. The SPH and FE mesh are coupled at the interface. There is a reduction in the number of SPH particles in the coupled SPH-FE mesh. The benefit of this is verified by comparing the results from this model and the simulation time with a validated ful-SPH model.

4.2 Geometry

The geometry for both the SPH model and the coupled SPH-FE model are chosen according to Madaj et al. [22]. The workpiece dimensions are 5.8 mm $\times$ 1.0 mm $\times$ 0.05 mm. The tool rake angle is 17.5°; the clearance angle is 7°; and the tip radius is 20 μm. The depth of cut (b) is 4 mm and the uncut chip thickness (f) is 0.4 mm.

4.3 The SPH model

The SPH model consists of the workpiece discretized completely by particles and the tool by FE elements. The SPH particles are equispaced in all directions with an inter-particle spacing of 0.025 mm. This leads to a total of 18,560 SPH particles representing the workpiece. The SPH model is shown in Fig. 4.2. Two layers of particles are used in the Z direction (same as in Madaj et al. [22]). As the particles are constrained from moving in the Z direction, the number of layers in Z direction is not relevant to the results of this investigation.

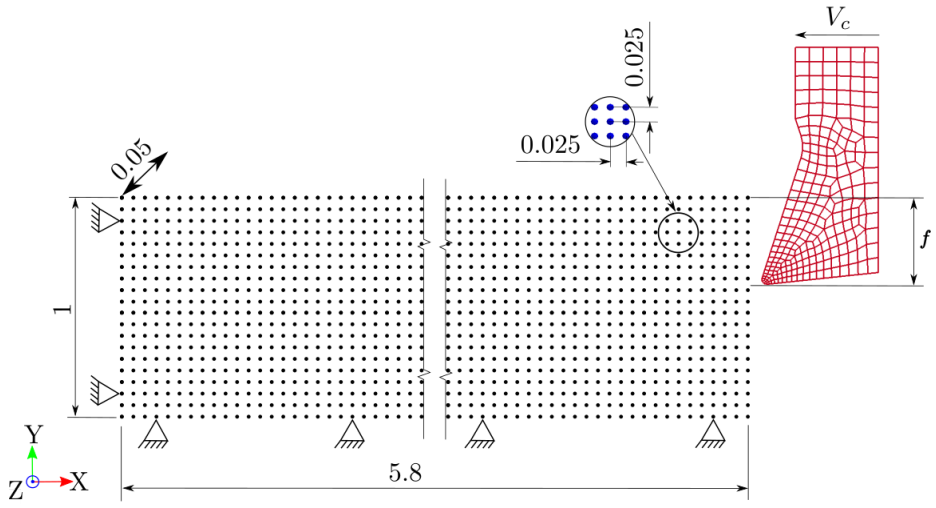

Figure 4.2: The SPH model.

4.4 The SPH-FE coupled model

In the SPH-FE coupled model, the workpiece is divided into two zones. The zone where the tool interacts with the workpiece is modeled with SPH particles. In this zone, the cutting takes place and there is high deformation. The lower zone is modeled with FEM elements. With this modification, the number of SPH particles decreases by around 50%. The SPH-FE coupled model is shown in Fig. 4.3. The coupling of SPH particles with FE mesh is achieved by constraining the bottom layer of SPH particles to the FE mesh by using the node to surface constraining algorithm. The

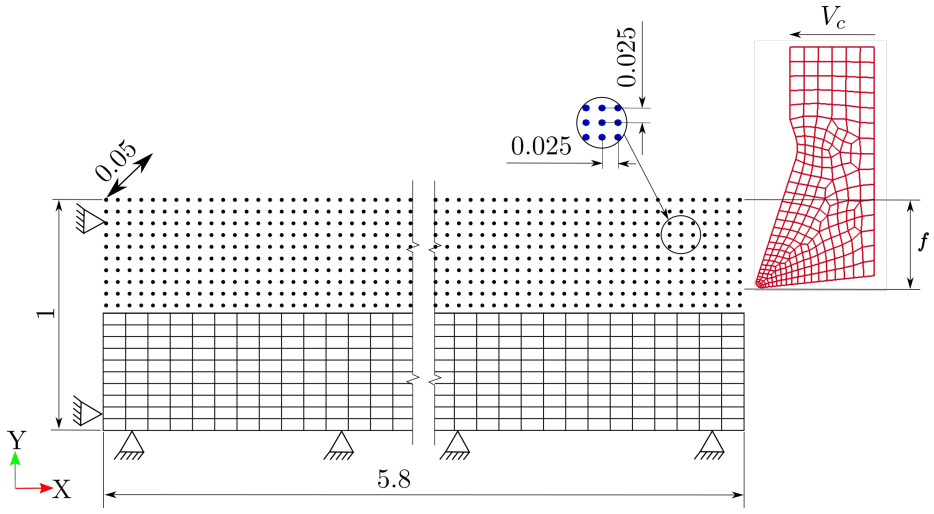

Figure 4.3: The coupled SPH-FE model.

SPH elements are considered as slave surface and the finite elements as master surface. The acceleration of each slave node is interpolated from the master segment containing its contact points [55]. Also, for proper coupling, three rows of SPH elements are kept between the FE mesh and the uncut part of SPH elements.

4.5 Boundary conditions

For both the models, the tool is given the cutting velocity of 800 m/min in the negative X direction and completely constrained in all the other directions. The workpiece is fully constrained on the left and bottom sides. Note that the boundary condition is applied on the FEM elements and the SPH particles for the SPH-FE coupled model. For the plane strain assumption, the motion of all the SPH particles and FEM elements of the workpiece and tool is fully constrained in the Z direction (normal to the plane).

4.6 Material model and properties

The workpiece material is the aluminium alloy A2024-351, and the tool is made of an uncoated cemented carbide. The physical properties of the workpiece and tool are given in Table 4.1. The workpiece is modeled using the Johnson-Cook material model

Table 4.1: Physical properties of Workpiece and Tool [1].

Property	Workpiece	Tool
Density, ρ (Kg/m^3)	2700	11900
Young's Modulus, E (GPa)	73	534
Poisson's ratio, μ	0.33	0.22
Specific heat, C_p (J/Kg K^{-1})	875	-
T_{melt}, (K)	793	-
T_{room}, (K)	300	300

Table 4.2: Johnson-Cook parameters of workpiece (A2024-351) [1].

Parameter	A (MPa)	B(MPa)	n	C	m
Value	352	440	0.42	0.09	1.03
Parameter	D1	D2	D3	D4	D5
Value	0.13	0.13	-1.50	0.011	0

with the Johnson-Cook damage model. The value of model parameters are given in Table 4.2. The tool is modeled as a rigid body.

4.7 Result

The results of the coupled SPH-FE model are compared with the SPH model. The outputs are chip profiles, plastic strain, damage variable and cutting forces.

4.7.1 Chip formation

The chip formation for the SPH model and coupled SPH-FE model is shown in Fig. 4.4 for four different times. The top row of figures corresponds to the SPH model and the bottom row corresponds to the SPH-FE model. The chip shape of the SPH model is consistent is with that obtained in [22]. Furthermore, the chip shape predicted by the SPH-FE model is the same as that predicted by the SPH model at all four times. The figure also illustrates the ability of the SPH method to simulate large deformations occurring during the machining operations. The chip separation, chip curl, highly distorted meshes and self-contact are major challenges in Lagrangian FE formulations but are easily handled by the SPH method.

Figures 4.5a and 4.6a show the distribution of von Mises stress and plastic strain

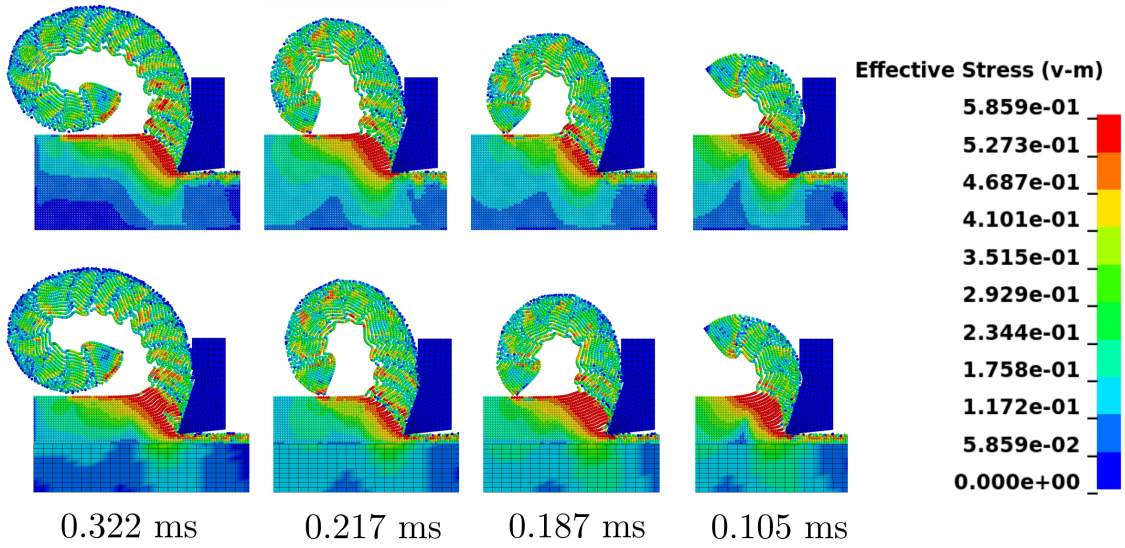

Figure 4.4: Chip shape at four different times as predicted by the SPH model (top row) and SPH-FE model (bottom row).

respectively for the SPH model. The results shown in these figures are consistent with [22]. The von Mises stress and plastic strain distribution for the coupled SPH-FE model are shown in Figs. 4.5b and 4.6b respectively. Clearly, these results are almost identical to those from the SPH model. Furthermore, it can be observed from these figures that the smoothness of stress distribution across the interface validates the proper coupling between SPH particles and FEM elements.

Another field variable of importance is the damage parameter D. In Figs. 4.7a and 4.7b, the damage variable (D) contour plots are provided for the SPH model and coupled SPH-FE model respectively. The results match. Moreover, direct correspondence between the plastic strain plot Fig. 4.6 and damage variable Fig. 4.7 can be observed. The damage variable is close to unity for the region where plastic strain is more than 0.65 (value of the equivalent fracture strain, ε_f used in [22]).

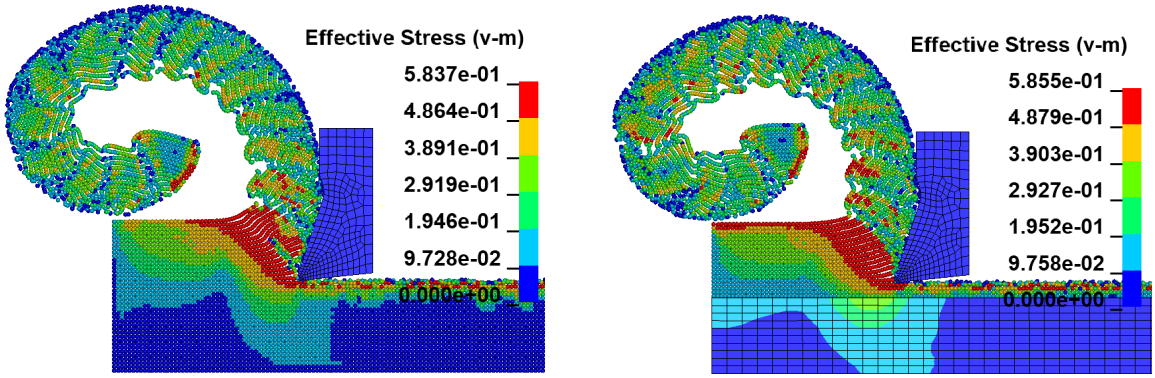

(a) SPH model. (b) coupled SPH-FE model.

Figure 4.5: von Mises stress distribution.

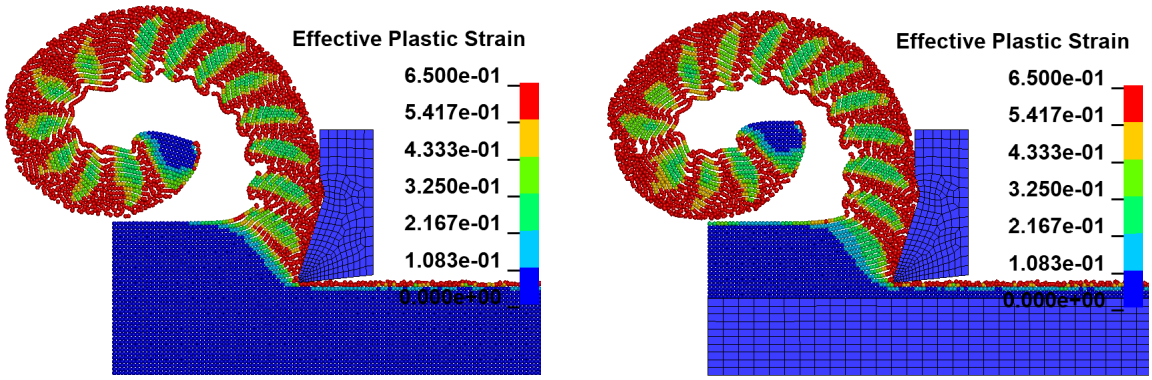

(a) SPH model. (b) coupled SPH-FE model.

Figure 4.6: Plastic strain distribution.

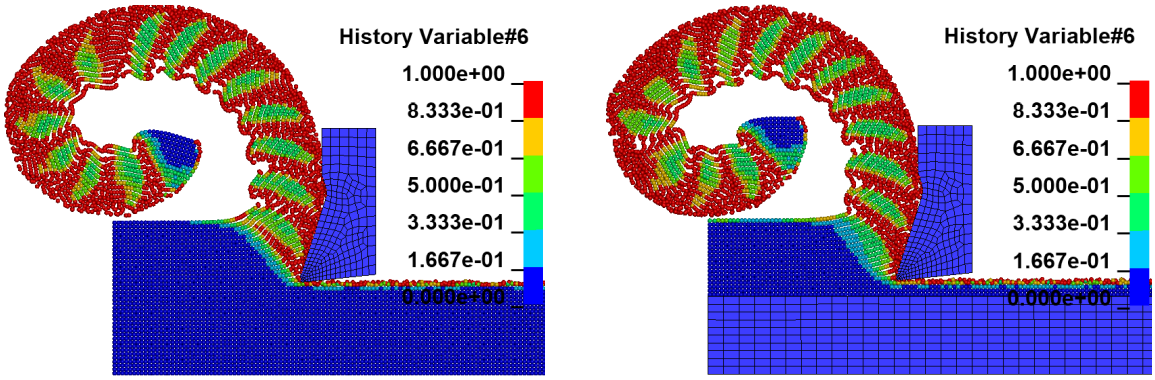

(a) SPH model. (b) coupled SPH-FE model.

Figure 4.7: Damage variable (D).

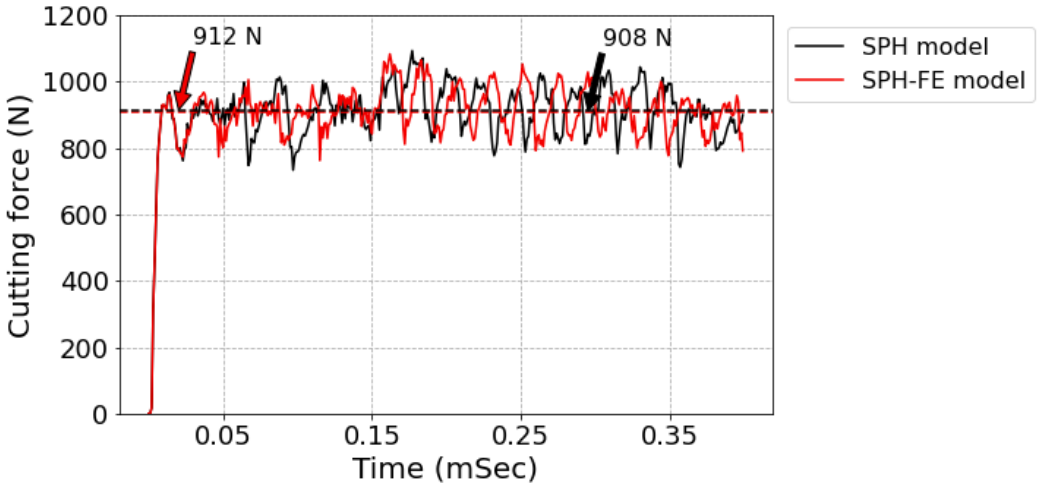

Figure 4.8: Cutting force evolution with time.

4.7.2 Cutting force

The predicted cutting forces are compared in Fig. 4.8. The average cutting force predicted by the SPH model is 908 N, whereas it is 912 N for the coupled SPH-FE model. Thus, based on these observations, it is clear that the two models provide similar results, although, in the SPH-FE problem, the number of SPH particles is approximately 50% less than that in the SPH model.

4.7.3 Simulation time

The SPH-FE model took approximately 77 minutes, whereas the SPH model took approximately 144 minutes. Clearly, the SPH-FE model offers the advantage of faster run times while predicting results almost identical to the SPH model. This benefit in computation time is because of the reduction in the number of SPH particles and the reduction in the domain size of the SPH particles in the model. The computation time increases drastically with the mesh refinement of SPH particles as shown in Table 4.3. Eight parallel processors were used for running these simulations. Thus, it can be concluded that the more realistic three-dimensional simulations of machining operations can be performed without significant loss of accuracy by using the coupled SPH-FE models while retaining the benefits of the SPH method.

Table 4.3: Simulation time with mesh refinement.

Test case	Number of SPH	Number of FE	Time (min)
Coarse SPH	18560	687	144
Coarse coupled SPH-FE	9280	1267	77
Refined SPH	62640	687	971
Refined coupled SPH-FE	31320	1267	522

4.8 Conclusion

In this study, two machining models: an SPH model and a coupled SPH-FE model, in two-dimension are developed. The SPH model has the workpiece discretized by the SPH particles. The coupled SPH-FE model has the workpiece discretized using both SPH particles (in the high deformation zones) and finite elements (in the rest of the workpiece). Numerical simulations of machining of the aluminum alloy A2024-351 are carried out using these models. The results from the SPH-FE and the fully SPH models are compared with the SPH model developed by Madaj et al.[22]. Comparisons of the chip profile, von Mises stress and plastic strain show that the SPH-FE coupled model produces results that are in close agreement with those of the fully SPH model. However, the coupled model results in a reduction of 40% in simulation time which is a significant benefit. This benefit becomes more significant for three-dimensional modeling problems where the simulations can take a prohibitively long time to complete. With the use of the coupled SPH-FE model, the domain to be discritized using SPH particles reduces. This leads to the reduction in the number of SPH particles. The reduction in the domain size has an additional advantage during the mesh refinement. This is because the mesh refinement for the SPH is done in all three directions, as the accuracy of the SPH method depends on the uniform distribution of SPH particles [50].

CHAPTER 5: PARAMETRIC STUDY

Machining modeling using smoothed particle hydrodynamics method has several parameters. These parameters can be divided into two categories, method-based and process-based parameters. Method-based parameters are the parameters used by the SPH method. Process-based parameters are the parameters related to the machining process, such as depth of cut, cutting speed and tool geometry, etc. A parametric study of these parameters is being done to obtain a robust machining model.

5.1 Method based parameters

Method-based parameters, along with their values used for the parametric study, are listed in Table 5.1. The aim of the study is to investigate the effect of these parameters and find optimum values for a numerically stable and accurate machining model.

Table 5.1: Parametric study of Method based parameters.

Parameter	**Values**
Number of SPH layers	1, 2, 3
Particle spacing	0.0125, 0.025, 0.05 mm, unequal in X and Y
Scale factor for time-step, TSSFAC	0.3, 0.6, 0.9
Artificial Bulk Viscosity	Q1= 1.5, Q2= 0.06 and Q1= 1.5, Q2= 0.5
SPH kernel function, SPHKERN	0, 1, 2, 3
Smoothing Length, hmin, hmax	default, fixed large, fixed small
Smoothing length calculation algorithm, DERIV	0, 1
SPH formulations	0, 1, 5, 6, 7, 8, 9, 10, 12

5.1.1 Number of SPH layers in Z-direction

In the SPH method, the properties of a particle are determined by the weighted sum of the properties of the neighboring particles. The number of layers of SPH particles influences the neighborhood of the particles. Also, there is a direct relationship between the number of SPH layers and the total number of SPH particles in the model. The number of SPH particles has a significant influence on the simulation time. A smaller number of particles is desirable but without the loss of accuracy of the results. Hence, studying the effect of the number of SPH layers is important.

Three simulations are run by changing the number of layers of SPH particles in Z direction (into the plane of view). The chip profiles and cutting forces are compared in Fig. 5.1 and Fig. 5.2 respectively. The results of two layers and three layers of SPH particles converge. The simulation time increases with the increase of SPH layers (Table 5.2). Based on the results, at least two layers of particles are required for having sufficient neighbors for SPH particles in the model.

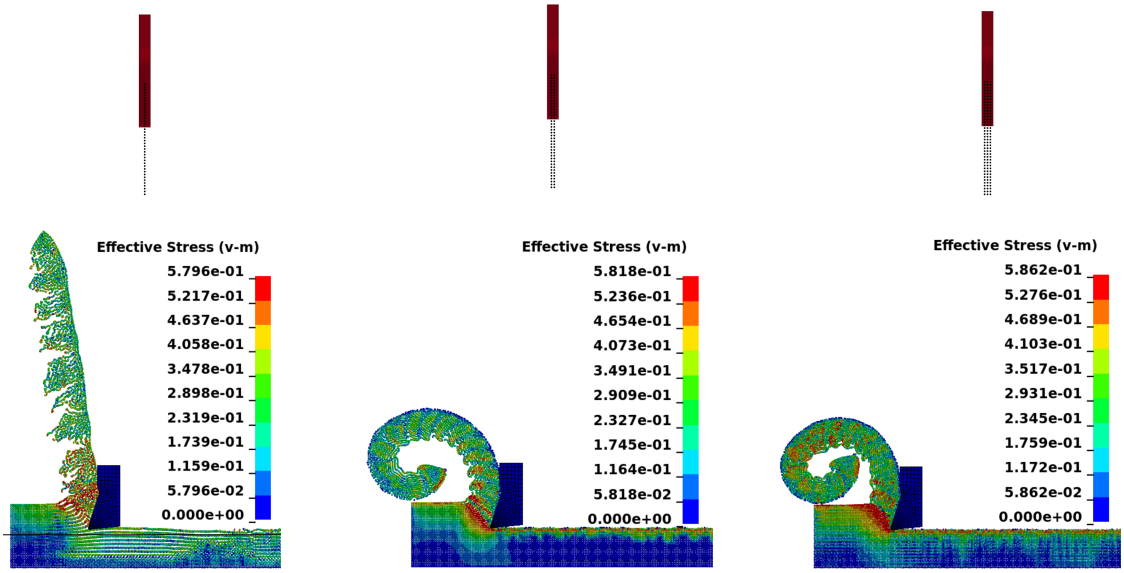

(a) 1 Layer. (b) 2 Layer. (c) 3 Layer.

Figure 5.1: von Mises stress and Chip profile with change in number of layers of SPH particles.

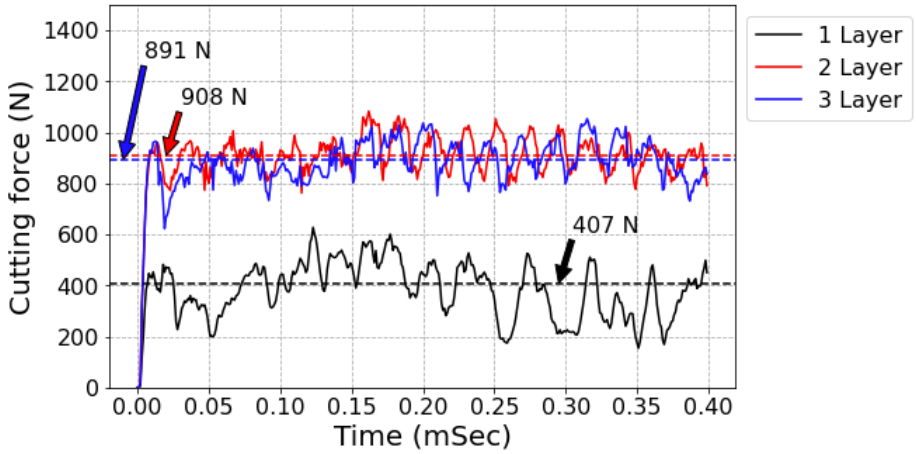

Figure 5.2: Cutting forces with change in number of layers of SPH particles.

Table 5.2: Number of SPH particles and simulation times for different layers.

Number of Layers	Number of SPH particles	Simulation time (8 processors)
1	9280	43 min
2	18560	144 min
3	27840	291 min

5.1.2 Particle spacing between SPH particles

Particle spacing between the SPH particles is similar to the element size in the Finite Element Method. The accuracy of the results depends on this parameter. Smaller distance between SPH particles not only results in the increase in the number of SPH particles but also reduces the stable time increment. A convergence study is required for the validity of the model. For the parametric study, the models with the spacing of 0.0125 mm (fine mesh), 0.025 mm (same as ref. [22]) and 0.05 mm (coarse mesh) are simulated. Also, equal spacing in horizontal and vertical directions is recommended by Monaghan [54] for better accuracy of results. This is verified using a model with 0.05 mm spacing in the horizontal direction and 0.025 mm in the vertical direction. The chip profiles and cutting forces for these models are shown in Fig. 5.3 and Fig. 5.4 respectively. As the spacing between SPH particles is reduced,

the serration in the chip is more prominent. Cutting force converges for 0.025 mm and 0.0125 mm particle spacing. The simulation times are compared in Table 5.3.

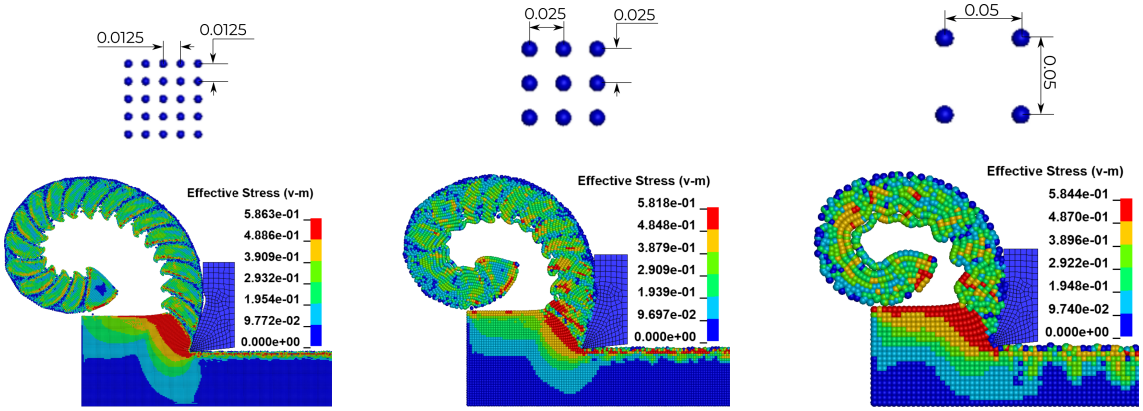

(a) Fine mesh. (b) same as Ref [22] (c) Coarse mesh.

Figure 5.3: von Mises stress and Chip profile with change in particle spacing between SPH particles.

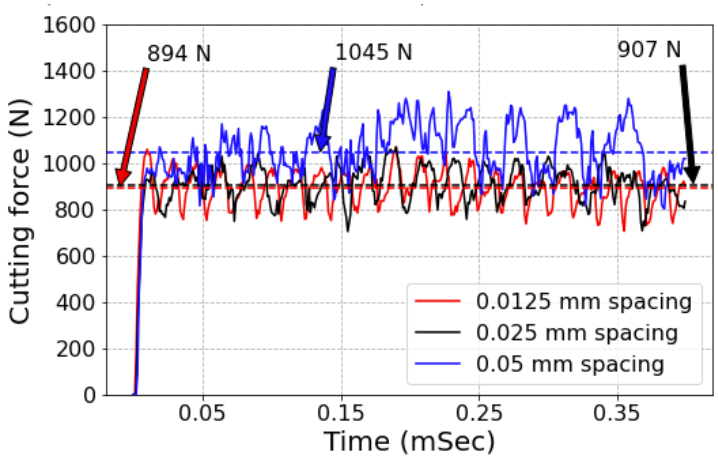

Figure 5.4: Cutting forces with change in particle spacing between SPH particles.

Table 5.3: Simulation time for different particle spacing.

Particle spacing	Number of SPH particles	Simulation time (16 processors)
0.0125 mm	74240	318 min
0.025 mm	18560	29 min
0.050 mm	4640	4 min
0.050 mm: Horizontal 0.025 mm: Vertical	9280	13 min

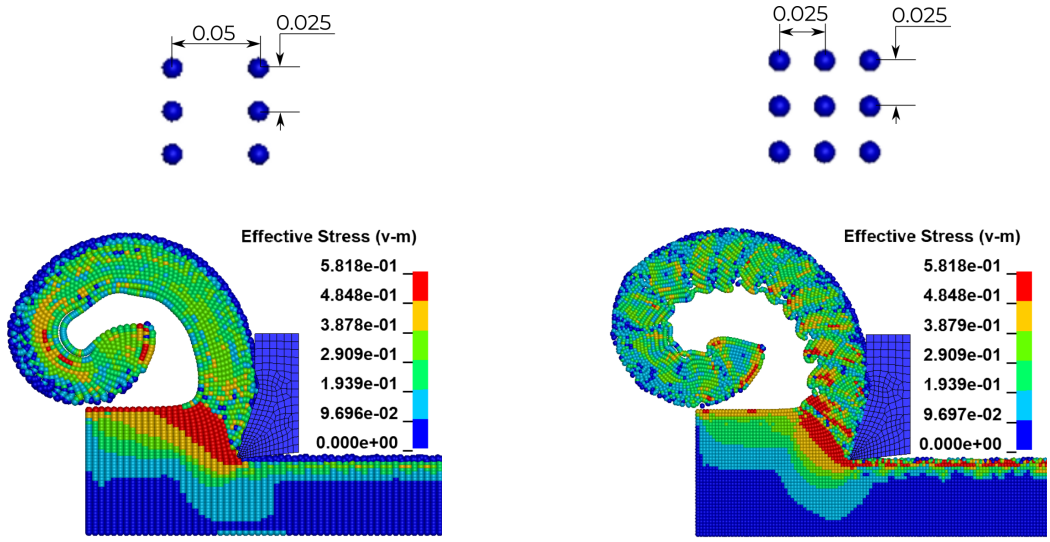

(a) Unequal SPH spacing. (b) same as Ref [22].

Figure 5.5: von Mises stress and Chip profile for unequal spacing of SPH particles.

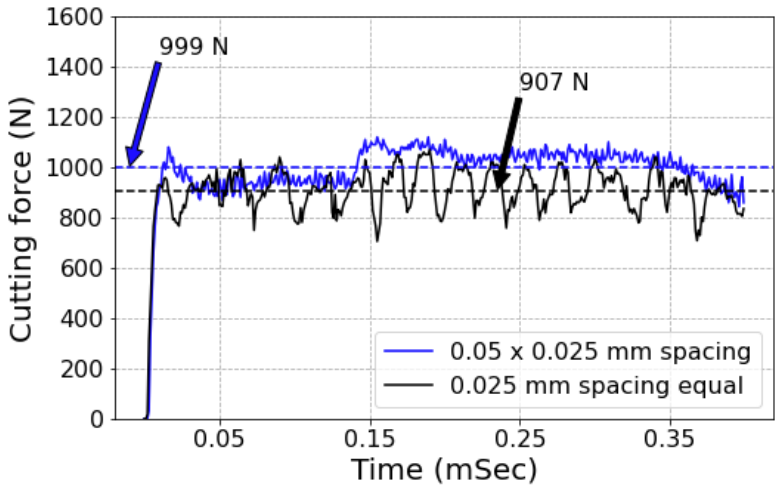

Figure 5.6: Cutting forces for unequal spacing of SPH particles.

The chip formed by the model with the unequal spacing of SPH particles is continuous (without any serration) as compared with the model with equal spacing of SPH particles (Fig. 5.5). The effect of this can be seen in Fig. 5.5. There is less fluctuation of cutting force for the model with the unequal spacing of SPH particles. However, serrations are observed in the chips formed in the experiments [1]. This confirms that the model with the equal spacing between SPH particles provide more accurate results.

5.1.3 Scale factor for computed time step (TSSFAC)

Because of the explicit nature of time stepping, the stability of the simulation depends on the chosen timestep. Courant Friedrichs-Lewy's (CFL) condition determines the smallest timestep required for a stable simulation. This time step size corresponds to the time taken by an acoustic wave to travel through the smallest characteristic distance of the elements. For the stability of the simulation, a scaling factor TSSFAC scales this timestep. The default value of TSSFAC is 0.9. However, for some applications involving contact or shock loads, the lower values are recommended in the LS-DYNA manual. But the lower values also lead to larger simulation time. Thus, determination of the optimum time step scale factor is important for accurate solutions in optimum simulation time.

Chip profiles for different TSSFAC are shown in Fig. 5.7. While the chip profiles for TSSFAC of 0.3 and 0.6 match, breaking of the chip is observed for TSSFAC = 0.9. Simulation times are compared in Table 5.4. A decrease in the simulation time is observed with increasing TSSFAC. No significant difference in the cutting forces is observed.

The timestep is also used in the calculations for the contact analysis. To avoid contact instabilities, LS-DYNA provides a limiting value for the timestep. While running the 3D simulations, this was observed in the results in the form of SPH particles flying away and a large decrease in the timestep for subsequent times. Thus, TSSFAC = 0.6 is used in further simulations to avoid these instabilities.

Table 5.4: Simulation time for different TSSFAC.

TSSFAC	Simulation time (16 processors)
0.30	33 min
0.60	17 min
0.90	11 min

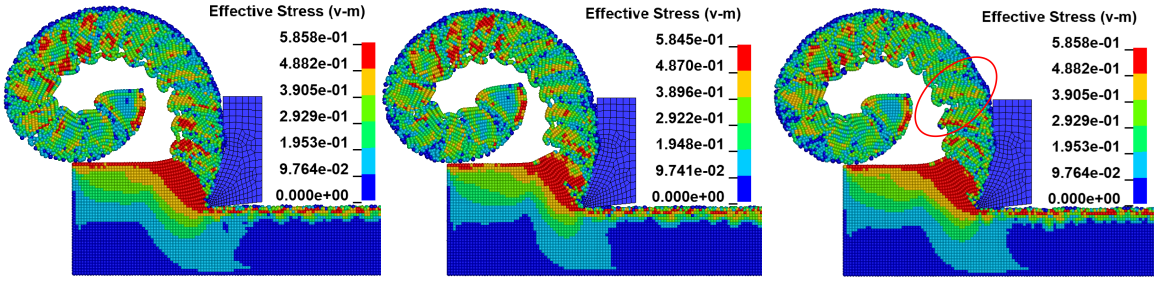

(a) TSSFAC = 0.3. (b) TSSFAC = 0.6. (c) TSSFAC = 0.9.

Figure 5.7: von Mises stress and Chip profile for different depths of cut (DOC).

5.1.4 Artificial Bulk viscosity

Artificial bulk viscosity is added to the conservation of momentum equation to stabilize the SPH method for shock wave and contact discontinuities. The default values for the two parameters defining artificial viscosity are Q1 = 1.5 and Q2 = 0.06. Espinosa et al.[39] have used Q1 = 1.5 and Q2 = 0.5. A comparison of the chip profiles for both these sets is shown in Fig. 5.8. With Q1 = 1.5 and Q2 = 0.5, the distribution of stress is smoother as compared to the model with Q1 = 1.5 and Q2 = 0.06. This result is in agreement with the observations of Espinosa et al.[39]. Thus, Q1 = 1.5 and Q2 = 0.5 is chosen for further simulations.

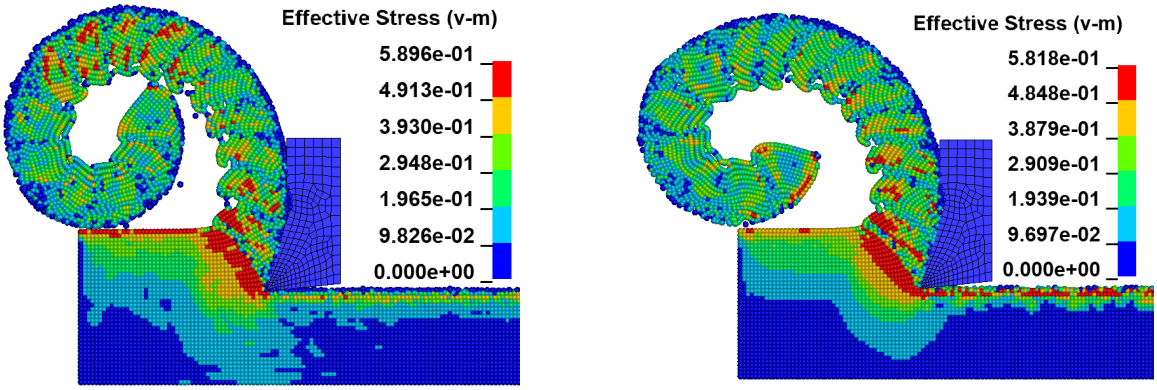

(a) Q1 = 1.5 and Q2= 0.06. (b) Q1 = 1.5 and Q2= 0.5.

Figure 5.8: von Mises stress and Chip profile for different sets of artificial viscosity.

5.1.5 SPH kernel functions (SPHKERN)

Kernel functions determine the domain of influence or neighbors of the SPH particles. The state variables of an SPH particle are determined by the weighted sum of state variables of its neighbors and the kernel function provides the weight. Thus, evaluation of the choice of the kernel function is important for the accuracy of the results.

The von Mises stress and chip profile for different kernel functions is shown in Fig. 5.9. Based on the results, there is no significant effect of the kernel function. Also, there is no significant difference in cutting forces and simulation time. Hence the default cubic spline kernel is used for further simulations.

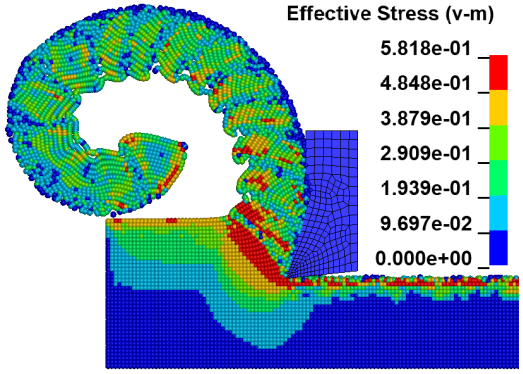

(a) SPHKERN= 0: Cubic spline.

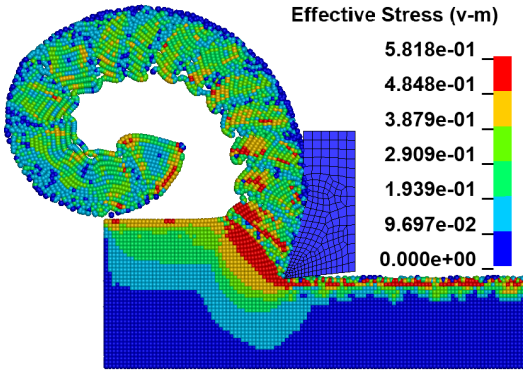

(b) SPHKERN= 1: Quintic spline.

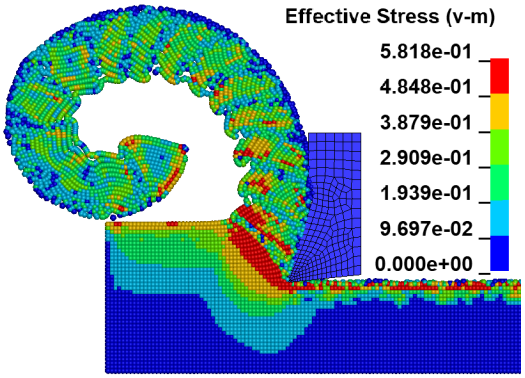

(c) SPHKERN= 2: Quadratic spline.

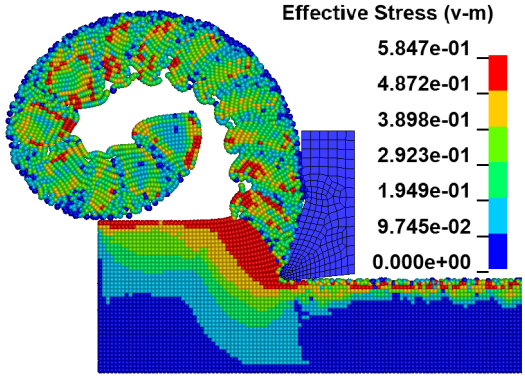

(d) SPHKERN= 3: Quartic spline.

Figure 5.9: von Mises stress and Chip profile for different Kernel functions (SPHKERN).

5.1.6 Smoothing length

Smoothing length in the SPH method determines the influence region around a particle. The particles inside this influence region or support domain are considered as the neighbors and contribute to the calculation of the state variable of the particle. During the simulation of machining, the particles move and can change the number of particles inside the influence region. To hold a constant number of particles in each neighborhood, LS-DYNA uses a variable smoothing length [55]. The smoothing length $h(t)$ is bound in the range $(H_{min} \times h_0, H_{max} \times h_0)$. Here, H_{min}, H_{max} are user-defined constants and h_0 is the initial smoothing length (recomputed every cycle for each particle based on the divergence of the velocity) [64].

The effect of variation of H_{min} and H_{max} is studied using three cases, small values are taken ($H_{min} = H_{max} = 0.2$), default values recommended in LS-DYNA and large values ($H_{min} = H_{max} = 3.0$). The chip profiles for these cases are shown in Fig. 5.10. For small values of the smoothing length constants, a small region of influence allows the particles to move freely, similar to [64]. For large constants, the chip has no segmentation and the boundary particles are observed to separate from rest of the domain. Similar inaccuracy due to the boundary effect is observed by Lee and Hong [65]. Thus for further simulations, the default values of H_{min} and H_{max} are used.

Another parameter, DERIV, defines the method of calculation of the initial smoothing length h_0. However, identical chips are observed for different options for DERIV.

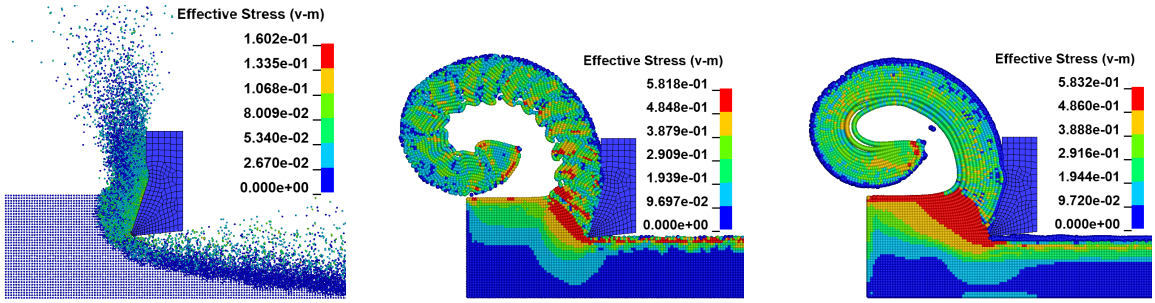

(a) $H_{min} = H_{max} = 0.2$. (b) $H_{min} = 0.2, H_{max} = 2$. (c) $H_{min} = H_{max} = 3$.

Figure 5.10: von Mises stress and Chip profile for varying smoothing length (h).

5.1.7 SPH formulations

LS-DYNA has different SPH formulations based on the applications. The formulations differ by the different definitions of the derivative operator and hence different discretization for the momentum equation. There are fifteen SPH formulations implemented in LS-DYNA [55]. Form 2 and 3 are not recommended for any case. Form 5 and 6 are used when fluid material is present or when materials with very different stiffness are used. Form 13 is an implicit incompressible fluid and used for water. Form 15 and 16 are recommended for fluid-like material applications (not for materials with failure). However, for completeness, the models are simulated with all formulations except Form 2 and 3.

The chip profile of the models with different SPH formulations available in LS-DYNA and the corresponding cutting forces are shown in Fig. 5.11 and Fig. 5.12 respectively.

The following observations are made:

1. Form 4 (tensor formulation) gave an error of SPH memory allocation.

2. Form 7 and 8 are Lagrangian formulations. They cannot endure very large deformations.

3. Cutting force for Form 1, 6 and 10 are greater than Form 0, 5 and 12.

4. Results of Form 1, 6 and 10 indicate that renormalization is required to get curled chips.

5. For further simulations, Form 1 is chosen.

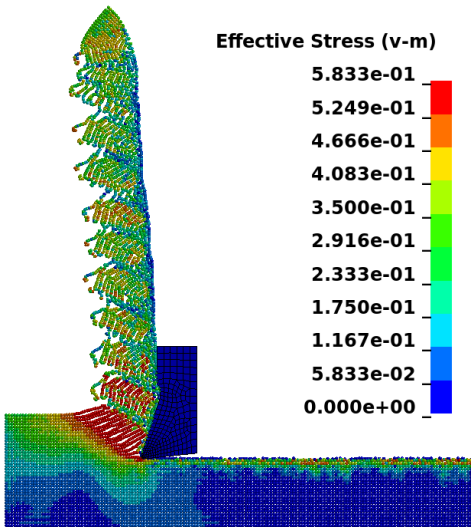

(a) Form 0: default formulation.

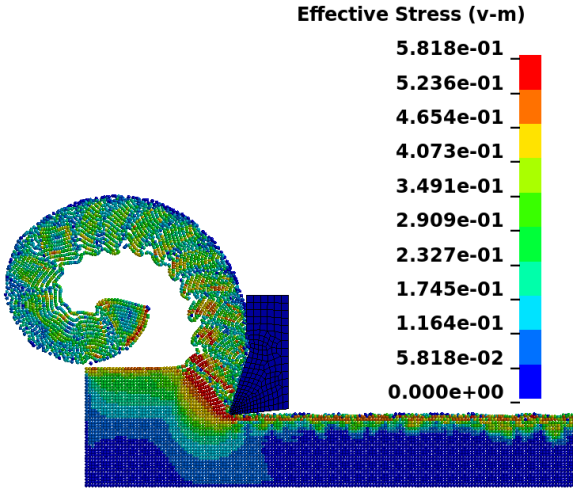

(b) Form 1: renormalization approximation.

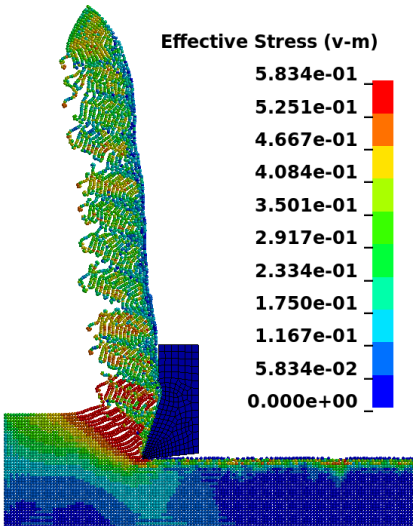

(c) Form 5: fluid particle approximation.

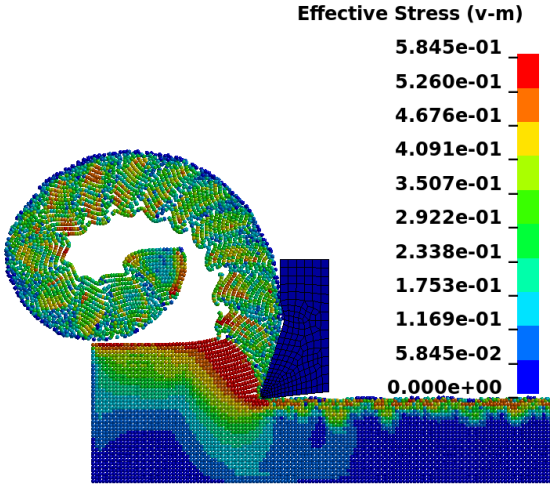

(d) Form 6: fluid particle with renormalization.

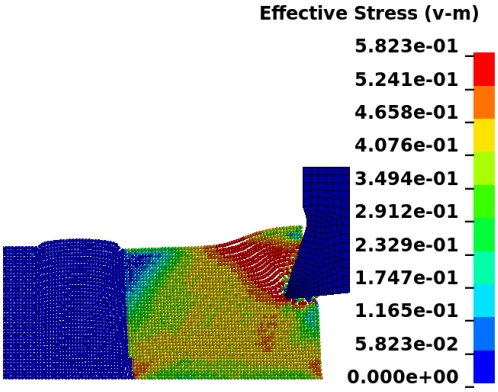

(e) Form 7: total Lagrangian form.

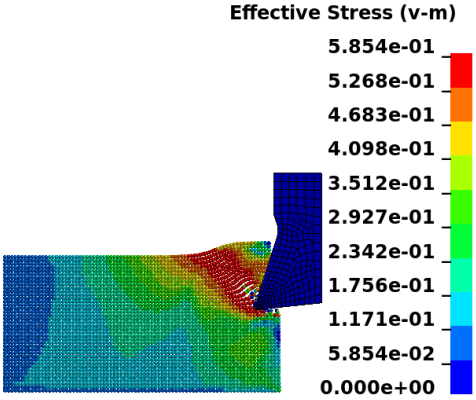

(f) Form 8: total Lagrangian with renormalization.

Figure 5.11: von Mises stress and Chip profile for different SPH formulations.

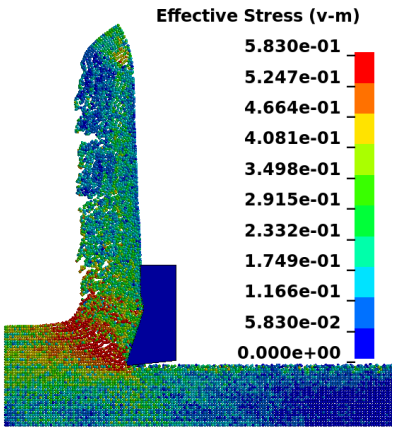

(g) Form 9: ASPH formulation.

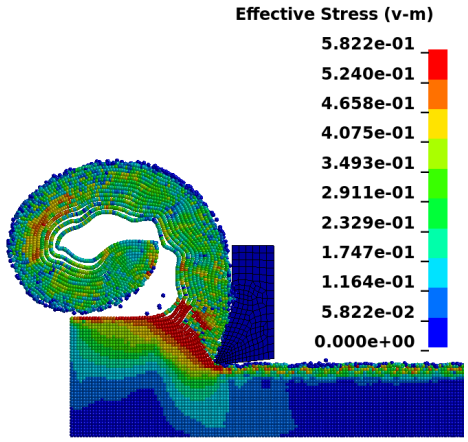

(h) Form 10: ASPH with renormalization.

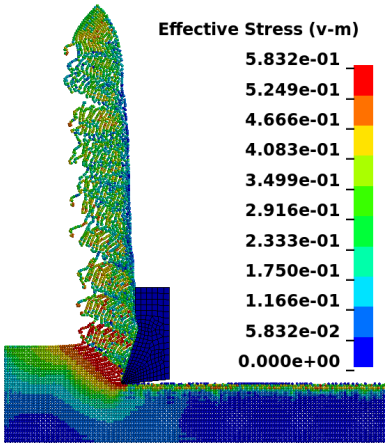

(i) Form 12: moving least-squares form.

Figure 5.11: von Mises stress and Chip profile for different SPH formulations.

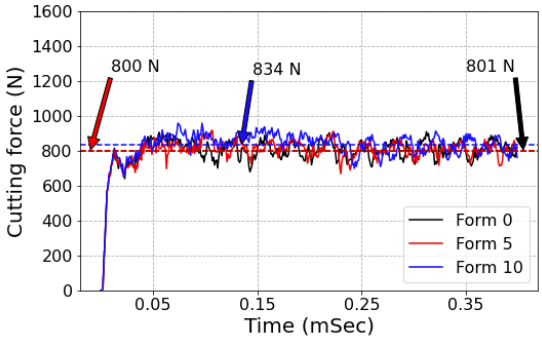

(a) Form 0, Form 5 & Form 10.

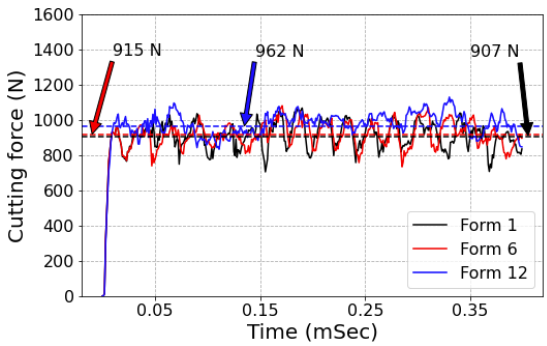

(b) Form 1, Form 6 & Form 12.

Figure 5.12: Cutting force plot for different SPH formulations in LS-DYNA.

5.2 Process based parameters

In this section, the results of the parametric study of process-based parameters are discussed. Understanding the effect of these parameters on machining conditions such as cutting force is important to have a reliable predictive capability. The process-based parameters and their corresponding values used in the parametric study are listed in Table 5.5.

Table 5.5: Parametric study of Process based parameters.

Parameter	**Values**
Depth of cut	0.2, 0.4, 0.6 mm
Cutting speed	400, 800, 4000, 8000 m/min
Rake angle	-5°, 0°, +5°, +17°
Friction coefficient	0.9, 0.5, 0.17, 0
Strain at Fracture	0, 0.2, 0.65, 1.5

5.2.1 Depth of cut

To investigate the effect of depth of cut during machining, a parametric study with three values of depth of cut, namely 0.2, 0.4 and 0.6 mm, is conducted. Chip profiles for these conditions are shown in Fig. 5.13. Also the cutting forces are compared in Fig. 5.14. As the depth of cut increases, the chip profile changes from continuous to serrated. The cutting force increases with the depth of cut. At a depth of cut = 0.6 mm, the variation of the cutting force increases due to chip serration.

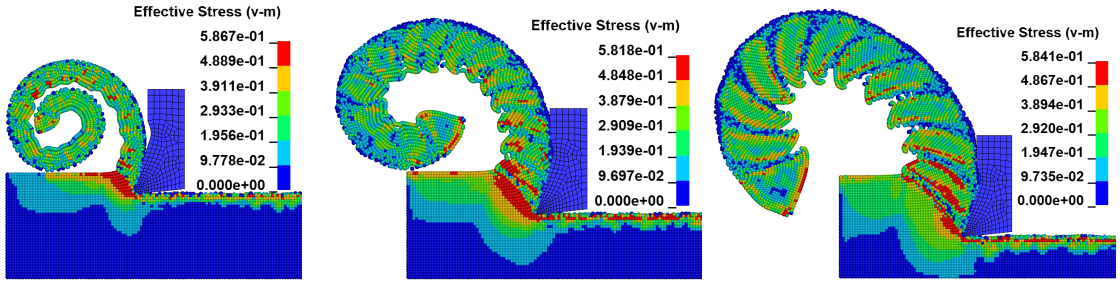

(a) Depth of cut= 0.02 mm. (b) Depth of cut= 0.04 mm. (c) Depth of cut= 0.06 mm.

Figure 5.13: von Mises stress and Chip profile for different depths of cut (DOC).

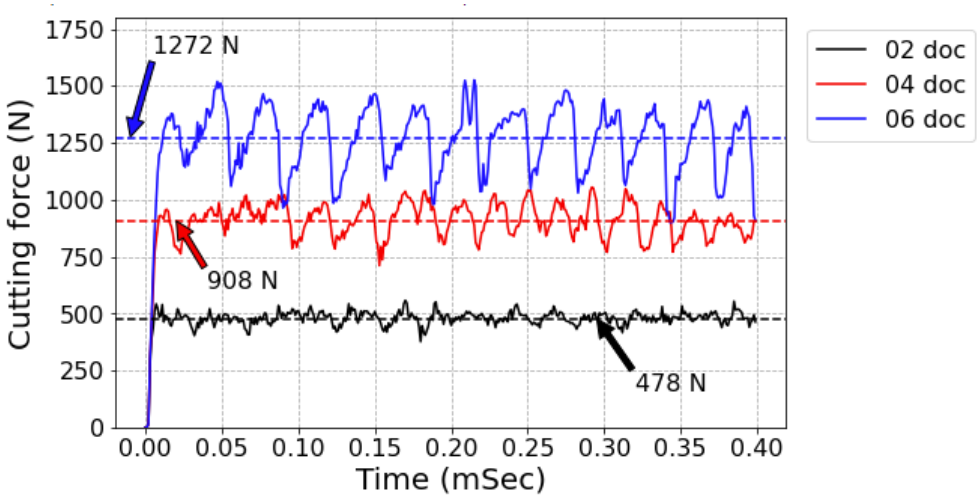

Figure 5.14: Cutting forces comparison for different depths of cut (DOC).

5.2.2 Cutting speed

To investigate the effect of cutting speed, a parametric study with cutting speeds of 400, 800, 4000 and 8000 m/min, is conducted. Although high values of the cutting speed, such as 8000 m/min, are not practical, this is chosen to verify the use of increasing the cutting speed in the simulation to reduce the simulation time [39, 66].

The chip profiles and the cutting forces for these conditions are shown in Fig. 5.16 and Fig. 5.15 respectively. It is observed that as the cutting speed increases, the curl radius of the chip increases. Also, the cutting force shows an increasing trend with increasing cutting speed. However, the increase in chip curl and cutting force is not significant until the cutting speed of 4000 m/min. Increasing the cutting speed leads to the reduction of the simulation time. However, a parametric study needs to be conducted for accurate modeling.

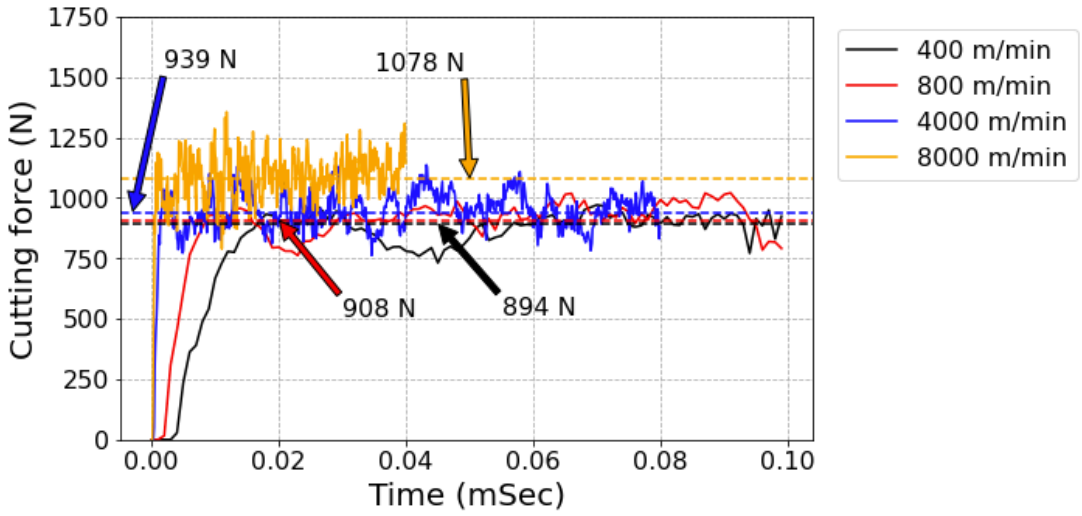

Figure 5.15: Cutting forces comparison for different cutting speeds.

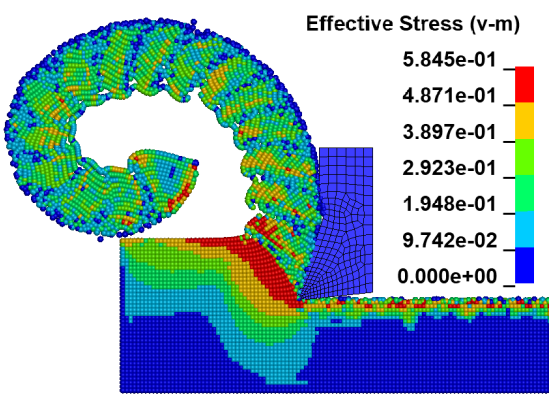

(a) Cutting speed= 400 m/min.

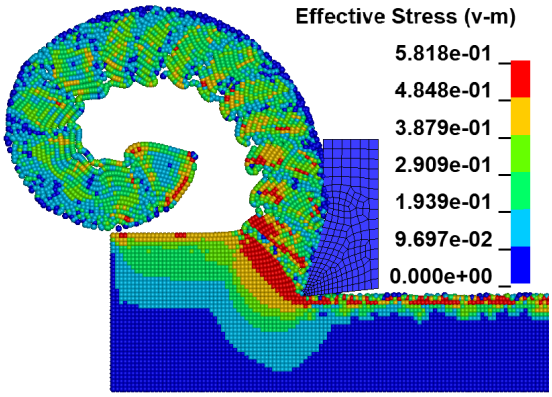

(b) Cutting speed= 800 m/min.

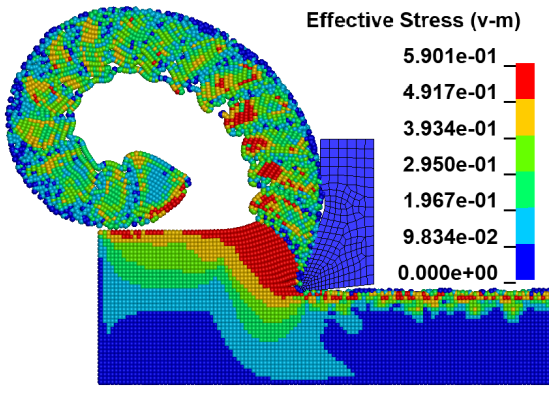

(c) Cutting speed= 4000 m/min.

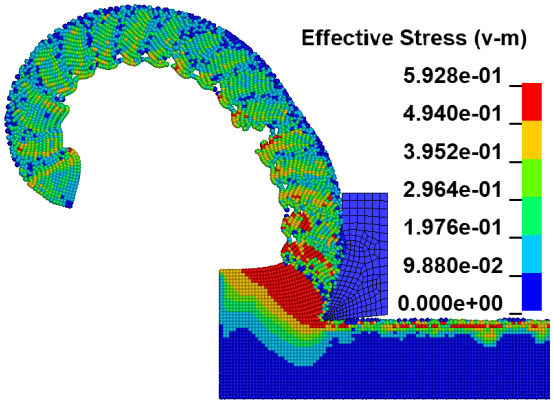

(d) Cutting speed= 8000 m/min.

Figure 5.16: von Mises stress and Chip profile for different cutting speeds.

5.2.3 Rake angle

The rake angle of the tool is an important consideration during the selection of tools for machining. Cutting forces, temperature and chip profile are dependant upon the rake angle [67]. To understand the effect of rake angle, the machining models with -5, 0, +5 and +17 ° rake angle are simulated. The chip profiles and cutting forces are shown in Fig. 5.17 and 5.18 respectively. With increasing rake angle, the serration in the chips decreases and the cutting force decreases. Also, the fluctuation in the cutting force plot decreases.

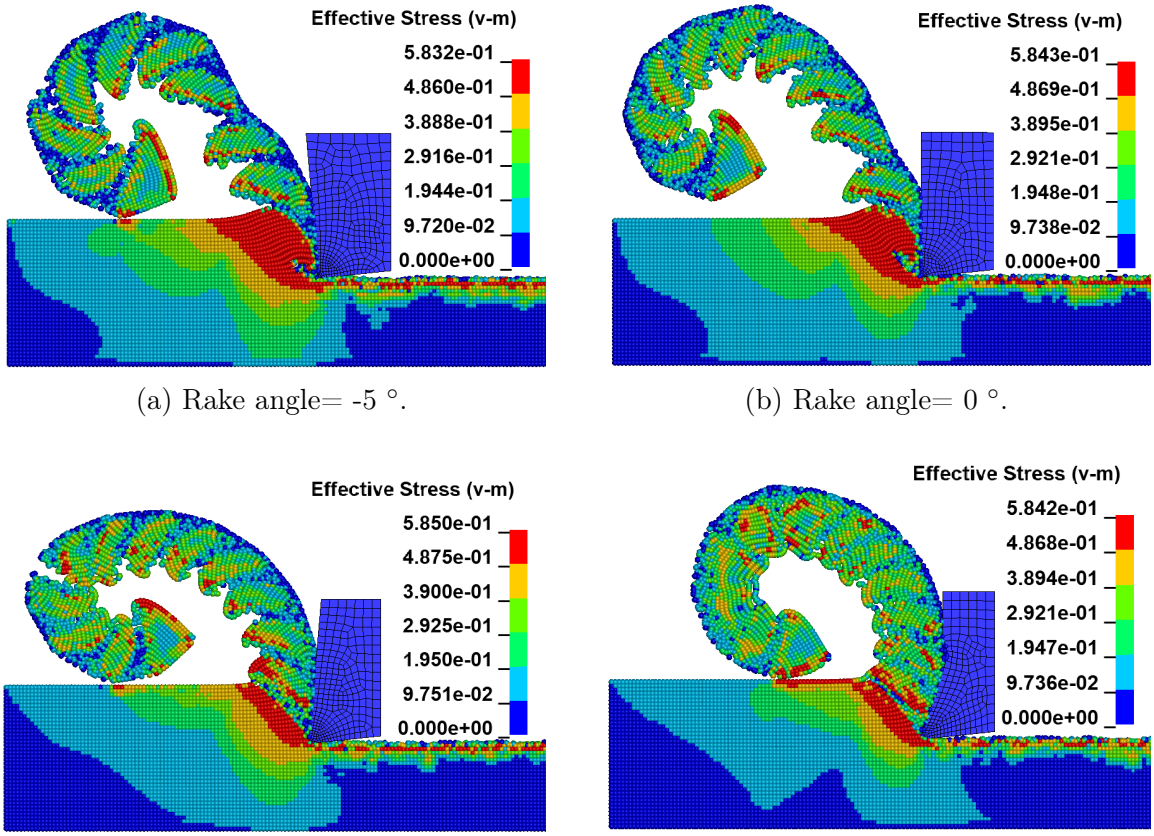

(a) Rake angle= -5 °. (b) Rake angle= 0 °.

(c) Rake angle= +5 °. (d) Rake angle= +17 °.

Figure 5.17: von Mises stress and Chip profile for different rake angles.

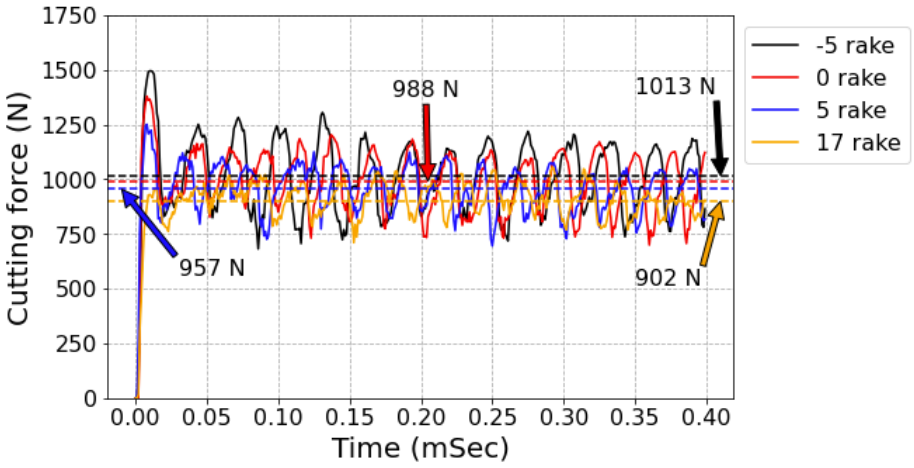

Figure 5.18: Cutting forces comparison for different rake angles.

5.2.4 Friction

During machining, frictional forces are present at the interface of the tool and the workpiece. Friction in LS-DYNA is based on a Coulomb formulation [55]. The coefficient of friction μ is defined by the user while defining the contact. A parametric study is conducted for three values of friction coefficient, μ, to investigate the effect of friction on the results. No significant difference in the chip profiles is observed. However, the cutting force (shown in Fig. 5.19) increased by increasing the value of the friction coefficient. Thus, the friction coefficient can be used as a calibrating parameter to correlate simulation results with experimental observations.

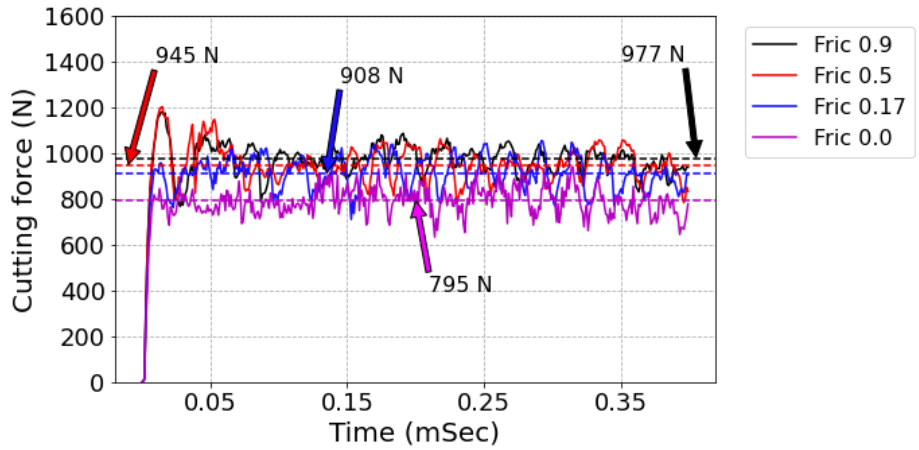

Figure 5.19: Cutting forces comparison for different friction coefficient.

5.2.5 Strain at Fracture

A fracture occurs in a material when the cumulative plastic strain equals a parameter called the strain at fracture. This is a material dependant parameter. A parametric study is conducted for four values of this parameter to investigate the effect on the simulation results. The chip profiles and cutting forces are shown in Fig. 5.20 and 5.21 respectively. As the value of the strain at fracture increases, the chip profile changes from serrated and broken to continuous. Also, with the increase of this parameter, the cutting force increases and has less fluctuation. Thus, this parameter is critical to tune to correlate simulation results with the experimental observations.

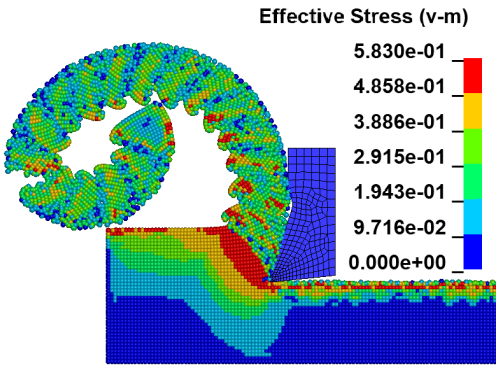

(a) $Ef_{min} = 0.$

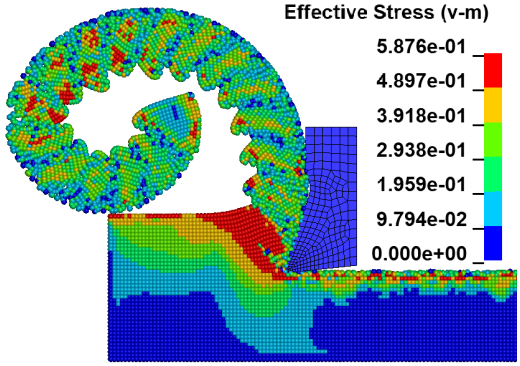

(b) $Ef_{min} = 0.20.$

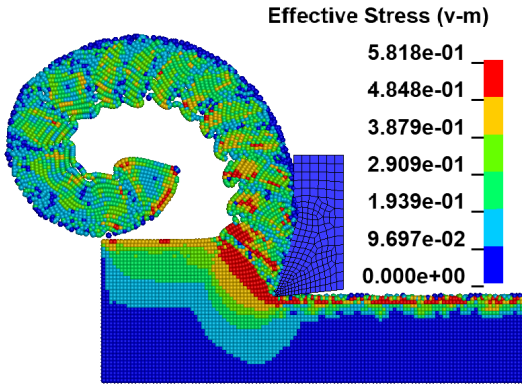

(c) $Ef_{min} = 0.65.$

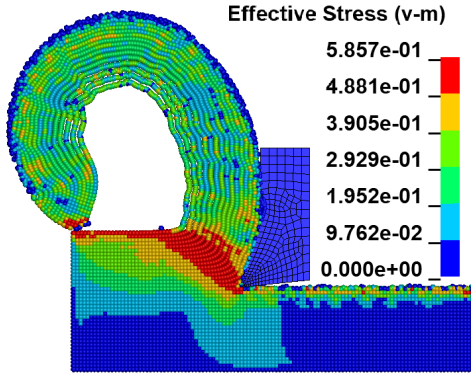

(d) $Ef_{min} = 1.5.$

Figure 5.20: von Mises stress and Chip profile for different values of Strain at fracture.

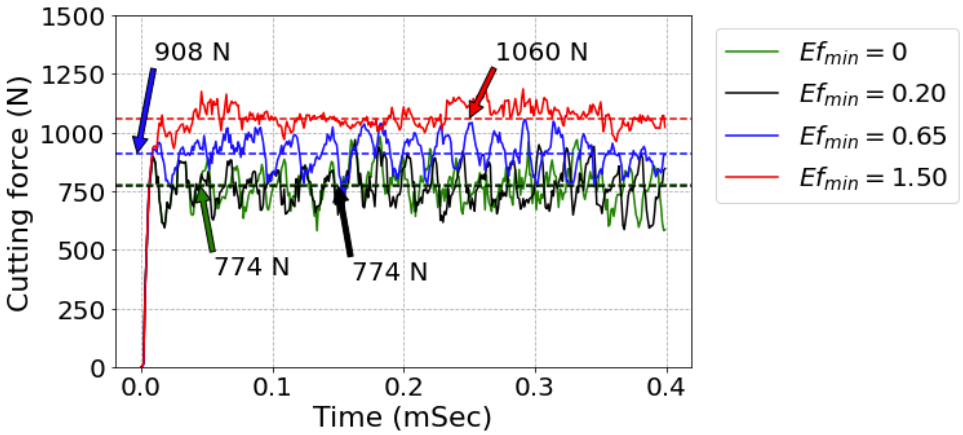

Figure 5.21: Cutting forces comparison for different values of Strain at fracture.

5.3 Conclusion

Insight is gained into the parameters of the SPH method through the parametric study. This insight leads to the enhanced robustness of the computational model for machining. The following are some of the important conclusions of the study:

1. Curled chips are obtained while using the renormalization approximation formulation of SPH. Straight chips are obtained when the default formulation is used.

2. A minimum of two layers of SPH particles is required to model the orthogonal machining accurately.

3. While choosing the value of the parameter, Scale factor for timestep, TSSFAC, merely satisfying the CFL criteria is not enough. The upper limit of the timestep defined for the contact is also essential for the stability of the model.

4. The values of the friction coefficient and strain at fracture need to be tuned to correlate the simulated forces with the experimentally measured forces.

CHAPTER 6: 3D MACHINING MODEL

Computational modeling is an important tool to understand the complex physics of machining and optimize the machining process. However, the majority of the current studies focus on the 2D plane strain orthogonal machining model because of its simplicity. The predicted cutting force aligns well with the experimental values. However, the thrust force is highly underpredicted. Also, the axial force cannot be predicted using this model. Very few studies [44–48] incorporate the 3D machining model. Even in these studies, only a section of the workpiece has been modeled. Although the cutting forces may stabilize, the chip profile associated with the actual machining operation cannot be predicted. The industrial machining operations are predominantly 3D in nature. Hence, to predict the physical variables such as stresses, strains and temperature for these operations, a more realistic 3D machining model is needed. In this chapter, machining models with a full-scale 3D model of the workpiece are simulated. The aim is to predict all the three components of the cutting forces and the chip morphology during machining by modeling. The results of the simulation are compared with the experimental observations.

6.1 Model description

The machining model, shown in Fig. 6.1, consists of a tool and a cylindrical workpiece. The tool is discretized using finite element mesh and the workpiece is discretized using a coupled SPH-FE mesh. This is done to reduce the simulation time, as the SPH method is computationally expensive. The SPH particles are used in the zone of cutting, where the workpiece interacts with the tool. This is a zone of high deformation. The chip forms, curls and comes in contact with itself and the

surface of the tool. A Finite element mesh is used away from this zone, where the deformations are less. All the boundary conditions are applied to the finite element mesh. The SPH and FE mesh are coupled at the interface. This coupling allows smooth transfer of the physical properties, such as displacement and stress. The geometry and mesh of the tool and the workpiece are shown in Fig. 6.2 and Fig. 6.3 respectively. All length dimensions are in mm.

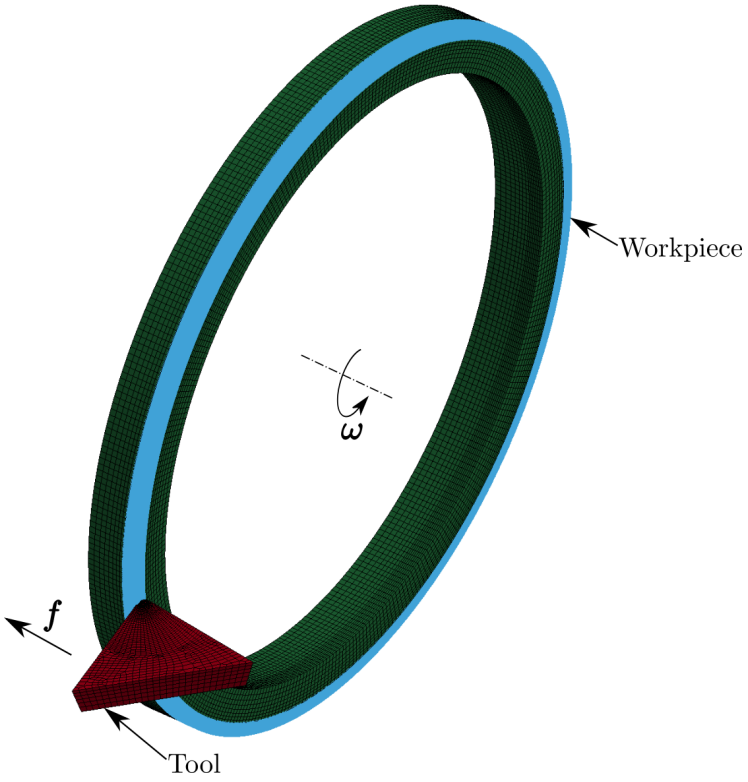

Figure 6.1: Machining model used for 3D machining.

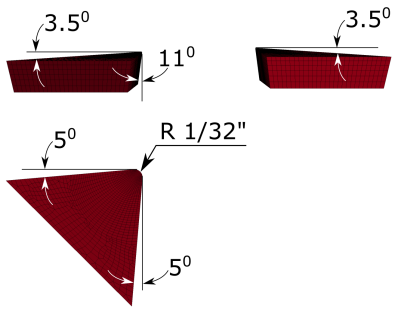

Figure 6.2: Geometry of the tool used used in 3D machining model.

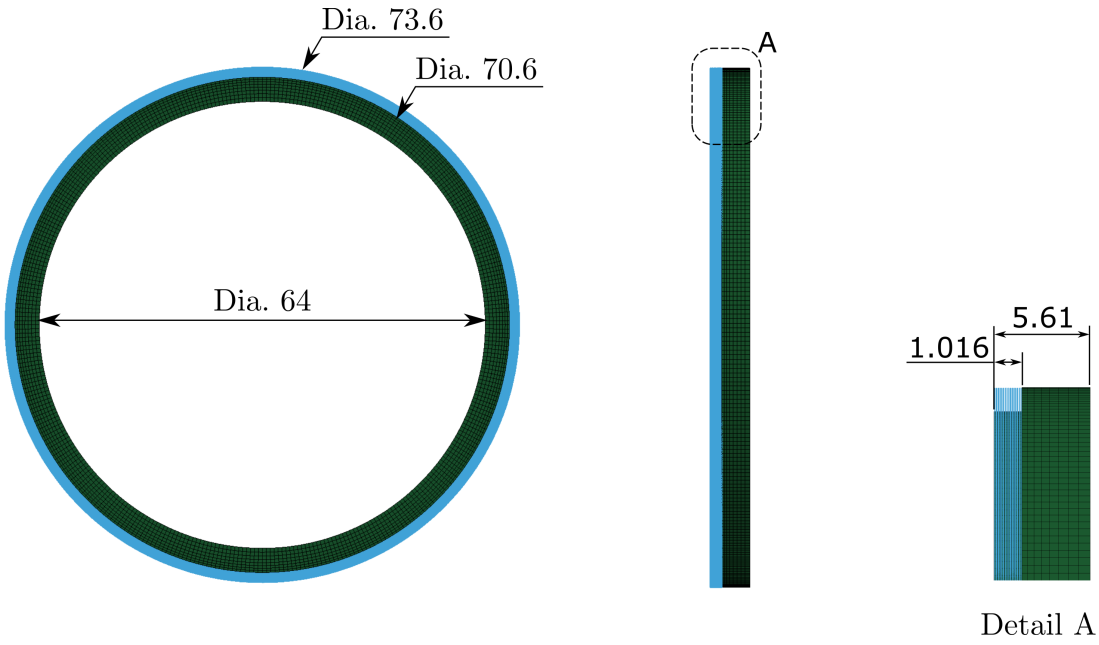

Figure 6.3: Geometry of the workpiece used in 3D machining model.

6.2 Material properties

The material of the tool is tungsten carbide, and that of the workpiece is Al 6061. The physical properties of the tool and the workpiece are shown in Table 6.1. The tool is modeled as a rigid body. This simplification is based on the fact that the tool's rigidity is comparatively much greater than the material of the workpiece. For modeling, the workpiece and its fracture in the form of chips, the Johnson-Cook material model with the Johnson-Cook damage model are used. The parameters of the material model of the workpiece are shown in Table 6.2.

Table 6.1: Physical properties of Workpiece and Tool [2].

Property	Workpiece	Tool
Density, ρ (Kg/m^3)	2700	11900
Young's Modulus, E (GPa)	68.9	534
Poisson's ratio, μ	0.33	0.22
Specific heat, C_p (J/Kg K^{-1})	896	-
T_{melt}, (K)	855	-
T_{room}, (K)	300	300

Table 6.2: Johnson-Cook parameters of workpiece (Al6061) [3, 4].

Parameter	A (MPa)	B(MPa)	n	C	m
Value	324	114	0.42	0.002	1.34
Parameter	D1	D2	D3	D4	D5
Value	-0.77	1.45	-0.47	0	1.6

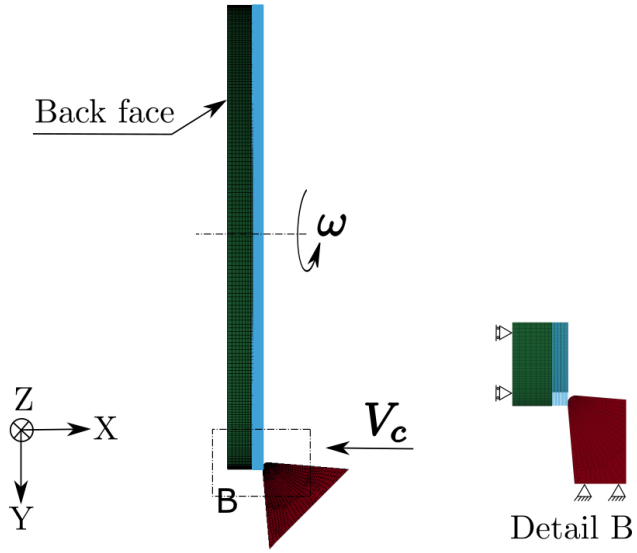

Figure 6.4: Boundary conditions used in 3D machining model.

6.3 Boundary conditions

The boundary conditions for the three-dimensional machining model are applied to the tool and the workpiece. All nodes of the tool are fully constrained in Y and Z directions. The cutting velocity, V_c is given in X direction. This velocity is calculated from the feed/revolution of the tool and the rotational speed of the workpiece. The boundary conditions on the workpiece are applied on the back face of the workpiece. All nodes on the back face are constrained to rotate along its centerline axis. Also, they are constrained for translation in X direction. Coupling of the SPH and FE mesh is done at the interface in the workpiece for smooth transfer of physical quantities. The boundary conditions are shown in Fig. 6.4.

The boundary conditions used for the two-dimensional machining model is similar to the one applied in the previous chapter. The workpiece is modeled as a rectangular box. A Plain strain condition is assumed for this model. The geometry and the boundary condition are shown in Fig. 6.5. The tool is given the cutting velocity in the negative X direction and is completely constrained in all other directions. The workpiece is fully constrained on the left and bottom sides. For the plane strain assumption, the motion of all the SPH particles and FEM elements of the workpiece and tool is fully constrained in the Z direction (normal to the plane).

6.4 Machining experiments

Haas TL-1 computer numerically controlled (CNC) lathe (8.9 kW, 2000 rpm spindle) is used as a testbed for the experiments. Cylindrical workpieces of 6061-T6 aluminum are machined with the prescribed depth of cut 1 mm and feed rate of 0.254 mm/rev. The cutting tool used is Kennametal part number 1183375 (ANSI catalog number CPGN 120308 KC730). The tool geometry consists of 80° parallelogram carbide inserts with a positive 3.5° rake angle. The insert was replaced once the measured flank wear width reached 0.3 mm to eliminate the possibility of corrupt data due to a worn cutting insert. A photograph of the setup is shown in Fig. 6.6.

Dynamic cutting forces are measured using a three-axis dynamometer (Kistler 9257B) which is mounted on the lathe's cross slide. An infrared camera (FLIR E40) is

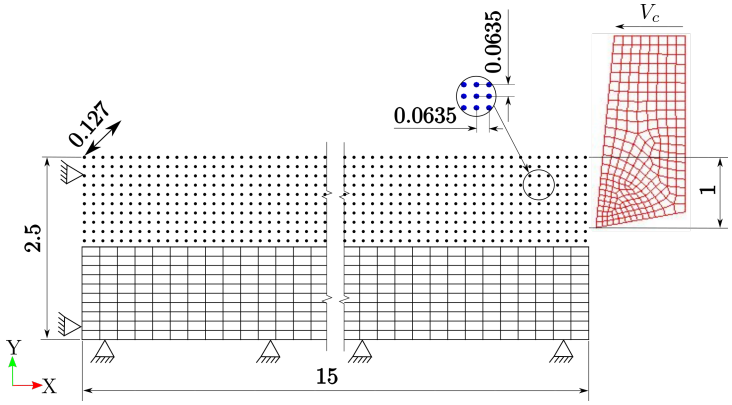

Figure 6.5: 2D Machining model.

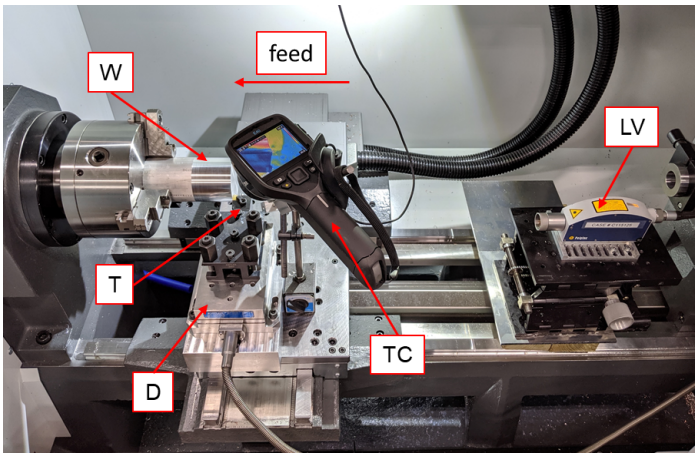

Figure 6.6: Photograph of turning setup including workpiece (W), dynamometer (D), cutting tool (T), thermal camera (TC), and laser vibrometer (LV).

attached to the cross slide to establish temperature trends with changes in machining conditions. A laser vibrometer (Polytec OFV-534/OFV-5000) is used to measure the feed direction motion (Z direction) to verify the actual feed rate during machining. A digital microscope (not pictured) is used to measure insert flank wear at a fixed location between machining tests.

6.5 Results

6.5.1 2D machining simulation

Initially, the 2D machining model is simulated. Cutting forces and chip profile are the output parameters. Although the assumptions of the plane strain conditions are not satisfied, the 2D machining models are simulated to quantify the deviation of forces from the experimental values. The simulated chip profile (shown in Fig. 6.7) is continuous, which is typically observed during the machining of Al 6061 workpieces. A comparison of the cutting forces with the experimental values is shown in Table 6.3. The cutting force is underpredicted by 45%. The thrust force is highly underpredicted (as observed in [5-8]). Also, the axial force cannot be predicted using this model. As a result, the total force (resultant of forces in all the three directions) is highly underpredicted.

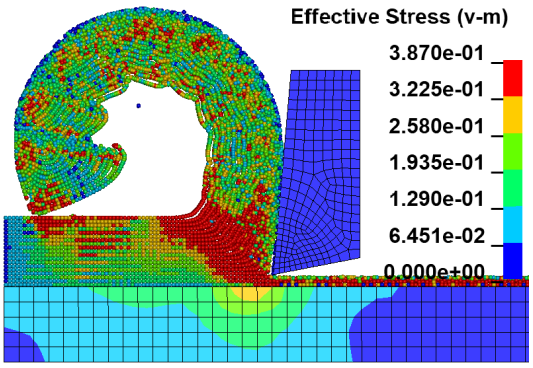

Figure 6.7: Chip profile (2D machining model).

Table 6.3: Comparison of forces predicted by 2D model with experiments.

	Experimental (N)	Simulated (N)
Axial Force (F_X)	100	-
Radial Force (F_y)	65	19
Cutting Force (F_z)	235	120
Total Force (F)	264	121

Based on the above result, it is clear that the 3D machining model is required for simulating the machining of the cylindrical workpiece. However, the 3D machining model is computationally expensive due to the large number of SPH particles ($\approx$ 323,000 particles). A commonly used approach is to reduce the simulation time is to increase the cutting speed [39, 66]. A convergence study is done using the 2D machining model for validating this approach. The cutting speed is increased by five times (5X), 10X, and 20X from the actual speed and the deviation in cutting force at the higher speed is compared with that obtained at the actual speed. The plot of cutting force for these speeds is shown in Fig. 6.8. From the plot, it is concluded that increasing the speed up to 5X has no significant influence on the cutting force. Also, the chip curls less at 10X speed. The cutting force increases at higher cutting speeds. With higher cutting speed, the strain rates increase, leading to the increased flow stress and hence higher cutting force. Thus, all further simulations are done at 5X (five times the actual cutting speed).

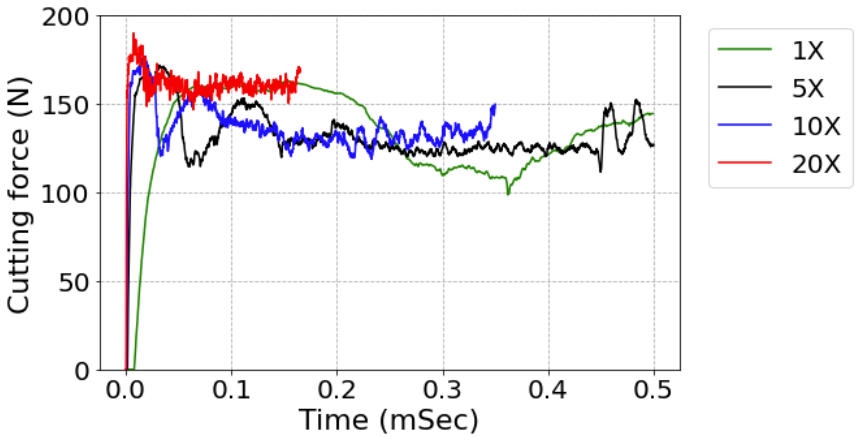

Figure 6.8: Cutting force comparison at different speeds.

6.5.2 Convergence study for 3D machining model

A convergence study for three-dimensional machining model is conducted by increasing the number of SPH particles in the model. The cutting force with time and the chip profile are considered as the output parameters for the convergence. The terminology followed is that the number of rows of SPH in feed direction per revolution is taken as a measure of the number of SPH particles. For example, for the 2.0 particle (shown in Fig.6.9), the tool will cut the first two rows of particles and touch the third row after one revolution of the workpiece. The models with 1.0 particles, 1.5 particles, 2.0 particles and 2.5 particles are simulated for the convergence study.

The plot of the cutting force is shown in Fig.6.10. For a smaller number of particles, the cutting force fluctuates and does not reach a steady state. This fluctuation is the most for 1.0 particle model and reduces for the model with the higher number of SPH particles. The cutting force converge for the 2.0 particle model and 2.5 particle model. Similar observations are made from the comparison of the chips formed by the different models. While the small chips are observed for the 1.0 particle model, the long, continuous chips are observed for 2.0 particle model and 2.5 particle models. Thus, the 2.0 particle model is taken as the model with the converged result.

The computation time for each of these models are given in Table 6.4.

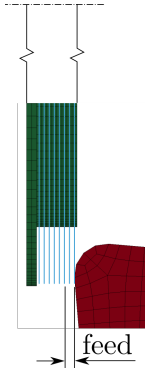

Figure 6.9: Terminology for number of SPH particles.

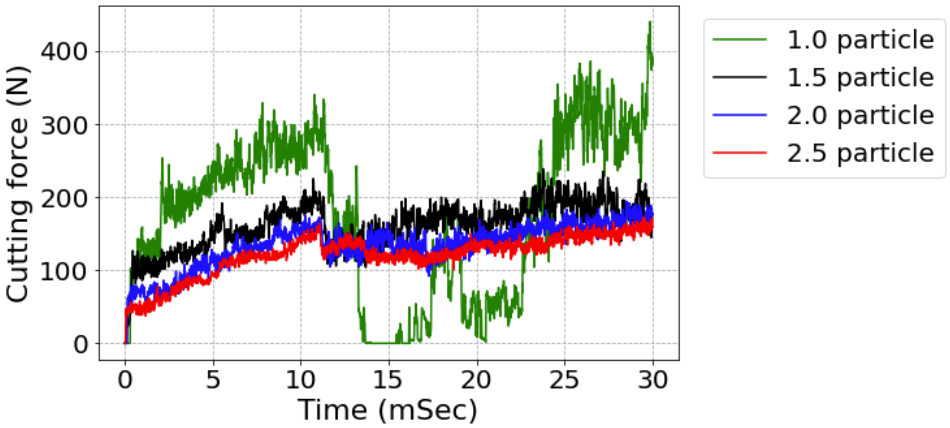

Figure 6.10: Convergence plot for cutting force.

6.5.3 3D machining simulation

A comparison of the simulated cutting forces in all three directions with the experimental values is shown in Fig. 6.11. As the tool approaches the workpiece, the cutting area of the workpiece increases. This leads to an increase in the cutting forces. The forces stabilize as the cutting area becomes constant after some time.

Table 6.4: Convergence study: Number of SPH particles and the simulation time.

Particle/feed	Number of Particles	Run time	Processors
1.0	43,708	7.25 hrs.	144
1.5	101,952	24.50 hrs.	144
2.0	192,280	64.75 hrs.	144
2.5	323,232	183.50 hrs.	144

The simulated cutting forces are summarized and compared with the experimental values in Table 6.5. While the axial and radial forces match well with the experiment values, the cutting force is under-predicted by 23%. The difference between the total simulated force and experimental value is $\sim -17\%$. Various factors such as the material model, the friction coefficient between tool and the workpiece and measurement uncertainties during experiments may contribute to this deviation.

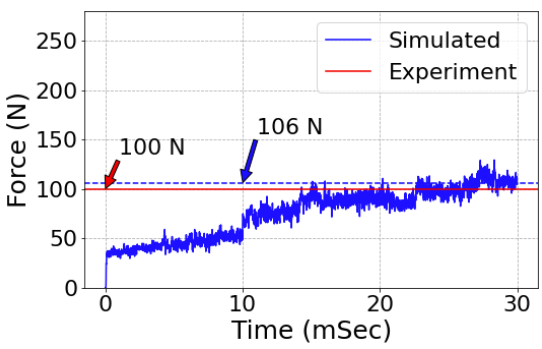

(a) Axial force (F_a)

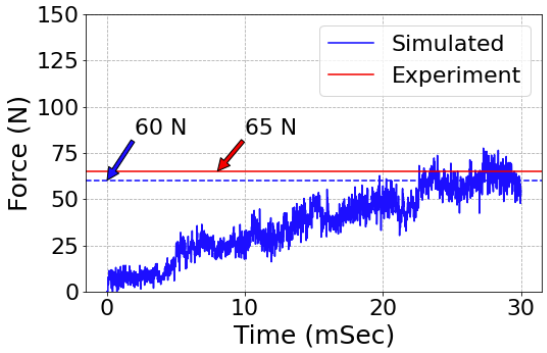

(b) Radial force (F_r)

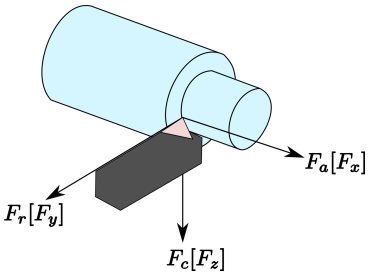

(c) Force directions

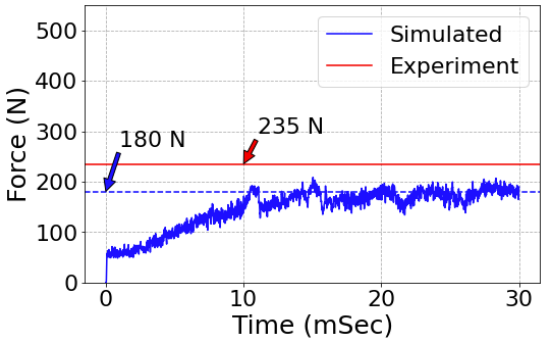

(d) Cutting force (F_c)

Figure 6.11: Cutting forces plot for 3D machining model.

Table 6.5: Comparison of forces predicted by 3D model with experiments.

	Experimental (N)	Simulated (N)
Axial Force (F_X)	100	106
Radial Force (F_y)	65	60
Cutting Force (F_z)	235	180
Total Force (F)	264	219

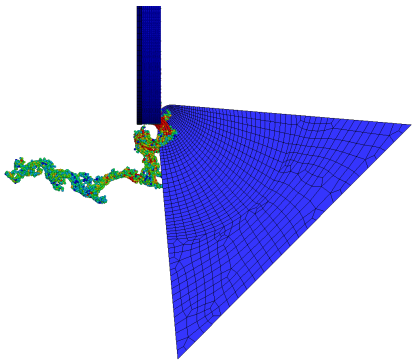

(a) Initial chip: simulated

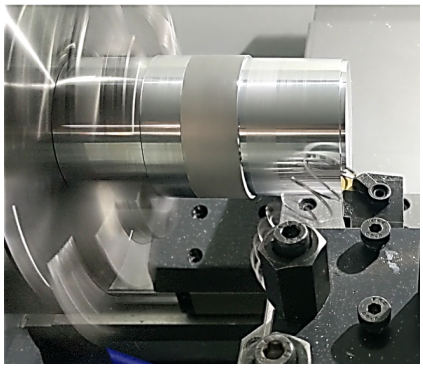

(b) Initial chip:experimental

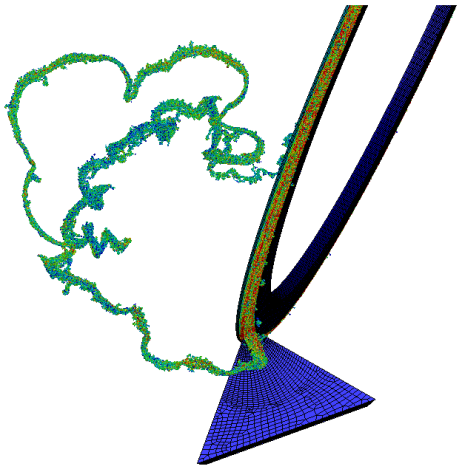

(c) Chip at later time: simulated

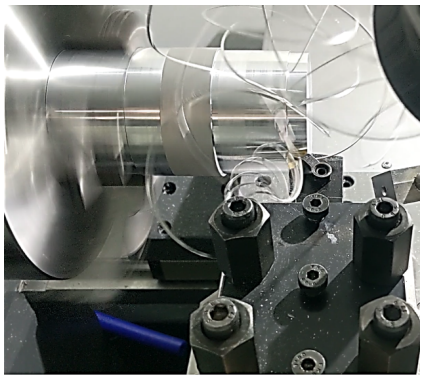

(d) Chip at later time: experimental

Figure 6.12: Comparison of simulated chip morphology with experiment.

A comparison of the chip shape obtained by the simulation with the experiment is shown in Fig. 6.12. At the initial time, the direction of chip formation matches with the experimental observations (6.12a, 6.12b). A long continuous chip is obtained in the simulation at a later time (Fig 6.12c, 6.12d). Accurate prediction of chip movement is useful for designing chip breakers and guards for safety while machining.

Initially, the friction coefficient (μ) between tool and workpiece is taken as 0.17. This value is used by Madaj et al. [22] for the orthogonal simulation of machining of Al2024 using the SPH method. However, the axial and radial forces obtained from the simulation are small compared to the experimental observations, as shown in Table 6.6. Then, a simulation with the friction coefficient of 0.5 is run. This

Table 6.6: Comparison of simulated cutting force with different friction coefficients vs experimental values.

	Exp. (N)	Sim. (N) ($\mu = 0.17$)	Sim. (N) ($\mu = 0.50$)
Axial Force (F_X)	100	45	106
Radial Force (F_y)	65	10	60
Cutting Force (F_z)	235	210	180
Total Force (F)	264	215	219

value is close to the calculated friction coefficient value of 0.57, calculated using Merchant's circle diagram (the most commonly used method for analyzing the forces for orthogonal machining). The forces obtained from this simulation matched well with the experimental observations. This underlines the importance of friction in modeling machining.

6.6 Conclusion

This work presents a full-scale 3D turning simulation using smoothed particle hydrodynamics (SPH) method. The advantages of the SPH method over the Finite Element Method are demonstrated by modeling the material separation and high deformations observed during machining. The following conclusions can be made:

1. The cutting forces and chip morphology predicted by the simulation correlates with the experimental observations. The "long" continuous chips observed during the turning of Al 6061 are simulated. This simulation is challenging while using the Finite Element Method because of high mesh distortions.

2. A 2D plane strain machining model for the actual turning operation of a cylindrical workpiece under-predicts the cutting force and the thrust force. Moreover, the axial force cannot be predicted by the 2D model.

3. Value of the friction coefficient between the tool and the workpiece has a signif-

icant influence on the simulated forces, especially on the axial and radial force components. The correct prediction of the radial force is important as this component governs the stability of the machining conditions.

4. SPH method is computationally expensive. Using a coupled SPH-FE model, a significant reduction in the computation time can be achieved.

CHAPTER 7: MTP MACHINING MODEL

During turning operation, the continuous engagement of the cutting tool with the workpiece results in long, continuous chips. These chips can affect the surface finish of the workpiece, cause tool damage and even cause an injury to the operator. Modulated tool path machining is an effective solution for this. The chips are broken into smaller pieces by modulating the motion of the tool. A comparison of the chips formed by the conventional turning and MTP turning is shown in Fig. 7.1. Experimental studies of MTP machining have been done in turning [68–70] and threading [71]. Copenhaver et al. [72] conducted MTP turning of tube turning and compared the experimental cutting forces with analytical model results. In this chapter, the SPH method is used to simulate the conventional and MTP turning. Chips and cutting forces predicted by these simulations are compared. Also, the results are validated using the results of the analytical model. These results demonstrate the advantages of MTP turning.

(a) By conventional turning. (b) By MTP turning.

Figure 7.1: Comparison of chips formed by conventional and MTP turning [12].

7.1 Modulated Tool Path (MTP) machining

In Modulated tool path (MTP) machining, an oscillatory motion is superimposed upon the constant feed motion provided to the tool. This motion causes the tool to come out of contact with the workpiece and hence breaking the chip. Chip breakage depends upon two parameters: oscillation amplitude relative to the global feed per revolution, RAF and tool oscillation frequency relative to the spindle speed, OPR. Mathematically, these parameters are defined as

$$RAF = \frac{A}{f_r} \tag{7.1}$$

and

$$OPR = \frac{60 \times f}{\omega}. \tag{7.2}$$

Here, A and f are respectively the amplitude and frequency (in Hz) of oscillation of the tool, f_r is the global feed per revolution given to the tool and ω is the spindle speed (in rpm). An example of displacement of the tool in MTP machining is shown in Fig. 7.2. In this case, $RAF = 0.8$ and $OPR = 0.5$. Thus, in one cycle of the oscillation of the tool, the workpiece completes two revolutions. The black dashed line shows the displacement of the tool for the conventional turning.

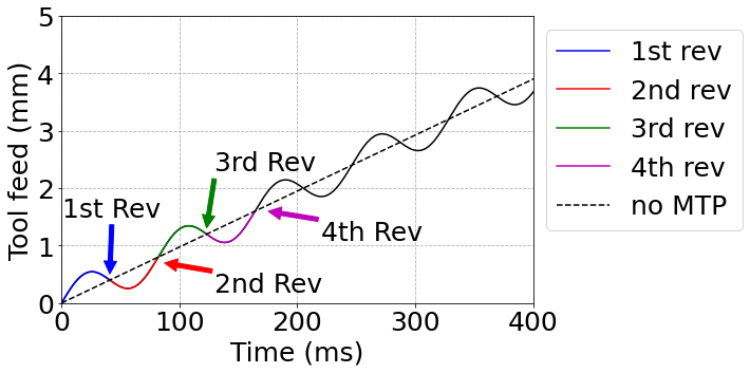

Figure 7.2: Tool displacement in MTP machining.

7.2 Chip breaking mechanism in MTP

In MTP turning, chips break due to the oscillatory motion provided to the tool. The thickness of the chip formed in each revolution is shown in Fig. 7.3. This figure is obtained from Fig. 7.2 by fitting the tool displacement curves for each revolution in one time period of the revolution of the workpiece. In the first revolution, the area shaded by blue in Fig. 7.3a is machined in the form of the first chip. This chip continues in the second revolution till point A in Fig 7.3b. No machining occurs when the tool moves from point A to point B in the second revolution (red line), as that portion of the workpiece is already machined. The second chip starts from point B onwards and continues to grow in the third revolution, as shown by green shaded in Fig. 7.3c. The second chip breaks in the fourth revolution of the workpiece at point C (shown in Fig. 7.3d). In this way, small chips are obtained during MTP turning.

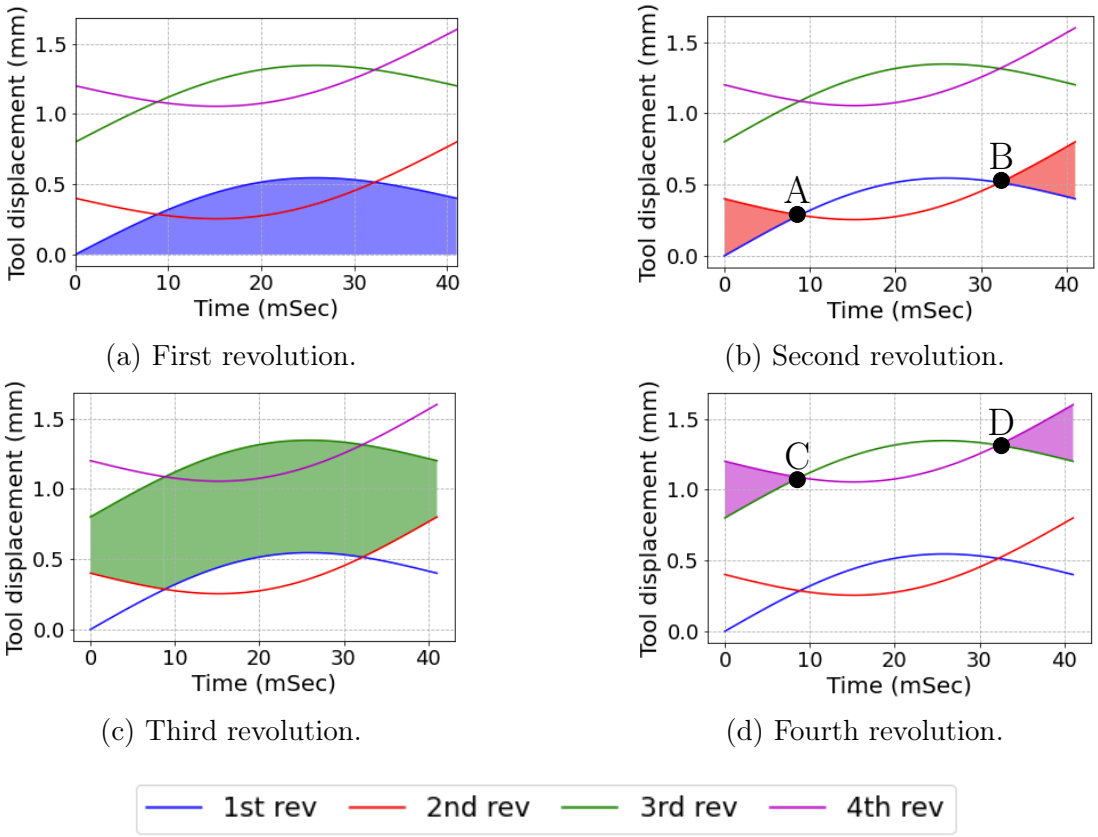

(a) First revolution.

(b) Second revolution.

(c) Third revolution.

(d) Fourth revolution.

Figure 7.3: Chip formation during MTP machining.

7.3 Computational model

The computational model is shown in Fig. 7.4. Similar to the 3D machining model, the tool is meshed by a Finite Element (FE) mesh and the workpiece is discretized using a coupled SPH-FE mesh. SPH particles are used in the zone of cutting, where the workpiece interacts with the tool. The FE mesh is used away from this zone, where the deformations are less. The SPH and FE mesh are coupled at the interface for the smooth transfer of physical properties. The geometry of the tool and the workpiece are shown in Fig. 7.5 and Fig. 7.6 respectively. All length dimensions are in mm. The machining conditions are provided in Table 7.1.

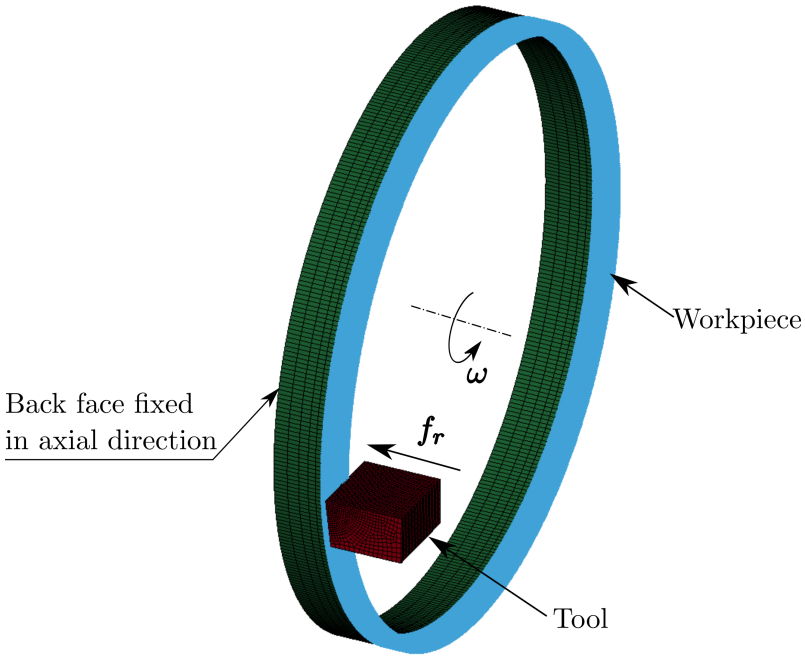

Figure 7.4: Computational model of MTP machining.

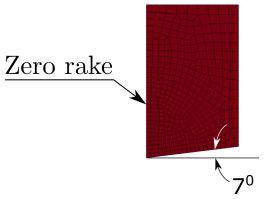

Figure 7.5: Geometry of the tool used.

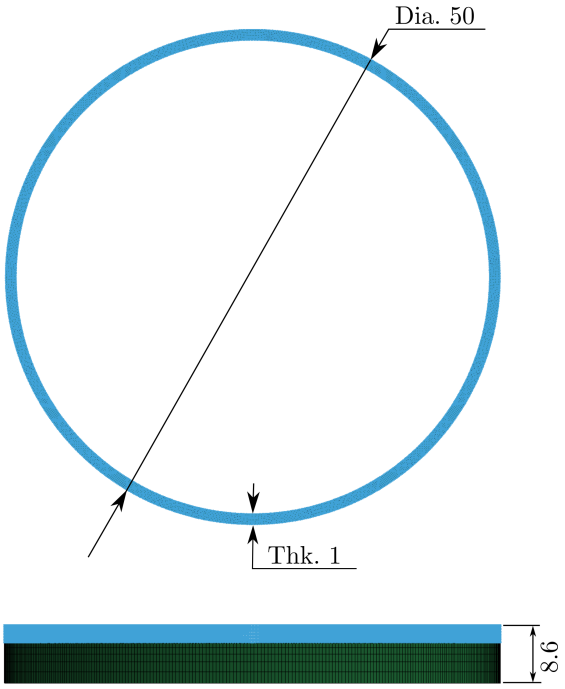

Figure 7.6: Geometry of the workpiece.

Table 7.1: Machining conditions used for the MTP simulation.

Parameter	**Value**
Material of tool	Tungsten carbide
Material of workpiece	1026 steel
Cutting speed	225 m/min
Global feed rate, f_r	0.4 mm/rev
RAF	0.8
OPR	0.5

7.4 Material properties

The material of the tool is tungsten carbide and that of the workpiece is AISI 1026 steel. The physical properties of the tool and the workpiece are shown in Table 7.2. Similar to the earlier machining models, the tool is modeled as a rigid body. For modeling the workpiece and its fracture in the form of chips, the Johnson-Cook material model with the Johnson-Cook damage model are used. The parameters of the material model of the workpiece are shown in Table 7.3.

Table 7.2: Physical properties of Workpiece and Tool [5, 6].

Property	Workpiece	Tool
Density, ρ (Kg/m^3)	7858	11900
Young's Modulus, E (GPa)	205	534
Poisson's ratio, μ	0.29	0.22
Specific heat, C_p (J/Kg K^{-1})	486	-
T_{melt}, (K)	1773	-
T_{room}, (K)	300	300

Table 7.3: Johnson-Cook parameters of workpiece (AISI 1026 steel) [7–9].

Parameter	A (MPa)	B(MPa)	n	C	m
Value	286.1	500.1	0.2282	0.022	0.917
Parameter	D1	D2	D3	D4	D5
Value	0.403	1.107	-1.899	0.00961	0.3

7.5 Boundary conditions

All nodes of the tool are fully constrained in Y and Z directions. A feed motion with the MTP parameters shown in Table 7.1 is given to the tool in X direction. All nodes of the back face of the workpiece are constrained for translation in the axial direction and a rotary motion about the axis of the workpiece is provided to them. The boundary conditions are shown in Fig. 7.7.

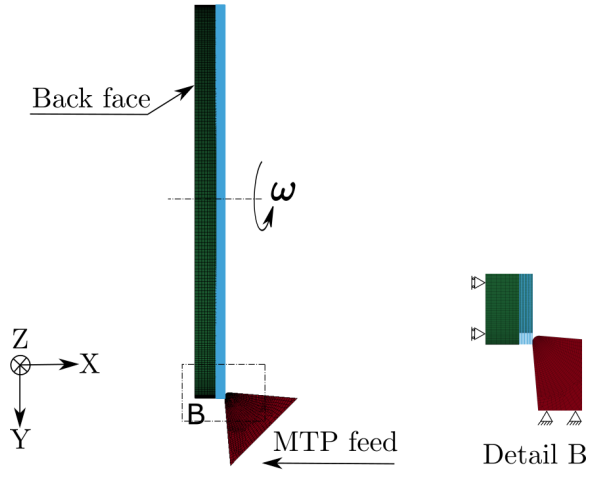

Figure 7.7: Boundary conditions used in MTP machining model.

7.6 Results

The results consist of the chip profiles and the cutting forces for the conventional turning and MTP turning. The simulated chip formation during MTP turning is shown in Fig. 7.8. The chip formation initiates as the tool comes into the contact with workpiece. Chip develops as the tool moves towards the workpiece. During the second revolution of the workpiece, the tool moves away from the workpiece due to the modulated feed motion given to the tool. The first chip separates when the tool is not in contact with the workpiece. Thereafter, the tool moves towards the workpiece and the second chip forms, develops and separates. The simulations predict long, continuous chips formed by the conventional turning and small, broken chips for the MTP turning. The comparison of chips is shown in Fig. 7.9.

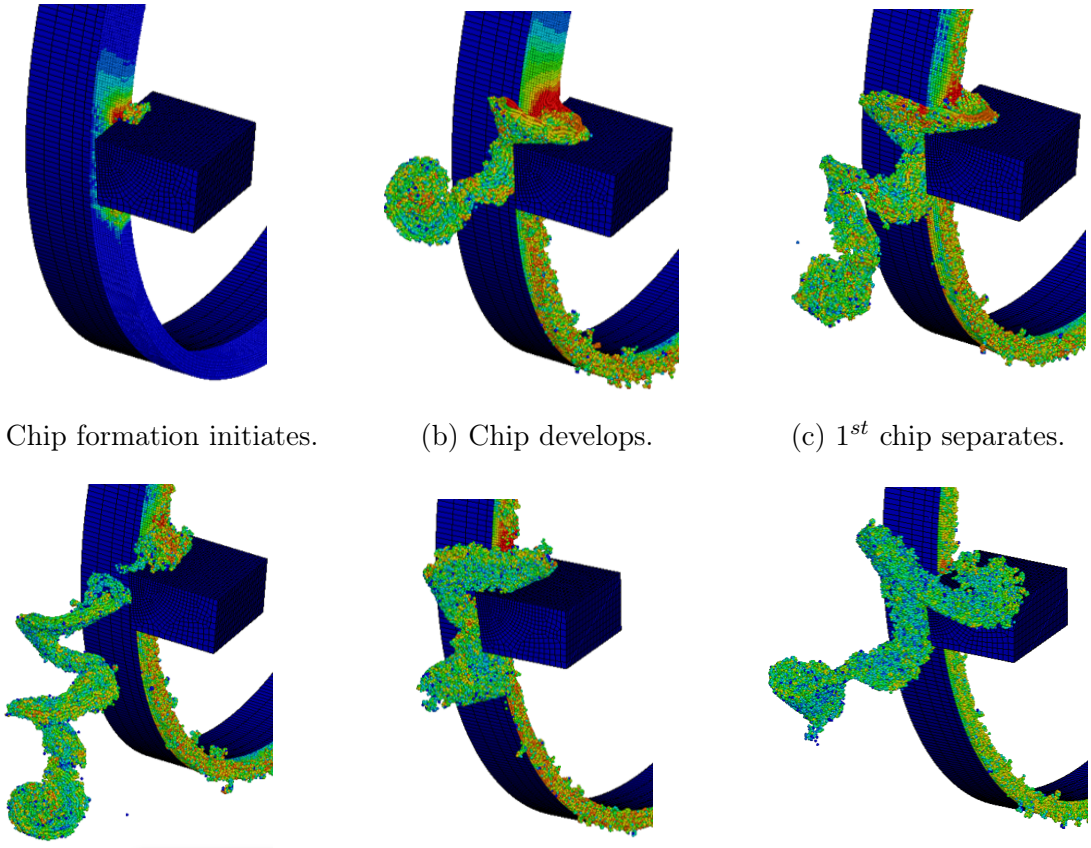

(a) Chip formation initiates. (b) Chip develops. (c) 1^{st} chip separates.

(d) 2^{nd} chip initiates. (e) 2^{nd} chip develops. (f) 2^{nd} chip separates.

Figure 7.8: Chip formation during MTP machining.

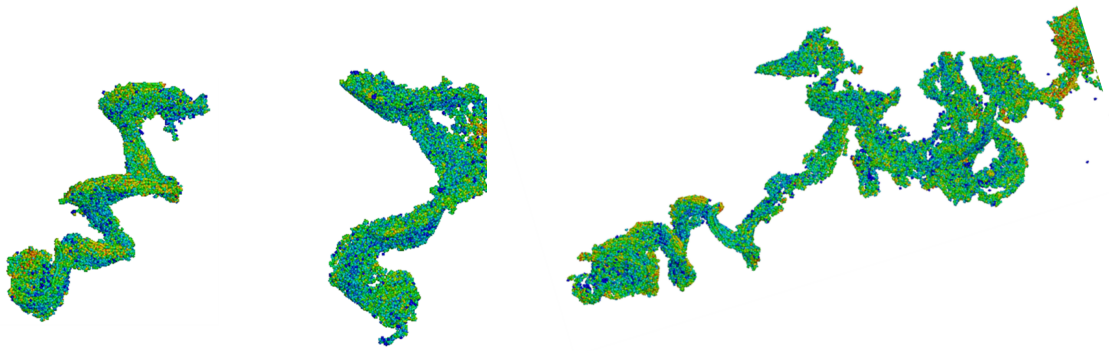

(a) MTP chips. (b) Conventional turning chips.

Figure 7.9: Chips formed by the MTP turning vs conventional turning simulation.

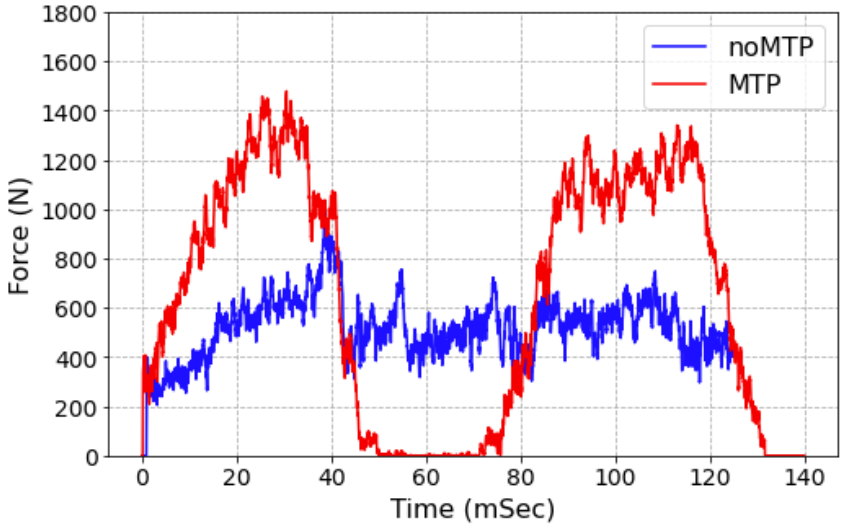

Figure 7.10: Cutting forces for MTP vs conventional turning simulation.

The cutting forces predicted by the simulations for the conventional and MTP turning are compared, shown in Fig. 7.10. For the conventional turning, a constant cutting force is observed. The cutting force for MTP turning shows a variation in the cutting force. Variation of the uncut chip thickness occurring during the MTP machining is the reason for this.

The cutting force predicted by the MTP turning simulation is compared with a mechanistic force model, described in detail in [72, 73]. In this model, the cutting force (F) is directly proportional to the chip area, A. Specific force (K_s) is the

proportionality constant. The specific force depends on the variables involved in the machining operations, such as the material of the workpiece, tool geometry, etc. Mathematically, the cutting force is given by,

$$F = K_s A = K_s b h(t). \tag{7.3}$$

Here, b is the chip width, and $h(t)$ is the instantaneous chip thickness. For MTP machining, this instantaneous chip thickness is calculated by subtracting the current motion of the tool from the workpiece surface formed by the previous revolution. For the machining conditions used in the MTP turning simulation, the instantaneous chip thickness is shown in Fig 7.11.

The data of Copenhaver et al. [72] is used for obtaining the plot of cutting force from the analytical model. The plot of the cutting force is obtained using the value of the specific force used in the paper. This plot is then compared with the force predicted by the simulation, as shown in Fig. 7.12. Good agreement between the simulated force and calculated force from the analytical model is observed. However, using the value of the specific force from the paper is an assumption. This is because of the difference in the value of feed used in the simulation and in experiments. Hence, more experimental data is required for a more accurate comparison.

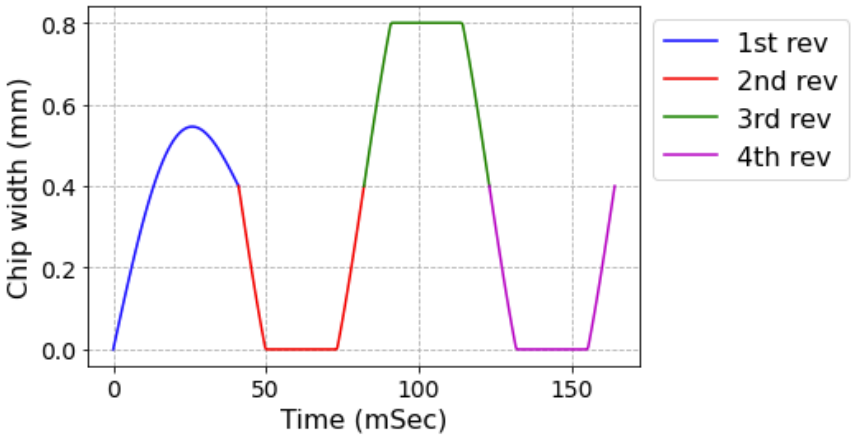

Figure 7.11: Instantaneous Chip thickness during MTP turning.

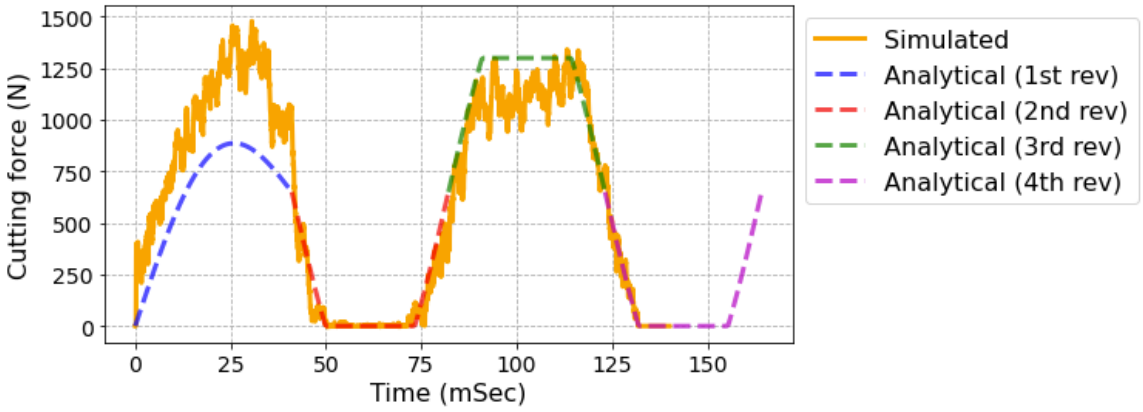

Figure 7.12: Comparison of simulated cutting force with the analytical model.

7.7 Proposed MTP with the modification in tool path

Based on the analysis of the uncut chip thickness during MTP turning, a modification in the tool path is proposed. In conventional MTP, the tool motion comprises a constant feed motion superimposed by a purely oscillatory motion. A change in the tool feed for alternate revolutions of the workpiece is proposed. Longer tool life due to less thermal and structural load on the tool is the expected for the proposed MTP.

A comparative analysis of the modified MTP with the conventional MTP is shown in Fig. 7.13. The feed motions of the tool for the conventional MTP and proposed MTP are shown in Fig. 7.13a. For the proposed MTP, the motion of the tool remains the same as in the conventional MTP for the first revolution of the workpiece (until point A). The tool remains stationary until point B and then follows a linear path with time till the end of the second revolution (point C). This motion is repeated for the subsequent revolutions.

The tool feed motion is shown revolution-wise for the first four revolutions in Fig. 7.13b. This plot is used to calculate the uncut chip thickness during machining (shown in Fig. 7.13c). The cutting force is directly proportional to the uncut chip thickness during machining. Hence, this plot is a representation of the cutting force. For the proposed MTP, the tool experiences a high level of the cutting force for $\sim$ 50% of

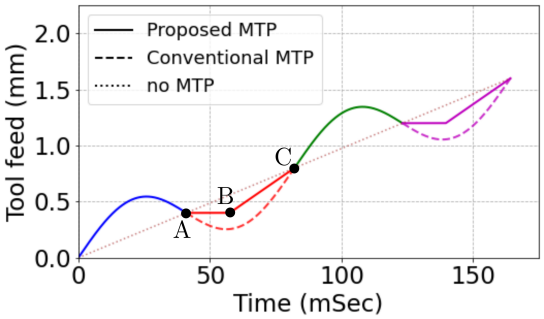

(a) Proposed vs Conventional MTP.

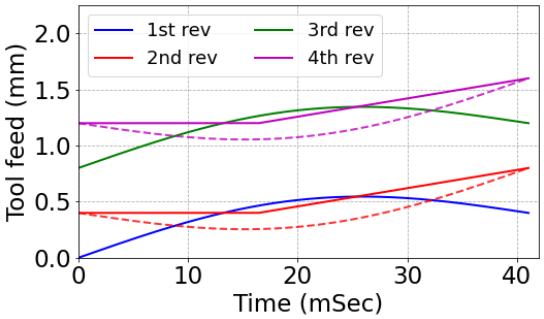

(b) Revolution-wise comparison.

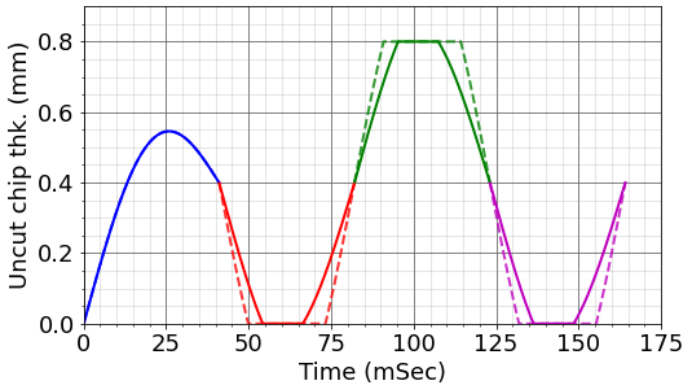

(c) Change in Chip thickness and hence Cutting force.

Figure 7.13: Comparison of tool feed in proposed MTP with the conventional MTP.

time in comparison with the conventional MTP. This also results in a less steep force plot. The structural and thermal loads on the tool are dependant on the cutting force. Thus, due to smaller loads, longer tool life is expected for the proposed MTP. The experimental work is in progress to validate this proposal.

7.8 Conclusion

This work incorporates the modulated tool path (MTP) in a full-scale 3D turning simulation using Smoothed particle hydrodynamics (SPH) method. The results of the MTP model simulation are compared with that of the conventional turning. Also, the cutting force predicted by the simulation is validated with the analytical model.

1. Broken chips are formed by MTP turning are simulated by the machining model. In contrast, the simulation of the conventional turning with the same machining

conditions predicts long continuous chips. These results are in line with the experimental observations.

2. The cutting force predicted by the MTP machining model fluctuates with time, whereas it is continuous for the conventional turning.

3. The cutting force predicted by the MTP machining model is validated with the analytical model. However, the value of the specific force is taken from Copenhaver et al. [72]. The value of feed/rev in the paper is different from that used in the simulation. Therefore, machining experiments need to be conducted for more accurate validation.

4. A modified MTP machining is proposed with changes in the tool feed motion. The advantage of this proposed MTP machining is presented analytically based on the uncut chip thickness plot. Experimental work for validation is in progress.

CHAPTER 8: MACHINING MODEL WITH DYNAMICS

Increasing the material removal rate while achieving precise dimensional accuracy is the requirement of the current machining industry. The machining conditions should be selected carefully for stable machining to achieve this goal. The selection of tools, tool holders, and width of cut are some important parameters affecting machining stability. During turning operation, avoiding the occurrence of regenerative chatter is essential. This phenomena is shown in Fig. 8.1. Due to the initial impact of the tool on the workpiece, the tool starts vibrating. This vibration of the tool during cutting creates a wavy surface on the workpiece. As the tool feeds into the workpiece for the next revolution, the uncut chip thickness varies due to the wavy surface imprinted in the previous revolution. This causes uneven cutting force, as the cutting force is directly proportional to the uncut chip thickness. Depending upon the machining conditions, this feedback may cause unstable machining or chatter.

In the machining models of the previous chapters, the vibration of the tool due to the action of cutting forces is neglected. In this chapter, the elastic behavior in the system is modeled by attaching spring and damper to the tool. The machining model and the results are presented in the following sections.

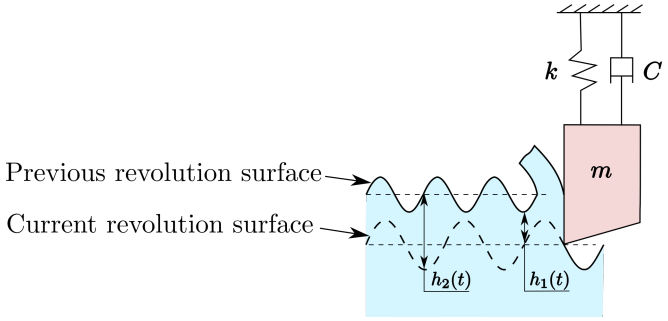

Figure 8.1: Regenerative chatter [$h_1(t)$ and $h_2(t)$ are instantaneous chip thickness].

8.1 Model description

The machining model, shown in Fig. 8.2, consists of a tool, a tubular workpiece, a spring and a damper. Similar to the three-dimensional machining model, the tool is discretized using finite element mesh and the workpiece is discretized using a coupled SPH-FE mesh. The spring and damper are used to model the dynamic behavior of the system. In this study, the dynamic elements are modeled with a single degree of freedom, i.e., along the axis of the workpiece. The machine dynamics in this direction contributes to the chatter during machining. The dynamic behavior in the other directions is ignored. One end of the spring and damper is attached to the center of gravity of the tool. The other end is attached to a fixed node. The geometry and mesh of the tool and the workpiece are shown in Fig. 8.3 and Fig. 8.4 respectively. All length dimensions are in mm. A zero rake tool has been used in the model. The reference values of the stiffness of the spring and damping coefficient are determined experimentally from the frequency response of the tool.

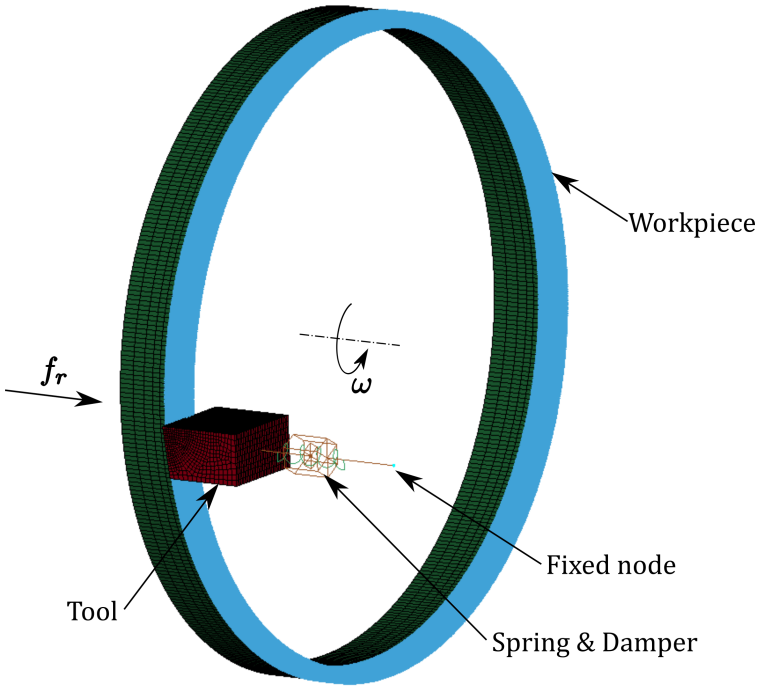

Figure 8.2: Machining model with machine dynamics.

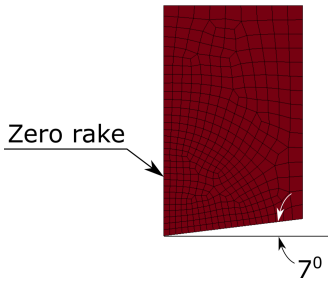

Figure 8.3: Geometry of the tool used in machine dynamics model.

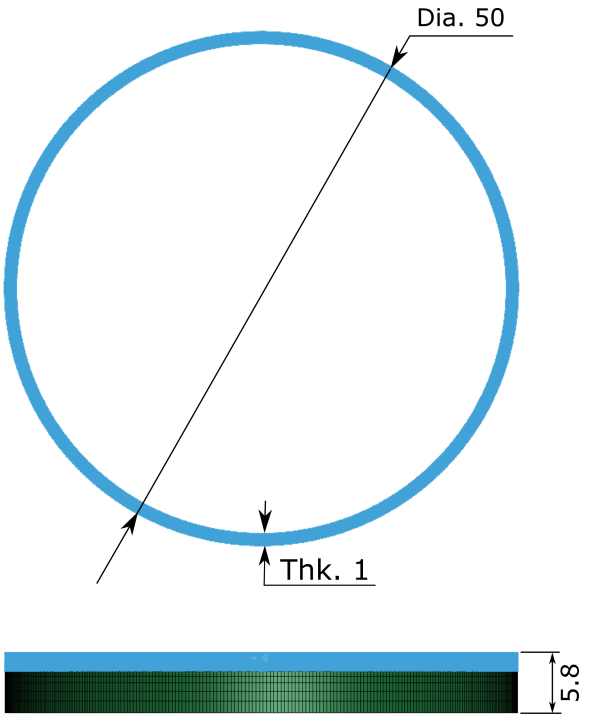

Figure 8.4: Geometry of the workpiece used in machine dynamics model.

8.2 Boundary conditions

The boundary conditions, shown in Fig. 8.5, are applied to the workpiece and free end of the spring and damper. All nodes on the back face of the workpiece are constrained to rotate along its centerline axis with the the rotational speed of the workpiece during machining. Also, the feed motion (translation) towards the tool in X direction is given to them. The free end of the spring and the workpiece is connected to a node. The node is fully constrained in all directions.

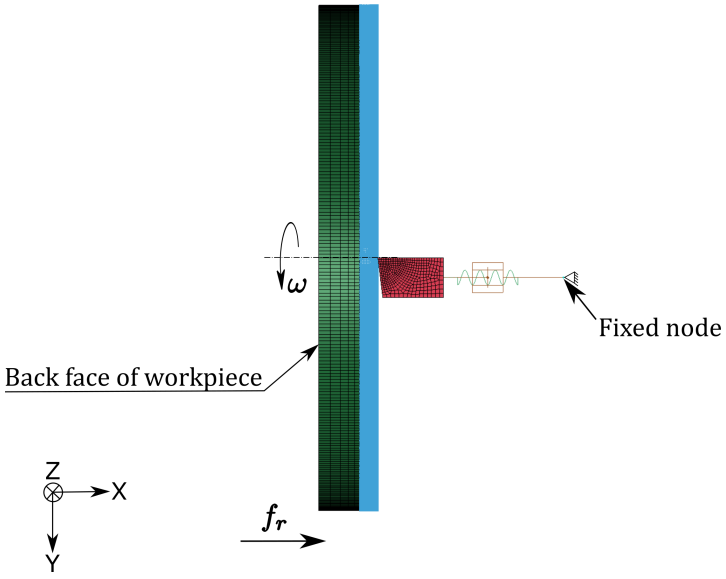

Figure 8.5: Boundary conditions used in machine dynamics model.

8.3 Material properties

The material properties are the same as the ones used in the three-dimensional machining model. The tool is made of tungsten carbide and the workpiece is Al 6061. The physical properties of the tool and the workpiece are shown in Table 6.1. The tool is modeled as a rigid body. The Johnson-Cook material model with the Johnson-Cook damage model are used to model the material behavior of the workpiece. The parameters of the material model of the workpiece are shown in Table 6.2.

8.4 Results

Eight simulations are run to understand the effect of different machine dynamics parameters on the tool vibration and the cutting forces. The parameters are shown in Table 8.1. Simulation 1 is with no tool flexibility. Simulation 2 is with the data provided by Copenhaver et al. [72]. The effect of spring only is studied in simulations 3 and 4. The effect of the damper is studied with simulations 5 and 6. All these six simulations are with a tube thickness of 1 mm. The machining stability depends on the width of cut. This is studied using the simulations 7 and 8. The results of both these simulations are compared with simulations 2 and 6, respectively.

Table 8.1: Parameter sets used for Machine dynamics study.

Simulation no.	**Spring stiffness (N/m)**	**Damping coefficient (N-s/m)**	**Tube thicknes (mm)**
1	No spring	No damper	1
2	5.9×10^7	2.16×10^3	1
3	2.36×10^6	No damper	1
4	4.72×10^6	No damper	1
5	2.36×10^6	2.16×10^3	1
6	2.36×10^6	1.08×10^3	1

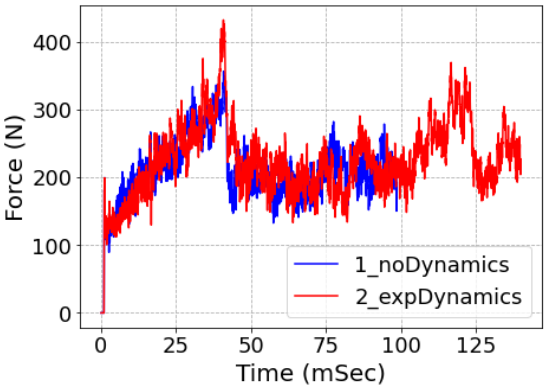

(a) Cutting force (F_c).

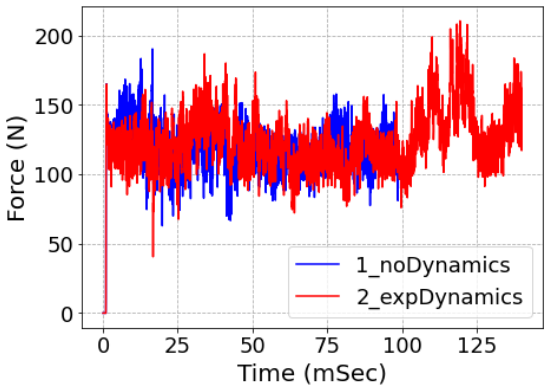

(b) Axial force (F_a).

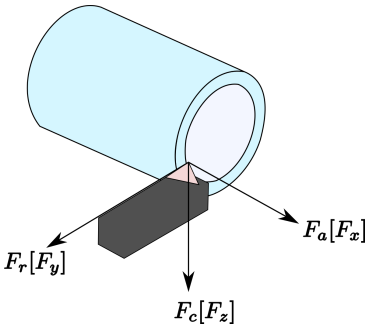

(c) Force directions

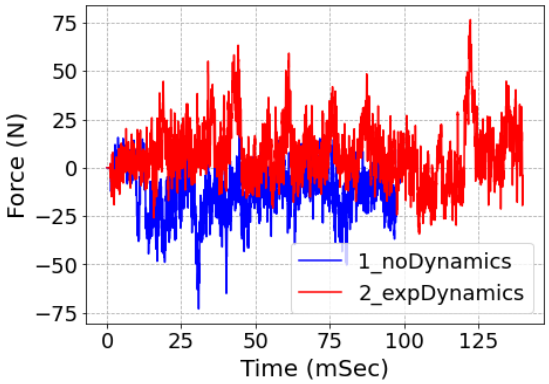

(d) Radial force (F_r).

Figure 8.6: Cutting forces for model with no dynamics and model with experimentally measured dynamics.

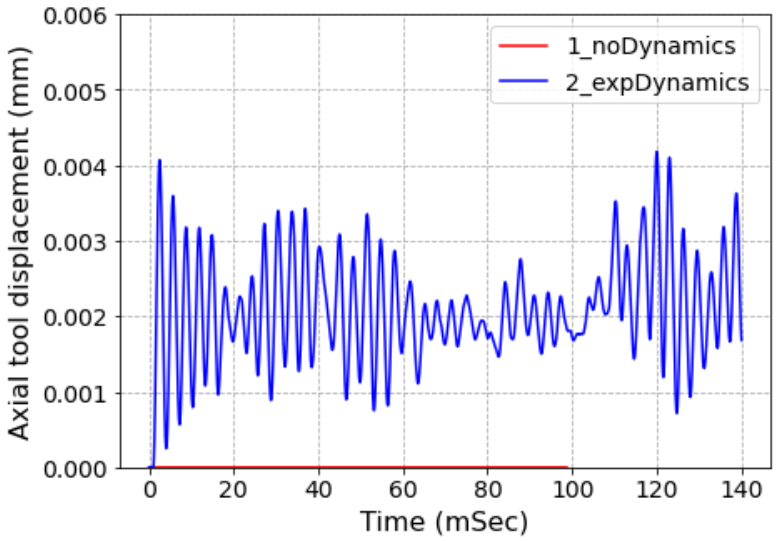

Figure 8.7: Tool vibration for model with no dynamics and model with experimentally measured dynamics.

8.4.1 Model with no dynamics and Model with experimentally measured dynamics

The results of simulations of the two models: one with no dynamic elements and the other with the dynamic elements having the experimentally measured values, are compared in this section. The plots of the cutting forces in the three directions are shown in Fig. 8.6. The forces overlap with each other. The value of radial force is close to zero as the turning of a thin wall tube can be approximated to be orthogonal machining. The reason for the overlapping cutting forces becomes clear from the plot of tool vibration plots in the axial direction of the workpiece, shown in Fig. 8.7. The spring and damper are connected to the tool in this direction. There is no vibration of the tool for the model with no dynamic elements. The vibrations are fluctuating and are of the order of microns for the model with dynamic elements. Due to the computational expensive SPH method, the models are simulated for three revolutions of the workpiece. Based on the result of tool vibration, the chatter may not develop in such a short time. Hence, to understand the effect of the variation of the dynamic elements, the stiffness of the spring is reduced by an order for further simulations.

8.4.2 Models with different spring stiffness and no damping

Simulation models 3 and 4 are with spring elements only, with the spring stiffness of $2.36 \times 10^6 N/m$ and $4.72 \times 10^6 N/m$, respectively. The tool vibrations in the axial direction are shown in Fig. 8.8. The tool vibration is more for simulation 3. This is an expected result as the spring is less stiff. Also, the vibration goes on increasing with time. This phenomenon is because of the lack of damping elements in the system. The tool starts vibrating due to the initial impact on the workpiece. This causes an uneven machined surface on the workpiece, which in turn leads to fluctuating cutting force (shown in Fig. 8.9). This fluctuation in the force adds to the tool vibration.

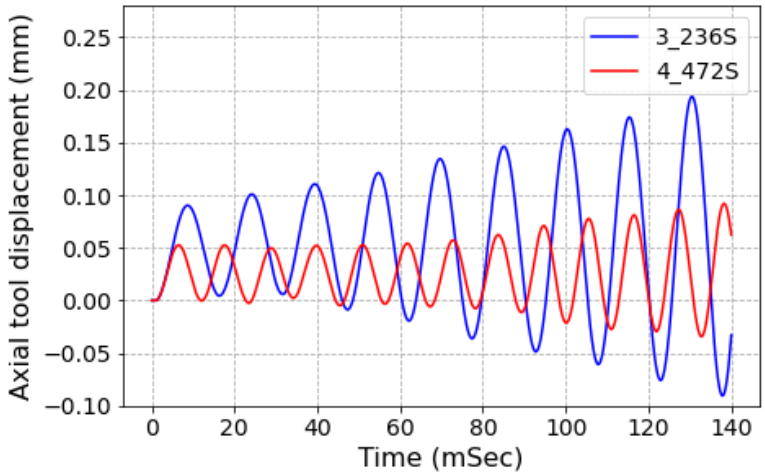

Figure 8.8: Comparison of tool vibration with change in spring stiffness.

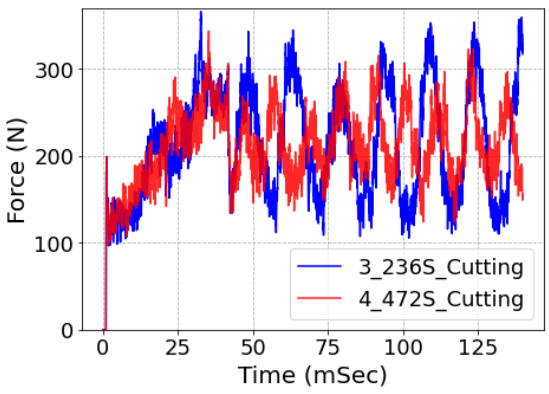

(a) Cutting force.

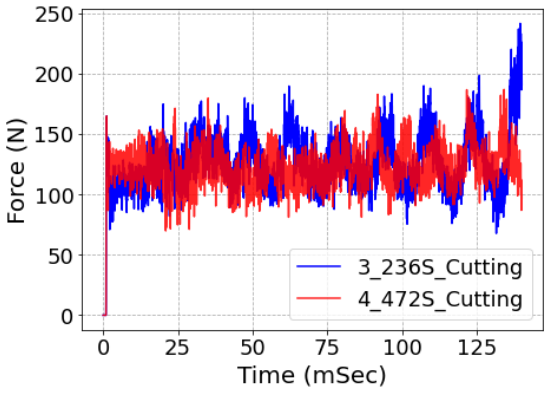

(b) Axial force.

Figure 8.9: Cutting forces comparison with change in spring stiffness.

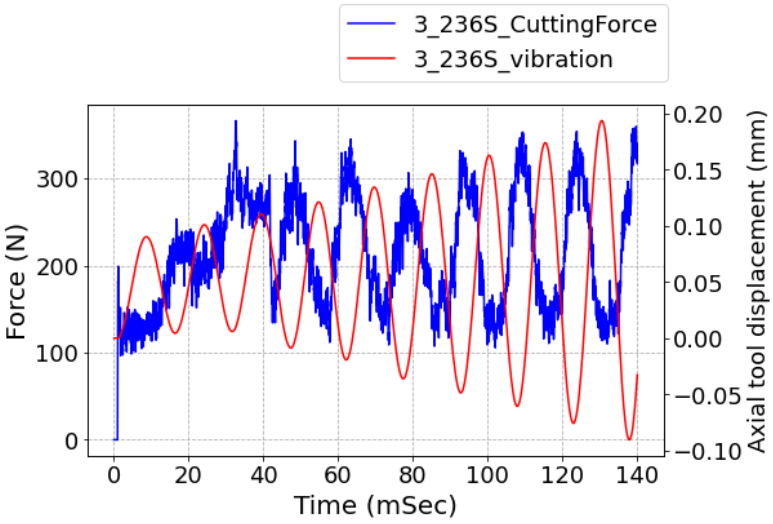

Figure 8.10: Phase difference between tool vibration and cutting force.

A phase difference is observed between the cutting force and the tool vibration. The plot of the cutting force and axial tool displacement (on the secondary axis) with time is shown in Fig. 8.10. After the first revolution, the phase difference is 90°. As the tool moves towards the workpiece, the axial displacement becomes more negative. The uncut chip thickness increases, leading to an increase in the cutting force. The cutting force is maximum when the tool is at maximum penetration position into the workpiece, i.e., at minimum displacement.

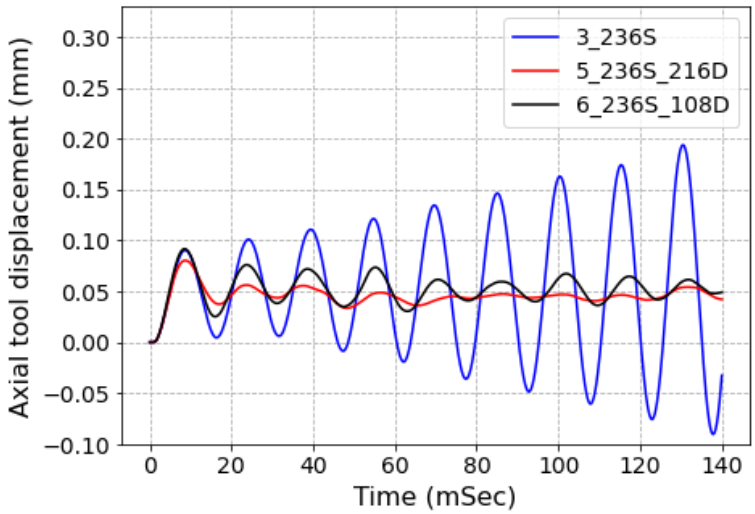

Figure 8.11: Comparison of tool vibration with change in damping coefficient.

8.4.3 Models with different damping coefficients

Simulation models 5 and 6 are with spring and damper elements. The spring stiffness are $2.36 \times 10^6 N/m$ for both the models. The damping coefficients are $2.18 \times 10^3 N/m$ and $2.18 \times 10^3 N/m$ respectively. The tool vibrations in the axial direction for simulations 3, 5 and 6 are shown in Fig. 8.11. The initial tool vibration is same for these models. Due to the damping present in simulations 5 and 6, the vibration decays with time. The decay is more for simulation 5, as the damping coefficient is greater in this model. Similar trend is seen in the plots of the cutting forces and axial forces (shown in Fig. 8.12).

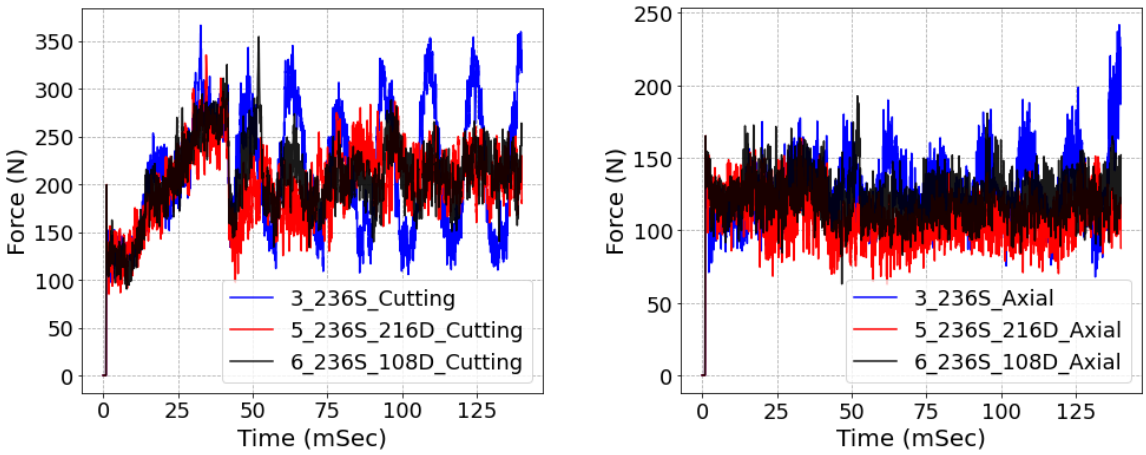

(a) Cutting force.

(b) Axial force.

Figure 8.12: Cutting forces comparison with change in damping coefficient.

8.5 Conclusion

Full-scale 3D turning simulation with machine dynamics using the smoothed particle hydrodynamics (SPH) method has been conducted in this study. The results of the simulations are useful in predicting the stability of machining. The following conclusions can be made:

1. The effects of spring stiffness and damping coefficient have been studied using the simulations. These dynamic elements result in the vibration of the tool,

which may lead to unstable machining or chatter.

2. A phase difference of 90° is observed between the cutting force and the tool vibration.

3. The SPH method is computationally expensive. For this reason, the simulations are run for three revolutions of the workpiece rotation. Small tool vibrations are observed for the model with actual values of the stiffness and damping coefficient measured during the experiments. These vibrations may develop at a later time. The stiffness of the spring is reduced by an order of magnitude to observe the effects of the dynamic elements, and further studies are conducted with these values.

4. The results of the simulation need to be validated using experiments.

CHAPTER 9: UNIQUENESS OF JOHNSON-COOK PARAMETERS

All the machining simulations described in the earlier chapters use the Johnson-Cook constitutive model [74] for modeling the material behavior of the workpiece during machining. The Johnson-Cook model has also been used by various researchers in analytical models such as the Oxley machining model [13] and finite element simulations [17, 19, 20, 75, 76]. This model has five material-dependent parameters that relate flow stress of the material to strain, strain rate and temperature of the material. Experimentally, these parameters are obtained by fitting the data of the quasi-static tests at various temperatures and dynamic tests at different strain rates. Tensile tests and Split-Hopkinson Pressure Bar (SHPB) tests are two of the techniques typically used for this purpose [77]. However, the extreme conditions of machining [32], such as strain rates of the order 10^5/s to 10^6/s and high temperatures, are challenging to achieve in these experiments. Various researchers have proposed inverse approaches to determine these parameters using the data from the actual machining experiments to overcome this difficulty. However, these methods have been shown to have the drawback of producing non-unique solutions to the Johnson-Cook parameter values.

The inputs to the inverse method are machining conditions, experimental observations and simulation results (finite element analyses or analytical models). The simulation results depend on the material model parameters. The goal is to determine these material model parameters by minimizing the objective function, which consists of the difference between experimental observations and simulation results. This minimization is achieved by tuning the parameters of the material model using an optimization algorithm such as AMPGO, PSO, and Kalman filter. The determined material model parameter set is used in the computational or analytical models and

validated with experimental results. Although experiments such as uniaxial, isothermal compression testing of cylindrical specimens [78], laser peening [79], and cold wire drawing [80] have been used for validation purposes, the most widely used experimental technique is based on orthogonal machining.

In this work, the source of non-unique solutions to the inverse problem is identified and an approach to determine a unique set of Johnson-Cook parameters is presented. The extended Oxley's model is used as the analytical model for simulation. Two separate optimization algorithms, Adaptive Memory Programming for Global Optimization (AMPGO) and Particle Swarm Optimization (PSO), are used to minimize the objective function. The consideration of two separate algorithms eliminates any bias that may be present in one particular method.

9.1 Literature review

During machining, the workpiece material undergoes plastic deformation. The plastic behavior of the material is modeled using the Johnson-Cook material model:

$$\sigma_{eq} = \underbrace{\left(A + B\varepsilon_p^n\right)}_{\text{Strain hardening}} \times \underbrace{\left[1 + C\ \ln\left(\frac{\dot{\varepsilon_p}}{\dot{\varepsilon}_0}\right)\right]}_{\text{Strain rate sensitivity}} \times \underbrace{\left[1 - \left(\frac{T - T_0}{T_m - T_0}\right)^m\right]}_{\text{Thermal softening}}. \tag{9.1}$$

Here, σ_{eq} is flow stress, ε_p is the equivalent plastic strain, $\dot{\varepsilon}_p$ is the plastic strain-rate, $\dot{\varepsilon}_0$ is a reference strain-rate, T_m is the melting temperature, and T_0 is a reference temperature. A, B, C, n and m are the material dependant parameters. A denotes the initial yield strength, B and n describes the strain hardening, C captures the strain rate sensitivity and m the thermal sensitivity of the material.

The majority of the existing studies on the inverse approach for determining the Johnson-Cook parameters can be divided into three categories. In the first category, all five parameters of the Johnson-Cook model are taken as optimizing parameters and through optimization algorithms, determination of unique parameter set is claimed.

Agmell et al.[81] and Ning et al. [82] performed inverse analysis using a Kalman filter and machining experiments. The relationship between the Johnson-Cook parameters and machining output parameters was developed through multiple FEM simulations. Five discrete values within a range of ± 30 % of each Johnson-Cook parameter of reference material were used for these simulations. A close agreement between the simulated FEM results and experimental observations was observed using the parameter set obtained through the inverse approach. Ozel et al. [83] used different variations of the PSO method, namely, PSO, PSO-c and CPSO method, to determine the Johnson-Cook parameters. A unique set of parameters were obtained for each method, but the values differ for each method. The parameter set obtained using CPSO showed the best correlation with the experimental results. Eisseler et al. [84] used design of experiment (DoE) for inverse parameter identification by comparing the cutting force of FEM simulations with 50 Johnson-Cook parameter sets and machining experiments. Two sets of all the five Johnson-Cook parameters were determined for steel SAE-4142 within a maximum difference of less than 3%.

The second category recognizes the non-uniqueness of the parameters obtained by the inverse approach and proposes some suggestions to counter this non-uniqueness. Denkena et al. [85] used Oxley's machining model and Particle Swarm Optimization (PSO) method using the cutting and thrust forces in an orthogonal slot milling experiment to tune the Johnson-Cook parameters. The optimization was performed without using tensile test data (i.e., all five parameters varied) and with the use of tensile test data (i.e., A, B and n values were obtained from tensile test data and C and n optimized using PSO method). Wide variation was observed in the resulting set of parameters obtained by the two methods. Local minima in the solution domain were suggested to be the reason for this observation. Karkalos and Markopoulos [86] used the Fireworks optimization algorithm for the determination of all the five parameters of Johnson-Cook constitutive material model parameters. Their sugges-

tion was to choose the bounds for optimization variables carefully to avoid premature convergence to a solution far from the optimal point. Pujana et al. [87] varied four parameters (B, n, C and m) of the Johnson-Cook model for the inverse analysis using deterministic minimization techniques. The selection of initial values was found to influence the optimized set of parameters. The use of regularly distributed function evaluations was proposed in order to reach the absolute minimum.

The third category focuses on the non-uniqueness study and attempts to eliminate this by adding experimental results to determine the unique parameter set. Shrot et al. [88] studied the non-unique identification of Johnson-Cook parameters by matching the results of machining experiments and finite element models. The parameters A, B and n were varied in a defined interval. The parameter sets were selected based on the closeness of effective stress-strain plots using the standard Johnson-Cook parameters and test parameters. Similar chip shapes and cutting forces were obtained by the FEM simulation using these identified parameter sets. However, the non-uniqueness was attributed to the measurement error during experiments. The use of different cutting conditions was suggested to obtain a unique parameter set.

Storchak et al. [89] determined the Johnson-Cook parameters using a combination of compression test and machining experiments. The parameters A, B, n and m were obtained using the compression tests at various strain rates and temperatures. Only the parameter C was obtained using the Oxley theory and machining experiments.

These three different approaches coupled with multiple methods to determining unique values of Johnson-Cook parameters via inverse methods show that the origin of non-uniqueness of the parameters (when inverse methods are used) is far from settled. In this Chapter, we hope to address this issue by considering two optimization algorithms.

9.2 Methodology

For the inverse approach using orthogonal machining, the observations of machining experiments along with the results of machining simulations or an analytical model (such as the extended Oxley model) are used to form an objective function. The Johnson-Cook parameters are tuned to minimize this objective function using the optimization algorithm. The cutting force (F_c), chip thickness ratio (h_c) and tool-workpiece interface temperature (T_c) are commonly taken as the variables of the objective function (Err), which is given by,

$$\text{Err} = \left[\left(\frac{F_{c,exp} - F_{c,sim}}{F_{c,exp}} \right)^2 + \left(\frac{h_{c,exp} - h_{c,sim}}{h_{c,exp}} \right)^2 + \left(\frac{T_{c,exp} - T_{c,sim}}{T_{c,exp}} \right)^2 \right]^{\frac{1}{2}}. \quad (9.2)$$

Here, the label "exp" represents experimental observation and "sim" represents simulated or calculated value. The output of the machining experiment is assumed to be the same as that obtained from the extended Oxley model using the known values of Johnson-Cook parameters in literature. This is done to eliminate the measurement uncertainty associated with experiments. Also, the accuracy of the determined Johnson-Cook parameters can be obtained by comparing with these reference values.

For investigating the uniqueness of Johnson-Cook parameters, two approaches (shown in Fig. 9.1) are taken. In the first approach, all the five Johnson-Cook parameters are considered as the unknown variables. In the second approach, the parameters C and m are considered as the unknown variables. The parameters A, B and n are considered as known. They are determined using the quasi-static tensile test and hence their values are kept the same as the value in the literature. For the unknown Johnson-Cook parameters, a wide range is provided as input to the optimization algorithm. This is based on their values for different materials in the literature [74] and [90]. The ranges considered for the parameters are shown in Table 9.1. The machining conditions used as input parameters are given in Table 9.2.

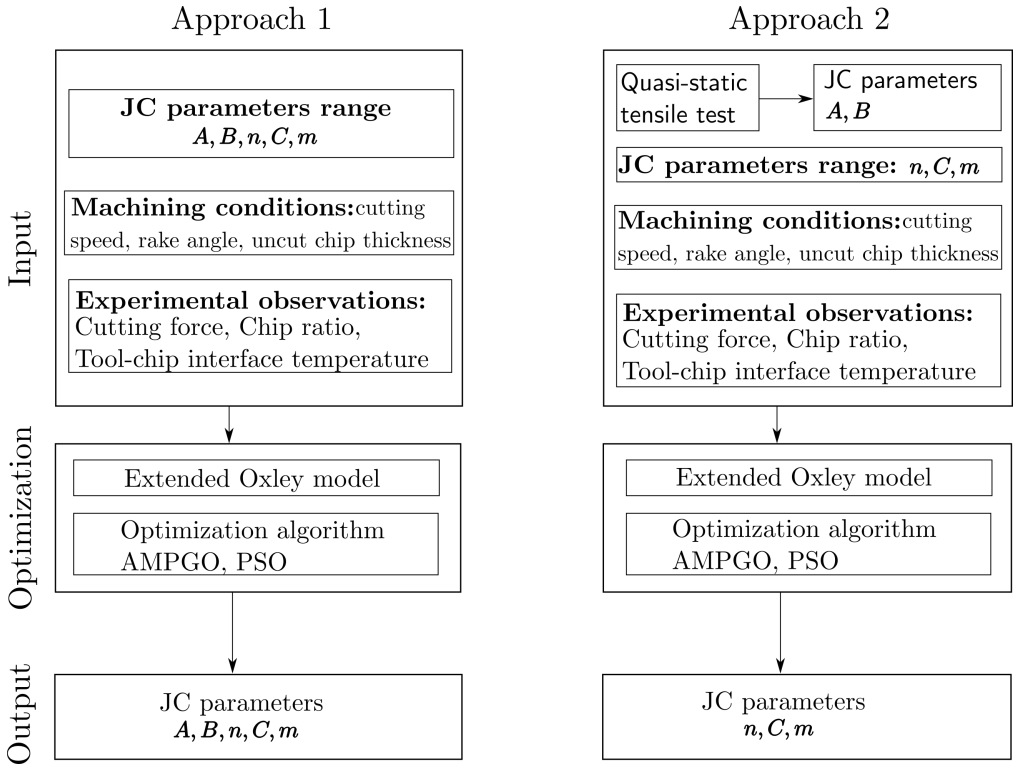

Figure 9.1: Approaches used for investigating the unique determination of Johnson-Cook parameters.

The Johnson-Cook parameters are obtained with these inputs by minimizing the objective function using the optimization algorithms, AMPGO, and PSO algorithms. In the optimization loop, the extended Oxley model is used to calculate the values of the machining output for a given set of Johnson-Cook parameters. The output of Approach 1 is all the five parameters, whereas the parameters C and m are the output of Approach 2. The uniqueness of the parameter sets is discussed in the results section.

Table 9.1: Johnson-Cook parameter range provided in the inverse method.

Parameter	Ref value [91]	Min value	Max value
A (MPa)	553.1	440	660
B (MPa)	600.8	480	720
n	0.234	0.18	0.28
C	0.0134	0.001	0.090
m	1	0.5	2

Table 9.2: Machining conditions used [10].

Test no.	V (m/min)	$t1$ (mm)	$\alpha(^\circ)$
1	200	0.15	-7
2	200	0.15	5
3	200	0.30	-7
4	200	0.30	5
5	400	0.15	-7
6	400	0.15	5
7	400	0.30	-7
8	400	0.30	5

9.2.1 Extended Oxley theory

The parallel-sided shear zone theory, proposed by Oxley [13] is a widely used analytical model for predicting the stresses, cutting forces and the average temperature in orthogonal machining. The deformation zone consists of two regions: a parallel-sided primary shear zone and a rectangular secondary shear zone at the tool-chip interface of constant thickness. Along with the application of the principle of minimum work, this theory analyses the equilibrium of the shear plane AB (shown in Fig. 9.2) and the tool-chip interface to determine the physical parameters of the machining process. This is done by tuning three parameters, namely shear angle ϕ, strain-rate constant at the shear zone C_0 and strain-rate constant at the tool-chip interface zone δ.

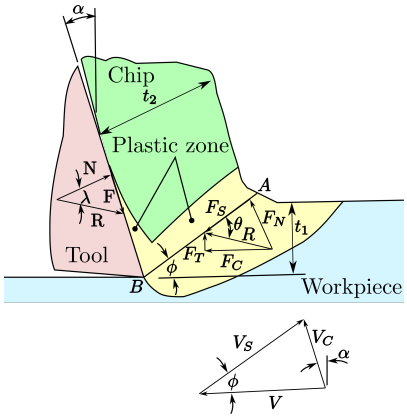

Figure 9.2: Chip formation model in Oxley's theory [13].

9.2.1.1 Shear Plane AB

Let t_1 be the uncut chip thickness, V the cutting velocity and α the rake angle of the tool. Then the length of the shear plane l_{AB}, the chip thickness t_2, the shear velocity V_S, and the chip velocity V_C are

$$l_{AB} = \frac{t_1}{\sin\phi}, \tag{9.3}$$

$$t_2 = \frac{t_1 \cos(\phi - \alpha)}{\sin\phi}, \tag{9.4}$$

$$V_S = \frac{V\cos\alpha}{\cos(\phi - \alpha)}, \tag{9.5}$$

and

$$V_C = \frac{V\sin\phi}{\cos(\phi - \alpha)}. \tag{9.6}$$

The equivalent shear strain at AB, ε_{AB} is

$$\varepsilon_{AB} = \frac{\gamma_{AB}}{\sqrt{3}} = \frac{\cos\alpha}{2\sqrt{3}\sin\phi\cos(\phi - \alpha)}. \tag{9.7}$$

and the equivalent shear strain rate along AB, $\dot{\varepsilon}_{AB}$ is

$$\dot{\varepsilon}_{AB} = \frac{\dot{\gamma}_{AB}}{\sqrt{3}} = \frac{C_0 V_S}{\sqrt{3} l_{AB}}. \tag{9.8}$$

The shear flow stress k_{AB} can be obtained from the tensile flow stress σ_{AB} by using the von Mises criterion and the Johnson-Cook material model as

$$k_{AB} = \frac{\sigma_{AB}}{\sqrt{3}} \tag{9.9}$$

with

$$\sigma_{AB} = (A + B\varepsilon_{AB}^n)\left[1 + C\ \ln\left(\frac{\dot{\varepsilon}_{AB}}{\dot{\varepsilon}_0}\right)\right]\left[1 - \left(\frac{T_{AB} - T_0}{T_m - T_0}\right)^m\right]. \tag{9.10}$$

The average temperature along AB, T_{AB} is calculated using

$$T_{AB} = T_0 + \eta \Delta T_{SZ}. \tag{9.11}$$

Here, T_0 is the initial temperature, η is the Taylor-Quinney coefficient and ΔT_{SZ} is the temperature rise in the primary shear zone. This temperature rise is obtained using the plastic work done in the shear zone and is given by,

$$\Delta T_{SZ} = \frac{(1-\beta) F_S V_S}{\rho V t_1 w C_p}. \tag{9.12}$$

Here, β is the fraction of heat conducted into the workpiece from the shear zone, which is estimated from the empirical equations

$$\begin{aligned} \beta &= 0.5 - 0.35 \log(R_T \tan\phi) \quad \text{for } 0.04 \leq R_T \tan\phi \leq 10 \\ &= 0.3 - 0.15 \log(R_T \tan\phi) \quad \text{for } R_T \tan\phi \geq 10. \end{aligned} \tag{9.13}$$

Here R_T is a non-dimensional number given in terms of the specific heat (C_p), cutting velocity (V), uncut chip thickness (t_1) and the thermal conductivity of the workpiece (K) by

$$R_T = \frac{\rho C_p V t_1}{K} \tag{9.14}$$

The angles in the chip formulation model (Fig. 9.2) are related by the expressions

$$\theta = \tan^{-1}\left(1 + 2\left(\frac{\pi}{4} - \phi\right) - C_0 n_{eq}\right), \tag{9.15}$$

and

$$\lambda = \theta - \phi + \alpha. \tag{9.16}$$

Here, the strain hardening exponent for the Johnson-Cool material model [10], n_{eq} is

expressed by the expression

$$n_{eq} \approx \frac{nB\varepsilon_{AB}^{n}}{A + B\varepsilon_{AB}^{n}}. \tag{9.17}$$

The normal stress at the tool-chip interface is given by

$$\sigma'_N = k_{AB}\left(1 + \frac{\pi}{2} - 2\alpha - 2C_0 n_{eq}\right). \tag{9.18}$$

9.2.1.2 Tool-chip interface

The strain (ε_{int}) and strain rate ($\dot{\varepsilon}_{int}$) at tool-chip interface using von Mises criterion is given by,

$$\varepsilon_{int} = \frac{\gamma_{int}}{\sqrt{3}} = 2\varepsilon_{AB} + \frac{h}{2\sqrt{3}\delta t_2}, \tag{9.19}$$

$$\dot{\varepsilon}_{int} = \frac{\dot{\gamma_{int}}}{\sqrt{3}} = \frac{V_C}{\sqrt{3}\delta t_2}. \tag{9.20}$$

The average temperature at the tool-chip interface, T_{int} is given by,

$$T_{int} = T_0 + \Delta T_{SZ} + \psi \Delta T_M. \tag{9.21}$$

Here, ΔT_M is the maximum temperature rise of the chip and is calculated using the empirical equation proposed by Boothroyd [92].

$$\log\left(\frac{\Delta T_M}{\Delta T_C}\right) = 0.06 - 0.195\delta\sqrt{\frac{R_T t_2}{t_1}} + 0.5\log\left(\frac{R_T t_2}{h}\right). \tag{9.22}$$

The tool-chip interface length, h and the average temperature rise in the chip ΔT_C are given by

$$h = \frac{t_1 \sin\theta}{\cos\lambda \sin\phi}\left(1 + \frac{C_0 n_{eq}}{3\left(1 + 2\left(\frac{\pi}{4} - \phi\right)C_0 n_{eq}\right)}\right) \tag{9.23}$$

and

$$\Delta T_C = \frac{FV_C}{\rho V t_1 w C_p}. \tag{9.24}$$

The flow stress at the tool-chip interface, k_{chip} is calculated using the expression

$$k_{chip} = \frac{1}{\sqrt{3}} \left(A + B\varepsilon_{int}^{n}\right) \left[1 + C \ \log\left(\frac{\dot{\varepsilon}_{int}}{\dot{\varepsilon}_0}\right)\right] \times \left[1 - \left(\frac{T_{int} - T_0}{T_m - T_0}\right)^m\right]. \tag{9.25}$$

9.2.1.3 Cutting forces

The cutting forces (shown in Fig. 9.2) are obtained using the equations

$$F = R\sin\lambda, \tag{9.26}$$

$$N = R\cos\lambda, \tag{9.27}$$

$$F_S = R\cos(\phi + \lambda - \alpha) = k_{AB} l_{AB} w, \tag{9.28}$$

$$N_S = R\sin(\phi + \lambda - \alpha), \tag{9.29}$$

$$F_c = R\cos(\lambda - \alpha), \tag{9.30}$$

$$F_t = R\sin(\lambda - \alpha). \tag{9.31}$$

The normal stress σ_n and the shear stress τ_{int} at the tool-chip interface are given by

$$\sigma_N = \frac{N}{hw} \tag{9.32}$$

and

$$\tau_{int} = \frac{F}{hw}. \tag{9.33}$$

9.2.2 Calculation flowchart

The flowchart for determining the Johnson-Cook parameters is shown in Fig. 9.3. There are two loops in the flowchart: the inner loop shown by the dashed line and the outer loop shown by the solid line. The calculation for the machining parameters $C_0, \phi,$ and δ for a given Johnson-Cook parameter set is done in the inner loop. The objective of the inner loop is to minimizing the gap between k_{chip} and τ_{int}, σ_N and σ'_N and the minimum cutting force F_C by tuning the parameters δ, C_0 and ϕ. The detailed

derivations and the equations used have been adopted from Lalwani et al. [10]. The difference in the calculation approach in the current work with respect to Lalwani et al. [10] is that instead of varying the values of the parameters (δ, C_0 and ϕ) by discrete values, the optimization is done using the AMPGO algorithm. This eliminates the dependence of the optimization accuracy on the discrete interval.

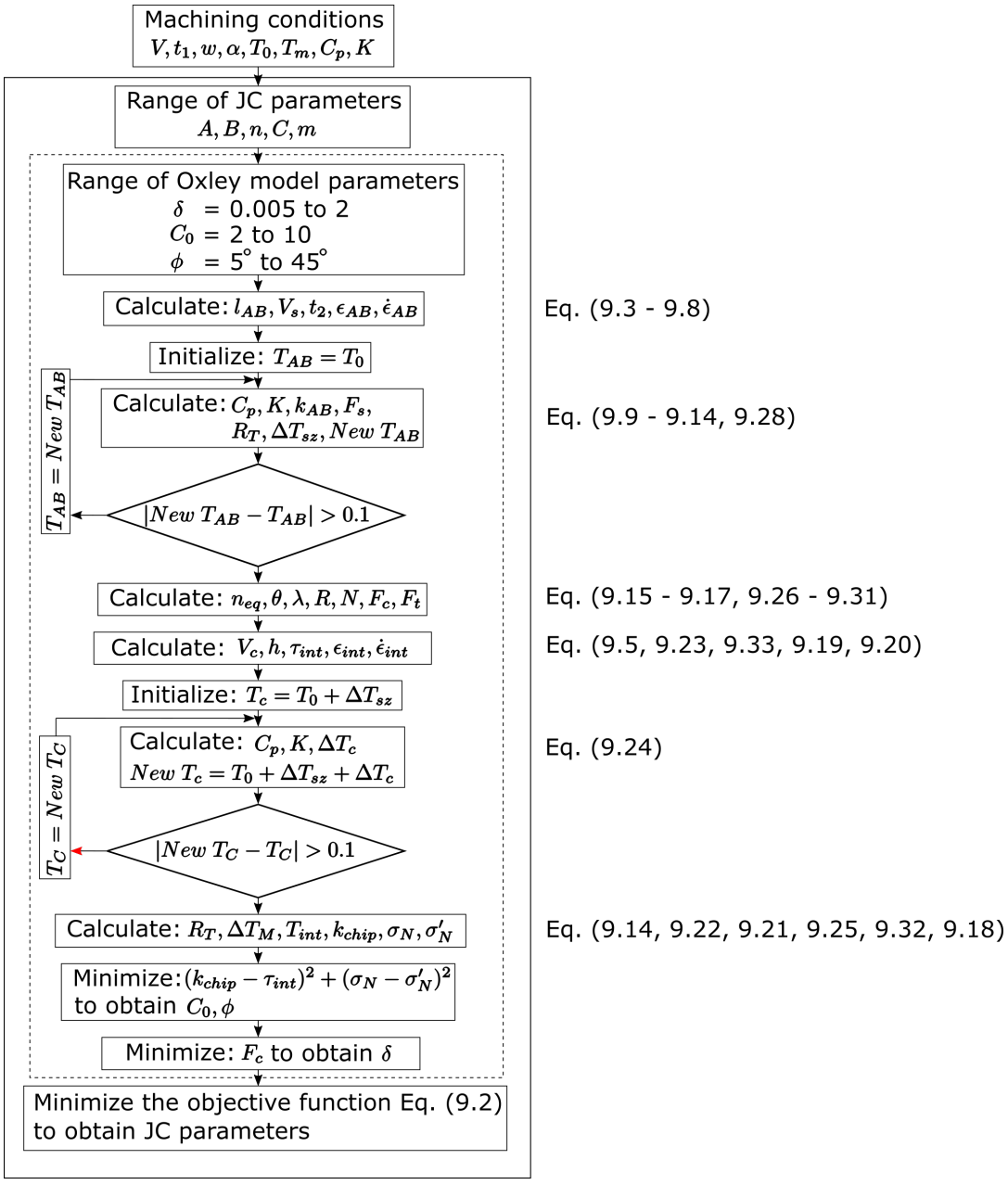

Figure 9.3: Determining JC parameters using AMPGO/PSO method.

The optimal Johnson-Cook parameter values are determined using the outer loop. A wide range of Johnson-Cook parameters is provided as input. The objective here is to minimize the objective function Eq. 9.2 by tuning the Johnson-Cook parameters. This is done using the AMPGO algorithm and PSO algorithm separately for each of the two approaches.

9.2.3 Adaptive Memory Programming for Global Optimization method

Adaptive Memory Programming for Global Optimization (AMPGO) is an optimization algorithm presented by Lasdon et al. [14] for the constrained global optimization problems. It consists of two phases: minimization and tunneling. A local minimum is found using a descent algorithm. Then, using a tunneling loop, the objective is to improve the found minimum with the new solution away from the current solution for the next minimization phase. The tunneling function is given by the Eq. 9.34.

$$TTf(\mathbf{x}) = \frac{(f(\mathbf{x}) - \text{aspiration})^2}{\prod_{\mathbf{s}_i \in \text{ Tabulist}} (\text{dist}(\mathbf{x}, \mathbf{s}_i))^2}. \tag{9.34}$$

Here, $f(\mathbf{x})$ is the function to be optimized. The aspiration value for the objective function is slightly less than the current best value. Tabulist contains the points from which to move away, i.e., the most recent local solution and recent solutions of tunneling sub-problems that failed to achieve the optimum condition. Also, $\text{dist}(\mathbf{x}, \mathbf{s}_i)$ denotes the Eulerian distance.

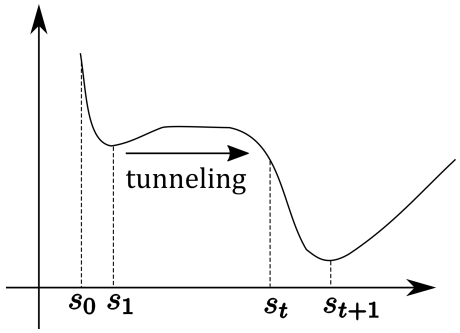

Figure 9.4: Tunneling approach of AMPGO algorithm [14].

9.2.4 Particle Swarm Optimization (PSO) method

The particle swarm optimization method was first proposed by Kennedy and Eberhart [93]. Motivated by the social behavior of bird flocks, this method can be used to find the minimum or maximum values of an objective function $f(\mathbf{X})$, where $\mathbf{X} = [x_1, x_2, ..., x_n]$ is a vector of variables, also known as a position vector. A swarm size is chosen in this method. The optimized solution is found using the cooperation of these swarm particles based on the communication among them.

The search movement for optimum solution of each particle for an iteration (shown in Fig. 9.5 comprises of a component of current velocity direction v_t^i, a movement component towards local or personal best solution from all the previous iterations $c_1\left(p_t^i - x_t^i\right)$ and a movement component towards global best , i.e. the best solution of all the particles in the swarm $c_2\left(g_t^i - x_t^i\right)$. The velocity for the next iteration $(t+1)$ for i^{th} particle of the swarm, represented by v_{t+1}^i is given by Eq. 9.35.

$$v_{t+1}^i = \omega v_t^i + c_1 r_1 \left(p_t^i - x_t^i\right) + c_2 r_2 \left(g_t^i - x_t^i\right). \tag{9.35}$$

Here, parameter ω is called inertia weight, c_1 is called cognitive learning factor and c_2 is called social learning factor. These three parameters control the contribution of each factor in a particle's movement. The numbers r_1 and r_2 are the random numbers in the range (0,1) and are used to avoid premature convergence. For this work, a swarm size of 20 with equal values to the parameters c_1 and c_2 is used.

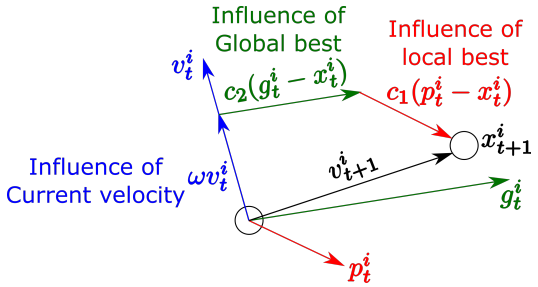

Figure 9.5: Movement of particles in PSO algorithm.

9.3 Results

Using the first approach, multiple sets of optimal Johnson-Cook parameters are obtained by both of the optimization algorithms. As an example, ten sets of optimal parameters for the machining condition 3 of Table 9.2 by AMPGO algorithm are given in Table 9.3. The variation of each parameter over the ten sets is quite large. For example, the parameter A varies from 449.5 MPa in set 1 to 658.3 MPa in set 10.

Table 9.3: Johnson-Cook parameters obtained using Approach 1 by AMPGO method (for Machining condition 3).

A (MPa)	B (MPa)	n	C	m
449.5	720.3	0.228	0.0160	0.922
471.8	720.8	0.233	0.0140	0.921
473.9	720.8	0.231	0.0130	0.935
479.4	719.9	0.234	0.0130	0.924
499.1	719.9	0.238	0.0110	0.929
508.9	719.6	0.241	0.0100	0.924
545.1	648.3	0.248	0.0120	0.951
567.8	623.5	0.254	0.0110	0.959
578.9	613.4	0.254	0.0100	0.978
658.3	507.6	0.277	0.0100	1.024

Using the second approach, where only C and m are varied, very close values of the Johnson-Cook parameters are obtained by each of the algorithms. The optimization is done ten times for each of the machining conditions to verify the uniqueness of the parameter set obtained by each algorithm, t. The variations in the obtained parameters are within $\pm 2\%$. The average value of ten optimizations for each of the parameters obtained by the AMPGO and PSO algorithm is given in Table 9.4 and Table 9.5 respectively.

Comparisons of the obtained values of the Johnson-Cook parameters C and m from the AMPGO and PSO algorithms are shown in Fig. 9.6 and 9.7 respectively. Red lines in the plots represent the range of the parameter provided as an input to the algorithm. The green line indicates the value reported in the literature [91]. The

Table 9.4: JC parameters obtained using Approach 2 by AMPGO.

Test no.	C	m
1	0.01343	0.9987
2	0.01342	0.9990
3	0.01345	0.9988
4	0.01347	0.9983
5	0.01337	0.9999
6	0.01346	0.9979
7	0.01349	0.9982
8	0.01353	0.9970
Jaspers and Dautzenberg [91]	0.0134	1

Table 9.5: JC parameters obtained using Approach 2 by PSO.

Test no.	C	m
1	0.01344	0.9986
2	0.01342	0.9990
3	0.01346	0.9986
4	0.01347	0.9982
5	0.01339	0.9997
6	0.01348	0.9975
7	0.01356	0.9970
8	0.01354	0.9969
Jaspers and Dautzenberg [91]	0.0134	1

results of the optimization algorithms match well with this green line.

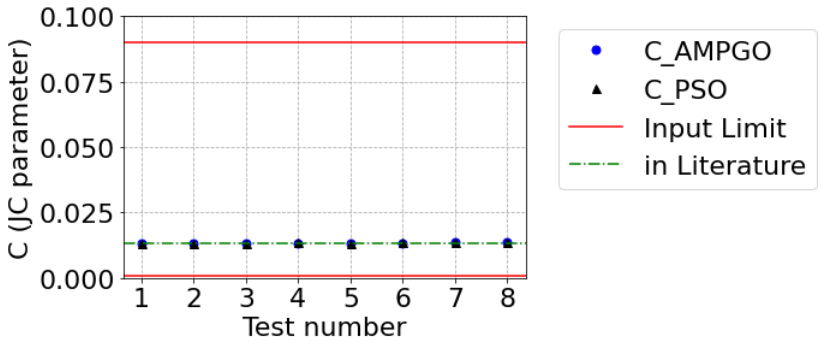

Figure 9.6: Comparison of Johnson Cook parameter C.

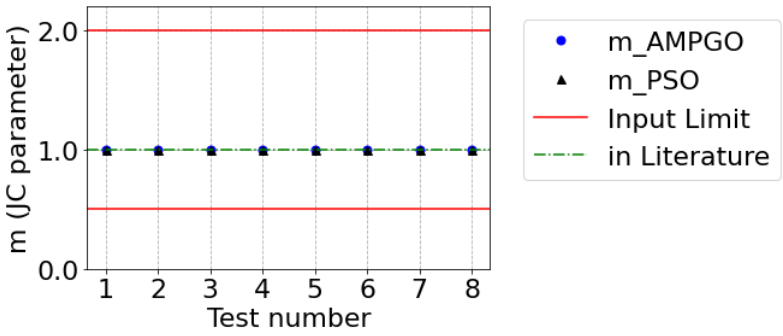

Figure 9.7: Comparison of Johnson Cook parameter m.

Table 9.6: Strain hardening term for Johnson-Cook parameters obtained using Approach 1 for the machining condition 3.

A (MPa)	B (Mpa)	n	ε_p	$A + B\varepsilon_p^n$
449.508	720.342	0.2276	0.6321	1098
471.753	720.800	0.2328	0.6321	1120
473.947	720.798	0.2306	0.6320	1122
479.400	719.891	0.2341	0.6321	1126
499.116	719.877	0.2376	0.6321	1145
508.910	719.630	0.2408	0.6321	1153
545.087	648.332	0.2482	0.6321	1124
567.799	623.450	0.2541	0.6321	1123
578.884	613.379	0.2539	0.6320	1125
658.250	507.556	0.2775	0.6321	1105

9.4 Discussion on the unique determination of Johnson-Cook parameters

In this section, the results of both the approaches used in this study are summarized. The reason for the non-unique determination of the Johnson-Cook parameters is also discussed.

9.4.1 Non-uniqueness of Johnson-Cook parameters while using Approach 1

As discussed in the Results section, multiple sets of values are obtained when all the five Johnson-Cook parameters are chosen as the target parameters to predict. To investigate further, the other machining parameters such as the temperature along the shear plane (AB) using these sets are calculated and compared in Table 9.7. The

Table 9.7: Other output variables using Approach 1 by AMPGO method.

ε_{AB}	$\dot{\varepsilon_{AB}}$ (1/s)	ε_{int}	$\dot{\varepsilon_{int}}$ (1/s)	T_{AB} (°C)	T_{int} (°C)	k_{AB} (MPa)	σ_N (MPa)	h (mm)	F_c (N)	F_t (N)	Chip ratio
0.63	11583	14.72	92995	292	1015	573.8	871.5	0.5	770.7	235.3	1.8
0.63	11566	14.68	92733	292	1014	573.9	871.6	0.5	770.7	235.3	1.8
0.63	11692	14.87	94064	292	1015	573.8	871.5	0.5	770.5	235.2	1.8
0.63	11590	14.70	92869	292	1014	573.9	871.6	0.5	770.7	235.3	1.8
0.63	11625	14.74	93150	292	1015	573.8	871.6	0.5	770.6	235.3	1.8
0.63	11578	14.66	92556	292	1014	573.9	871.6	0.5	770.8	235.4	1.8
0.63	12189	14.66	92549	292	1014	573.9	871.6	0.5	770.8	235.4	1.8
0.63	12401	14.60	92174	292	1014	573.9	871.6	0.5	770.8	235.4	1.8
0.63	12641	14.79	93519	292	1015	573.8	871.5	0.5	770.6	235.2	1.8
0.63	13882	14.68	92716	292	1014	573.9	871.6	0.5	770.7	235.3	1.8

variables of the objective function, i.e., the cutting force, chip ratio and the tool-chip interface temperature, agree for all ten sets. In fact, the value of all the other machining parameters, including the shear strain ε_{AB} and strain rate $\dot{\varepsilon}_{AB}$ and average temperature T_{AB} at shear plane AB match. This clearly shows the non-uniqueness of these parameters while using Approach 1.

To validate the claim of the non-unique determination of the Johnson-Cook parameter sets, the finite element simulations are done for the test case 2 using different parameter sets. A comparison of chip profile and cutting force is made. The plot comparing the cutting force is shown in Fig. 9.8. Also, the chip profile comparison is shown in Fig. 9.9. Clearly, the results obtained from the simulation using different Johnson-Cook parameter sets match closely.

9.4.2 Unique determination of Johnson-Cook parameters while using Approach 2

A unique set of Johnson-Cook parameters is obtained using the Approach 2, where the parameters A, B and n are determined using the tensile test experiment and the parameters C and m are determined using the inverse method.

The strain hardening term of the Johnson-Cook constitutive model is the term $\left(A + B\varepsilon_p^n\right)$. For a given value of strain ε_p, multiple sets of A, B, and n can be determined to produce the same combined value of strain hardening. This is verified

in Table 9.6 by calculating the strain hardening term for the ten parameter sets (shown in Table 9.3) obtained by the inverse method for the machining condition 3 of Table 9.2. The calculated values of the strain hardening term are approximately equal. This indicates the possibility of multiple sets of A, B, and n producing equal value of strain hardening term. Thus to obtain the Johnson-Cook parameters uniquely, a combined approach of experiment and inverse method can be followed. The parameters A, B and n can be determined using the tensile test experiment. The remaining two parameters C and m can be determined using the inverse method. This replaces the cumbersome experiments at multiple large strain rates and high temperatures with the simple orthogonal machining experiments.

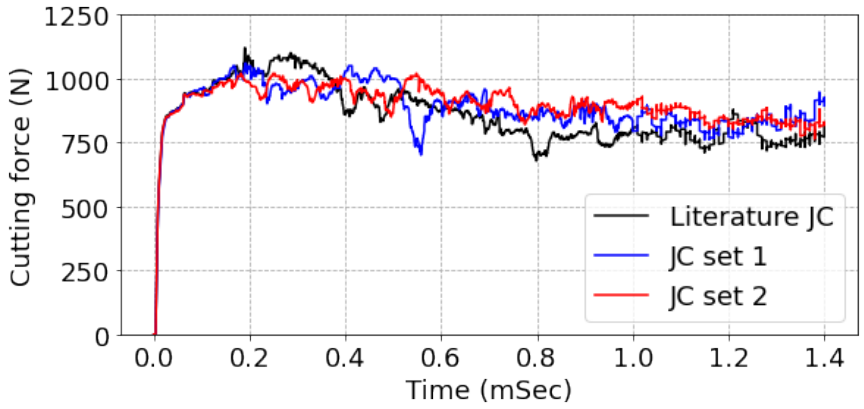

Figure 9.8: Comparison of cutting force using different JC parameter sets.

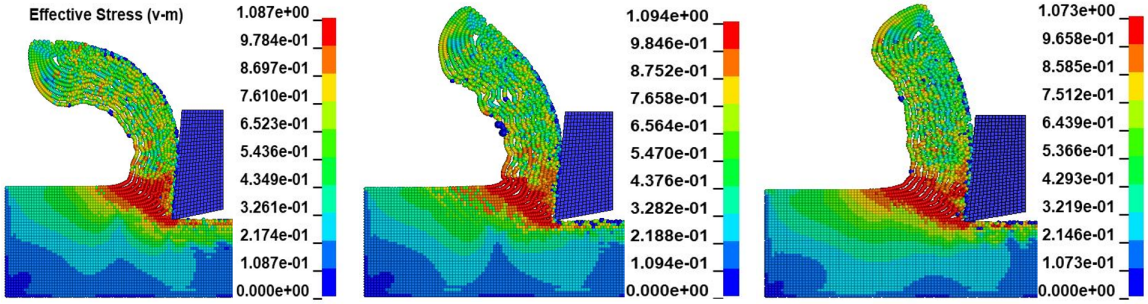

Figure 9.9: Comparison of chip profile using different JC parameter sets.

9.5 Conclusion

This work presents an inverse approach to determine the parameters of the Johnson-Cook constitutive model using a combination of analytical models, experiments, and optimization algorithms AMPGO and PSO. The following conclusions can be made:

1. When all the five parameters of the Johnson-Cook model are selected as the objective, multiple sets of values are predicted by the optimization algorithms (AMPGO and PSO) and the analytical extended Oxley model.

2. Results show that the Johnson-Cook parameters C and m can be determined with an acceptable degree of accuracy using only the cutting force, chip ratio, and tool-chip interface temperature as the variables of the objective function. The results of the tensile test experiment can be used to determine the three parameters A, B, and n.

3. The two optimization algorithms, AMPGO and PSO algorithms, converge to the correct values of the Johnson-Cook parameters even when large search domains are provided for each of the parameters.

CHAPTER 10: CONCLUSIONS AND FUTURE WORK

Modeling of turning operations using a coupled Finite Element (FE) and Smoothed Particle Hydrodynamics (SPH) method is presented in this dissertation. The coupled SPH-FE models use SPH particles in the high-deformation zone where machining takes place and finite elements in the low-deformation zones. The challenges associated with using the FE method such as mesh distortions and material separation modeling are easily handled by the SPH method. At the same time, the high computational times associated with SPH are reduced with the use of the FE mesh in the low deformation zones.

A fully-SPH model and a coupled SPH-FE machining model are developed in two dimensions. The results of these models are validated with the SPH model developed by Madaj [22]. The results of the coupled SPH-FE model are in close agreement with the full SPH model. However, the coupled SPH-FE model resulted in a significant reduction in the simulation time by approximately 40%. Machining conditions that are close to the orthogonal machining, such as thin wall turning, can be simulated with two-dimensional models.

Using the two-dimensional SPH model, a parametric study is conducted by varying computational parameters. These parametric studies enabled the identification of the optimal values for the parameters that lead to physically realistic results.

Using the benefit of the coupled SPH-FE model and the insight gained from the parametric study, a full-scale three-dimensional turning model is simulated. The primary results of interest are the forces and chip morphology. The three-dimensional model is required as the two-dimensional model under-predicted the cutting forces. The forces predicted by the three-dimensional model are considerably close to the

experimental values. The chip morphology also correlates with experiments in terms of the direction of the chip movement and the "long" continuous chips observed while turning Al6061. These models are beneficial in the design of chip breakers and guards for safety while machining in addition to enabling tool-wear and surface finish studies.

The three-dimensional machining models are extended to include the modulated tool path (MTP) machining and validated with experimental results. MTP machining is a technique to break the chips formed during turning by modulating the motion of the tool. Long chips produced during the conventional turning can affect the surface finish of the workpiece, cause tool damage, and even cause injuries to the operator. The simulated chips and cutting forces of MTP machining are compared with the results from the constant feed turning simulation. The advantages of MTP turning are demonstrated through these results. The MTP machining models can be used to optimize the tool path that results in the reduction of the tool wear and improvement of the machined surface.

Dynamic elements are incorporated into the three-dimensional turning models. The effect of these dynamic elements on the tool vibration and the cutting force is presented. These models have the potential to be used for studying machining stability for given sets of machining conditions.

The machining models used in this dissertation use the Johnson-Cook material model as the constitutive model. To eliminate the uncertainty associated with the material parameters in these models, an inverse approach for the unique determination of the parameters is presented. Unlike the other inverse approaches available in the open-literature, the proposed approach provides a methodology to determine each parameter uniquely. The parameters A, B and n can be determined using the tensile test experiments and the parameters C and n can be determined through the inverse approach using the data from the orthogonal machining experiments. The orthogonal machining experiments replace the expensive-to-conduct Split-Hopkinson Pressure

Bar tests in the determination of these parameters.

A summary of the studies conducted in this dissertation is shown in Figure 10.1.

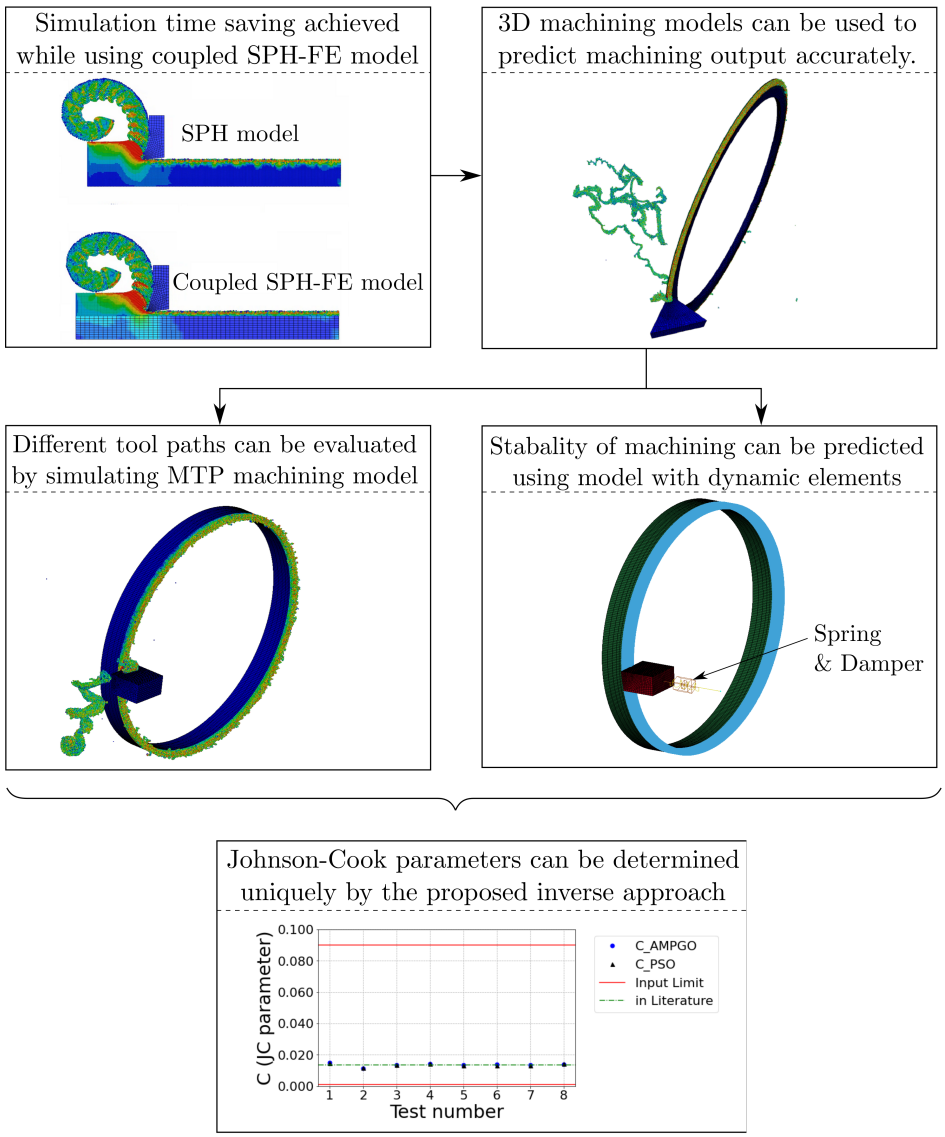

Figure 10.1: Summary of the studies conducted.

Future work could potentially focus on the following topics:

1. Other machining techniques such as vibration-assisted turning and interrupted turning can be modeled. Currently, these techniques are being studied using the experiments. Computational modeling can provide an efficient approach to optimize the parameters of these processes and improve the quality of the machined surface.

2. Diamond turning operation can be simulated using the coupled SPH-FE method. However, to reduce the computational time, a reduction of the diameter of the workpiece may be necessary.

3. Machining dynamics models can be validated with the experimental observations. These models have the potential to predict stability of the machining conditions.

4. The model can be utilized for designing cutting tools, chip breakers, and guards. This is particularly useful for the machining of hazardous materials where conducting experimental studies is unsafe.

5. This work can be extended to include other machining operations such as milling and drilling.

REFERENCES

[1] Tarek Mabrouki, François Girardin, Muhammad Asad, and Jean-François Rigal. Numerical and experimental study of dry cutting for an aeronautic aluminium alloy (A2024-T351). *International Journal of Machine Tools and Manufacture*, 48(11):1187–1197, 2008.

[2] Aluminum 6061-T6; 6061-T651. `http://www.matweb.com/search/datasheet_print.aspx?matguid=1b8c06d0ca7c456694c7777d9e10be5b`. (Accessed on 11/12/2020).

[3] Leonard E Schwer and CA Windsor. Aluminum plate perforation: a comparative case study using Lagrange with erosion, multi-material ALE, and smooth particle hydrodynamics. In *Seventh European LS-DYNA Conference, Stuttgart, Germany, June*, volume 10, 2009.

[4] GR Johnson and TJ Holmquist. Test data and computational strength and fracture model constants for 23 materials subjected to large strains, high strain rates, and high temperatures. *Los Alamos National Laboratory, LA-11463-MS*, 198, 1989.

[5] AISI 1026 Steel, cold drawn, 19-32 mm (0.75-1.25 in) round. `http://www.matweb.com/search/DataSheet.aspx?MatGUID=f3c08781eced413ebd167d9a9d1211f2&ckck=1`, . (Accessed on 12/29/2020).

[6] AISI 1026 Chemical Composition, AISI 1026 Mechanical Properties, AISI 1026 Heat Treatment. `https://www.steelgr.com/Steel-Grades/Carbon-Steel/aisi-1026.html`, . (Accessed on 12/29/2020).

[7] Shawoon Roy, Mohamed Trabia, Brendan O'Toole, Jagadeep Thota, Richard Jennings, Deepak Somasundarum, Melissa Matthes, Steven Becker, Edward

Daykin, Robert Hixson, et al. Plastic deformation of steel plates under high impact loading. Technical report, Nevada Test Site/National Security Technologies, LLC (United States), 2013.

[8] JD Seidt, A Gilat, JA Klein, and JR Leach. High strain rate, high temperature constitutive and failure models for EOD impact scenarios. In *Proceedings of the SEM Annual Conference & Exposition on Experimental and Applied Mechanics*, volume 15. Society for Experimental Mechanics, 2007.

[9] ASTM A36 Carbon Steel vs. SAE-AISI 1026 Steel: Makeitfrom.com. `https://www.makeitfrom.com/compare/ASTM-A36-SS400-S275-Structural-Carbon-Steel/SAE-AISI-1026-G10260-Carbon-Steel`. (Accessed on 05/29/2021).

[10] DI Lalwani, NK Mehta, and PK Jain. Extension of oxley's predictive machining theory for johnson and cook flow stress model. *Journal of Materials Processing Technology*, 209(12-13):5305–5312, 2009.

[11] H Ernst-ME Merchant and H Ernst. Chip formation, friction and high quality machined surfaces. *Sur Treat Metal*, pages 299–378, 1941.

[12] M Rubeo, Ryan Copenhaver, Saurabh Landge, T Schmitz, and NC Charlotte. Experimental platform for in-process metrology during orthogonal turning. In *American Society for Precision Engineering Annual Meeting, October*, pages 23–28, 2016.

[13] Peter Louis Brennan Oxley and Milton C Shaw. *Mechanics of machining: an analytical approach to assessing machinability*. John Wiley & Sons, 1990.

[14] Leon Lasdon, Abraham Duarte, Fred Glover, Manuel Laguna, and Rafael Martí. Adaptive memory programming for constrained global optimization. *Computers & operations research*, 37(8):1500–1509, 2010.

[15] Morteza Sadeghifar, Ramin Sedaghati, Walid Jomaa, and Victor Songmene. A comprehensive review of finite element modeling of orthogonal machining process: chip formation and surface integrity predictions. *The International Journal of Advanced Manufacturing Technology*, 96(9-12):3747–3791, 2018.

[16] Viktor P Astakhov and José C Outeiro. Metal cutting mechanics, finite element modelling. In *Machining*, pages 1–27. Springer, 2008.

[17] B Zhang and A Bagchi. Finite element simulation of chip formation and comparison with machining experiment. *Engineering for Industry*, 1994.

[18] TD Marusich and Modeling Ortiz. Modelling and simulation of high-speed machining. *International Journal for Numerical Methods in Engineering*, 38(21): 3675–3694, 1995.

[19] John T Carroll III and John S Strenkowski. Finite element models of orthogonal cutting with application to single point diamond turning. *International Journal of Mechanical Sciences*, 30(12):899–920, 1988.

[20] M Movahhedy, MS Gadala, and Y Altintas. Simulation of the orthogonal metal cutting process using an arbitrary lagrangian–eulerian finite-element method. *Journal of Materials Processing Technology*, 103(2):267–275, 2000.

[21] Jérôme Limido, Christine Espinosa, Michel Salaün, and Jean-Luc Lacome. SPH method applied to high speed cutting modelling. *International Journal of Mechanical Sciences*, 49(7):898–908, 2007.

[22] Martin Madaj and Miroslav Píška. On the SPH orthogonal cutting simulation of A2024-T351 alloy. *Procedia CIRP*, 8:152–157, 2013.

[23] Morten F Villumsen and Torben G Fauerholdt. Simulation of metal cutting using smooth particle hydrodynamics. *LS-DYNA Anwenderforum, C-III*, 17, 2008.

[24] Chinmay S Avachat and Harish P Cherukuri. A parametric study of the modeling of orthogonal machining using the smoothed particle hydrodynamics method. In *ASME 2015 International Mechanical Engineering Congress and Exposition*. American Society of Mechanical Engineers Digital Collection, 2015.

[25] Joseph R Davis. *ASM Handbook: Machining*, volume 16. ASM International, 1989.

[26] M Cocquilhat. Experiences sur la résistance utile produite dans le forage. In *Annales des Travaux Publics en Belgique*, volume 10, page 199, 1851.

[27] W. Hartig. *Handbuch der Maschinen*. 1873.

[28] Henri Edouard Tresca. *Mémoire sur le rabotage des métaux*. Imprimerie nationale, 1880.

[29] S Kobayashi and EG Thomsen. Some observations on the shearing process in metal cutting. *Journal of Engineering for industry*, 81(3):251–262, 1959.

[30] MG Stevenson and PLB Oxley. An experimental investigation of the influence of speed and scale on the strain-rate in a zone of intense plastic deformation. *Proceedings of the Institution of Mechanical Engineers*, 184(1):561–576, 1969.

[31] WB Palmer and PLB Oxley. Mechanics of orthogonal machining. *Proceedings of the Institution of Mechanical Engineers*, 173(1):623–654, 1959.

[32] PJ Arrazola, T Özel, D Umbrello, M Davies, and IS Jawahir. Recent advances in modelling of metal machining processes. *CIRP Annals*, 62(2):695–718, 2013.

[33] Tuğrul Özel and Erol Zeren. Finite element method simulation of machining of aisi 1045 steel with a round edge cutting tool. In *Proceedings of the 8th CIRP International Workshop on Modeling of Machining Operations*, pages 533–542, 2005.

[34] Siddharam Mane, Suhas S Joshi, Shyamprasad Karagadde, and Shiv G Kapoor. Modeling of variable friction and heat partition ratio at the chip-tool interface during orthogonal cutting of ti-6al-4v. *Journal of Manufacturing Processes*, 55: 254–267, 2020.

[35] JM Rodríguez, JM Carbonell, and Par Jonsen. Numerical methods for the modelling of chip formation. *Archives of Computational Methods in Engineering*, 27 (2):387–412, 2020.

[36] Jean-Loup Chenot, Marc Bernacki, Pierre-Olivier Bouchard, Lionel Fourment, Elie Hachem, and Etienne Perchat. Recent and future developments in finite element metal forming simulation. In *Proceedings of the 11th International Conference on Technology of Plasticity*, pages 265–293, 2014.

[37] Robert A Gingold and Joseph J Monaghan. Smoothed particle hydrodynamics: theory and application to non-spherical stars. *Monthly notices of the Royal Astronomical Society*, 181(3):375–389, 1977.

[38] Martin Heinstein and Dan Segalman. Simulation of orthogonal cutting with smooth particle hydrodynamics. Technical report, Sandia National Labs., Albuquerque, NM (United States), 1997.

[39] Christine Espinosa, Jean-Luc Lacome, Jérôme Limido, Michel Salaün, Catherine Mabru, and Rémy Chieragatti. Modelling high speed machining with the sph method. *10th International LS-DYNA Users Conference*, 2008.

[40] Yao Xi, Michael Bermingham, Gui Wang, and Matthew Dargusch. SPH/FE modeling of cutting force and chip formation during thermally assisted machining of Ti6Al4V alloy. *Computational Materials Science*, 84:188–197, 2014.

[41] Sampsa VA Laakso, Mathias Agmell, and Jan-Eric Ståhl. The mystery of missing feed force-the effect of friction models, flank wear and ploughing on feed force

in metal cutting simulations. *Journal of Manufacturing Processes*, 33:268–277, 2018.

[42] Madalina Calamaz, Dominique Coupard, and Franck Girot. A new material model for 2D numerical simulation of serrated chip formation when machining titanium alloy Ti-6Al-4V. *International Journal of Machine Tools and Manufacture*, 48(3-4):275–288, 2008.

[43] THC Childs and R Rahmad. Modifying strain-hardening of carbon steels for improved finite element simulation of orthogonal machining. *Proceedings of the Institution of Mechanical Engineers, Part B: Journal of Engineering Manufacture*, 224(5):721–732, 2010.

[44] Alaa Olleak and Tuğrul Özel. 3D finite element modeling based investigations of micro-textured tool designs in machining titanium alloy Ti-6Al-4V. *Procedia Manuf*, 10:536–545, 2017.

[45] Tugrul Ozel, I Llanos, J Soriano, and P-J Arrazola. 3D finite element modelling of chip formation process for machining Inconel 718: comparison of FE software predictions. *Machining Science and Technology*, 15(1):21–46, 2011.

[46] Ali Davoudinejad, Paolo Parenti, and Massimiliano Annoni. 3d finite element prediction of chip flow, burr formation, and cutting forces in micro end-milling of aluminum 6061-t6. *Frontiers of Mechanical Engineering*, 12(2):203–214, 2017.

[47] Mohamed NA Nasr, E-G Ng, and MA Elbestawi. A modified time-efficient fe approach for predicting machining-induced residual stresses. *Finite Elements in Analysis and Design*, 44(4):149–161, 2008.

[48] I Llanos, JA Villar, I Urresti, and PJ Arrazola. Finite element modeling of oblique machining using an arbitrary lagrangian–eulerian formulation. *Machining science and technology*, 13(3):385–406, 2009.

[49] Leon B Lucy. A numerical approach to the testing of the fission hypothesis. *The Astronomical Journal*, 82:1013–1024, 1977.

[50] MB Liu and GR Liu. Smoothed particle hydrodynamics (SPH): an overview and recent developments. *Archives of Computational Methods in Engineering*, 17(1): 25–76, 2010.

[51] JK Chen and JE Beraun. A generalized smoothed particle hydrodynamics method for nonlinear dynamic problems. *Computer Methods in Applied Mechanics and Engineering*, 190(1-2):225–239, 2000.

[52] MB Liu, GR Liu, and KY Lam. A one-dimensional meshfree particle formulation for simulating shock waves. *Shock Waves*, 13(3):201–211, 2003.

[53] Joe J Monaghan. Smoothed particle hydrodynamics. *Reports on Progress in Physics*, 68(8):1703, 2005.

[54] JJ Monaghan and RA Ginold. Shock Simulation by the Particle Method SPH. *Computational Physics*, 1983.

[55] Hallquist Jo. LS-DYNA theory manual. *LSTC, Livermore-California*, 2006.

[56] Paul W Cleary and Joseph J Monaghan. Conduction modelling using smoothed particle hydrodynamics. *Journal of Computational Physics*, 148(1):227–264, 1999.

[57] R Courant, KO Friedrichs, and H Lewy. Uber die partiellen differenzangleichungen der mathematisches. *Mathematische Annalen*, 100(1):32–74, 1928.

[58] Loup Verlet. Computer "experiments" on classical fluids. I. Thermodynamical properties of Lennard-Jones molecules. *Physical Review*, 159(1):98, 1967.

[59] LAMMPS Molecular Dynamics Simulator. `https://www.lammps.org/index.html`. (Accessed on 07/02/2021).

[60] Dualsphysics: A combined cuda and openmp implementation of the smoothed particle hydrodynamics method based on the advanced sphysics code. https://dual.sphysics.org/. (Accessed on 07/02/2021).

[61] Leapfrog integration - wikipedia. https://en.wikipedia.org/wiki/Leapfrog_integration. (Accessed on 07/03/2021).

[62] Time integration - welcome to the ls-dyna support site. https://www.dynasupport.com/tutorial/ls-dyna-users-guide/time-integration. (Accessed on 10/03/2020).

[63] GR Liu, MB Liu, and Shaofan Li. Smoothed particle hydrodynamics - a meshfree method. *Computational Mechanics*, 33(6):491–491, 2004.

[64] Suri Bala. Smoothing length in sph - d3view. https://www.d3view.com/smooth-length-in-sph/. (Accessed on 05/06/2021).

[65] Sangmin Lee and Jung-Wuk Hong. Parametric studies on smoothed particle hydrodynamic simulations for accurate estimation of open surface flow force. *International Journal of Naval Architecture and Ocean Engineering*, 12:85–101, 2020.

[66] Niclas Stenberg, Aldin Delić, and Thomas Björk. Using the sph method to easier predict wear in machining. *Procedia CIRP*, 58:317–322, 2017.

[67] Anhai Li, Jian Zang, and Jun Zhao. Effect of cutting parameters and tool rake angle on the chip formation and adiabatic shear characteristics in machining Ti-6Al-4V titanium alloy. *The International Journal of Advanced Manufacturing Technology*, 107(7):3077–3091, 2020.

[68] TS Assaid. Generation, measurement, and assessment of modulated tool-path

chip breaking in cnc turning processes. *Master's Thesis, UNC Charlotte, Charlotte, North Carolina*, 2010.

[69] David Andrew Tursky. *Chip Breaking Through Oscillating CNC Tool Paths and Its Effect on Chip Length, Tool Wear, and Machine Dynamics*. PhD thesis, University of North Carolina at Charlotte, 2010.

[70] Luke Berglind and John Ziegert. Chip breaking parameter selection for constant surface speed machining. In *ASME 2013 International Mechanical Engineering Congress and Exposition*. American Society of Mechanical Engineers Digital Collection, 2013.

[71] Luke Berglind and John Ziegert. Modulated tool path (MTP) machining for threading applications. *Procedia Manufacturing*, 1:546–555, 2015.

[72] Ryan Copenhaver, Mark A Rubeo, Steven Guzorek, Saurabh Landge, K Scott Smith, John Ziegert, and Tony L Schmitz. A fundamental investigation of modulated tool path turning mechanics. *Procedia Manufacturing*, 10:159–170, 2017.

[73] Tony L Schmitz and K Scott Smith. *Machining dynamics*. Springer, 2014.

[74] Gordon R Johnson and William H Cook. A constitutive model and data for metals subjected to large strains, high strain rates and high temperatures. In *Proceedings of the 7th International Symposium on Ballistics*, volume 21, pages 541–547. The Netherlands, 1983.

[75] Pedro J Arrazola and T Özel. Investigations on the effects of friction modeling in finite element simulation of machining. *International Journal of Mechanical Sciences*, 52(1):31–42, 2010.

[76] Tugrul Özel. The influence of friction models on finite element simulations of

machining. *International Journal of Machine Tools and Manufacture*, 46(5): 518–530, 2006.

[77] Herbert Kolsky. An investigation of the mechanical properties of materials at very high rates of loading. *Proceedings of the Physical Society. Section B*, 62(11): 676, 1949.

[78] John E Plumeri, Łukasz Madej, and Wojciech Z Misiolek. Constitutive modeling and inverse analysis of the flow stress evolution during high temperature compression of a new ze20 magnesium alloy for extrusion applications. *Materials Science and Engineering: A*, 740:174–181, 2019.

[79] Hemanth K Amarchinta, Ramana V Grandhi, Allan H Clauer, Kristina Langer, and David S Stargel. Simulation of residual stress induced by a laser peening process through inverse optimization of material models. *Journal of Materials Processing Technology*, 210(14):1997–2006, 2010.

[80] Ashkan Mahmoud Aghdami and Behnam Davoodi. An inverse analysis to identify the johnson-cook constitutive model parameters for cold wire drawing process. *Mechanics & Industry*, 21(5):527, 2020.

[81] Mathias Agmell, Aylin Ahadi, and Jan-Eric Ståhl. Identification of plasticity constants from orthogonal cutting and inverse analysis. *Mechanics of Materials*, 77:43–51, 2014.

[82] Jinqiang Ning, Vinh Nguyen, Yong Huang, Karl T Hartwig, and Steven Y Liang. Inverse determination of johnson-cook model constants of ultra-fine-grained titanium based on chip formation model and iterative gradient search. *The International Journal of Advanced Manufacturing Technology*, 99(5-8):1131–1140, 2018.

[83] Tuğrul Özel and Yiğit Karpat. Identification of constitutive material model parameters for high-strain rate metal cutting conditions using evolutionary computational algorithms. *Materials and Manufacturing Processes*, 22(5):659–667, 2007.

[84] Rocco Eisseler, Konstantin Drewle, Karl Christoph Grötzinger, and Hans-Christian Möhring. Using an inverse cutting simulation-based method to determine the johnson-cook material constants of heat-treated steel. *Procedia CIRP*, 77:26–29, 2018.

[85] Berend Denkena, Thilo Grove, Marc-André Dittrich, D Niederwestberg, and M Lahres. Inverse determination of constitutive equations and cutting force modelling for complex tools using Oxley's predictive machining theory. *Procedia CIRP 31 (2015)*, 31:405–410, 2015.

[86] Nikolaos E Karkalos and Angelos P Markopoulos. Determination of johnson-cook material model parameters by an optimization approach using the fireworks algorithm. *Procedia Manufacturing*, 22:107–113, 2018.

[87] J Pujana, PJ Arrazola, R M'saoubi, and H Chandrasekaran. Analysis of the inverse identification of constitutive equations applied in orthogonal cutting process. *International Journal of Machine Tools and Manufacture*, 47(14):2153–2161, 2007.

[88] Aviral Shrot and Martin Bäker. A study of non-uniqueness during the inverse identification of material parameters. *Procedia CIRP*, 1:72–77, 2012.

[89] Michael Storchak, Philipp Rupp, Hans-Christian Möhring, and Thomas Stehle. Determination of johnson–cook constitutive parameters for cutting simulations. *Metals*, 9(4):473, 2019.

[90] Donald R Lesuer, GJ Kay, and MM LeBlanc. Modeling large-strain, high-rate deformation in metals. Technical report, Lawrence Livermore National Lab., CA (US), 2001.

[91] SPFC Jaspers and JH Dautzenberg. Material behaviour in conditions similar to metal cutting: flow stress in the primary shear zone. *Journal of Materials Processing Technology*, 122(2-3):322–330, 2002.

[92] G Boothroyd. Temperatures in orthogonal metal cutting. *Proceedings of the Institution of Mechanical Engineers*, 177(1):789–810, 1963.

[93] Russell Eberhart and James Kennedy. Particle Swarm Optimization. In *Proceedings of the IEEE International Conference on Neural Networks*, volume 4, pages 1942–1948. Citeseer, 1995.

APPENDIX A: DERIVATION OF SOME SPH EQUATIONS

A.1 Kernel approximation of Gradient

The kernel approximation of the gradient of a scalar field $f(\mathbf{r})$ is calculated using the derivative of the smoothing kernel and it's functional value. It is given by

$$\langle \nabla_{\mathbf{r}^a} f(\mathbf{r}^a) \rangle = \sum_{j=1}^{N} \frac{m^b}{\rho^b} f(\mathbf{r}^b) \nabla_{\mathbf{r}^a} W(\mathbf{r}^{ab}, h). \tag{A.1}$$

Alternate forms of the kernel approximation of the gradient are obtained using the identity

$$\nabla(f\rho^n) = nf\rho^{n-1}\nabla\rho + \rho^n \nabla f. \tag{A.2}$$

Upon solving for ∇f from Eq. (A.2), we obtain

$$\nabla f = \frac{1}{\rho^n}[\nabla(f\rho^n) - nf\rho^{n-1}\nabla\rho]. \tag{A.3}$$

Combining Eq. (A.1) and Eq. (A.3)

$$\langle \nabla f(\mathbf{r}^a) \rangle = \frac{1}{(\rho^a)^n} \left[\sum_{b=1}^{N} m^b [f(\mathbf{r}^b)(\rho^b)^{n-1} - nf(\mathbf{r}^a)(\rho^a)^{n-1}] \nabla W(\mathbf{r}^{ab}, h) \right]. \tag{A.4}$$

Putting $n = 1$ in Eq. (A.4) gives the anti-symmetric form.

$$\langle \nabla f(\mathbf{r}^a) \rangle = \frac{1}{\rho^a} \left[\sum_{b=1}^{N} m^b [f(\mathbf{r}^b) - f(\mathbf{r}^a)] \nabla W(\mathbf{r}^{ab}, h) \right]. \tag{A.5}$$

Putting $n = -1$ in Eq. (A.4) gives the symmetric form.

$$\langle \nabla f(\mathbf{r}^a) \rangle = \rho^a \left[\sum_{b=1}^{N} m^b \left(\frac{f(\mathbf{r}^b)}{(\rho^b)^2} + \frac{f(\mathbf{r}^a)}{(\rho^a)^2} \right) \nabla W(\mathbf{r}^{ab}, h) \right]. \tag{A.6}$$

A.2 Kernel approximation of Divergence

Similar to the calculation of the gradient, the kernel approximation of the divergence of a vector field $\mathbf{F}(\mathbf{r})$ is calculated using the derivative of the smoothing kernel and its functional value. This approach is computatiaonally advantageous since functional derivatives are not required for calculating the divergence. The derivation of the kernel approximation of the divergence of a function $\mathbf{F}$ at position $\mathbf{r_a}$ is given below.

$$\begin{aligned}
\langle \nabla_{\mathbf{r}^a} \cdot \mathbf{F}(\mathbf{r}^a) \rangle &= \int_\Omega W(\mathbf{r}^{ab}, h) \nabla_{\mathbf{r}^b} \cdot \mathbf{F}(\mathbf{r}^b)\, \mathrm{d}\Omega_{\mathbf{r}^b} \\
&= \int_\Omega \nabla_{\mathbf{r}^b} \cdot [W(\mathbf{r}^{ab}, h)\mathbf{F}(\mathbf{r}^b)]\, \mathrm{d}\Omega_{\mathbf{r}^b} - \int_\Omega \nabla_{\mathbf{r}^b} W(\mathbf{r}^{ab}, h) \cdot \mathbf{F}(\mathbf{r}^b)\, \mathrm{d}\Omega_{\mathbf{r}^b} \\
&= \int_S W(\mathbf{r}^{ab}, h)\mathbf{F}(\mathbf{r}^b) \cdot \mathbf{n}\, \mathrm{d}S - \int_\Omega \nabla_{\mathbf{r}^b} W(\mathbf{r}^{ab}, h) \cdot \mathbf{F}(\mathbf{r}^b)\, \mathrm{d}\Omega_{\mathbf{r}^b} \\
&= 0 - \int_\Omega \nabla_{\mathbf{r}^b} W(\mathbf{r}^{ab}, h) \cdot \mathbf{F}(\mathbf{r}^b)\, \mathrm{d}\Omega_{\mathbf{r}^b} \\
&= \int_\Omega \nabla_{\mathbf{r}^a} W(\mathbf{r}^{ab}, h) \cdot \mathbf{F}(\mathbf{r}^b)\, \mathrm{d}\Omega_{\mathbf{r}^b} \\
&= \sum_{j=1}^{N} \frac{m^b}{\rho^b} \mathbf{F}(\mathbf{r}^b) \cdot \nabla_{\mathbf{r}^a} W(\mathbf{r}^{ab}, h).
\end{aligned} \tag{A.7}$$

The divergence theorem is used in the third step to convert the volume integral to a surface integral. In the fourth step, the first integral equals zero because of the compact support property of the smoothing kernel. The derivative of W is anti-symmetric with respect to $\mathbf{r}^a$ and $\mathbf{r}^b$. This flips the sign of the second integral in the fourth step.

A.3 SPH form of Stress work term

In this section, the SPH form of stress work term used in the conservation of energy equation and given by

$$< \frac{\boldsymbol{\sigma}}{\rho} : (\nabla \otimes \mathbf{v}) >= \frac{1}{2} \sum_{b=1}^{N} m^b \left(\frac{p^a}{(\rho^a)^2} + \frac{p^b}{(\rho^b)^2} \right) v_j^{ab} \frac{\partial W^{ab}}{\partial r_j^a} \; + \frac{\mu^a}{2\rho^a} \varepsilon_{ij}^a \varepsilon_{ij}^a \tag{A.8}$$

is derived. The total stress tensor $\boldsymbol{\sigma}$ consists of isotropic pressure p and shear stress $\boldsymbol{\tau}$ and is given by

$$\sigma_{ij} = -p\delta_{ij} + \tau_{ij}. \tag{A.9}$$

For a Newtonian fluid, shear stress is directly proportional to the shear strain rate and is given by

$$\tau_{ij} = \mu\epsilon_{ij}. \tag{A.10}$$

Here, μ is dynamic viscosity and $\boldsymbol{\epsilon}$ is shear strain rate.

Using Eqs. (A.9) and (A.10), we get

$$\frac{\boldsymbol{\sigma}}{\rho} : (\text{grad } \mathbf{v}) = -\frac{p}{\rho}\frac{\partial \mathbf{v}_i}{\partial \mathbf{r}_i} + \frac{\mu}{2\rho}\epsilon_{ij}\epsilon_{ij}. \tag{A.11}$$

From the SPH form of the conservation of mass equation, we have

$$< -\frac{p}{\rho}\frac{\partial \mathbf{v}_i}{\partial \mathbf{r}_i} > = \frac{p^a}{(\rho^a)^2}\sum_{b=1}^{N} m^b \mathbf{v}_i^{ab}\ \frac{\partial W^{ab}}{\partial r_i^a}. \tag{A.12}$$

From the product rule of differentiation, we have that

$$-\frac{p}{\rho}\frac{\partial \mathbf{v}_i}{\partial \mathbf{r}_i} = -\frac{\partial}{\partial \mathbf{r}_i}\left(\frac{p\mathbf{v}_i}{\rho}\right) + \mathbf{v}_i\frac{\partial}{\partial \mathbf{r}_i}\left(\frac{p}{\rho}\right). \tag{A.13}$$

This combined with Eq. (A.12) leads to

$$< -\frac{p}{\rho}\frac{\partial \mathbf{v}_i}{\partial \mathbf{r}_i} > = -\sum_{b=1}^{N} m^b \frac{p^b}{(\rho^b)^2}\mathbf{v}_i^b\frac{\partial W^{ab}}{\partial r_i^a} + \mathbf{v}_i^a\sum_{b=1}^{N} m^b\frac{p^b}{(\rho^b)^2}\frac{\partial W^{ab}}{\partial r_i^a} \tag{A.14}$$

or

$$< -\frac{p}{\rho}\frac{\partial \mathbf{v}_i}{\partial \mathbf{r}_i} > = \sum_{b=1}^{N} m^b \frac{p^b}{(\rho^b)^2}\mathbf{v}_i^{ab}\ \frac{\partial W^{ab}}{\partial r_i^a}. \tag{A.15}$$

Combining this result with Eq. (A.11) leads to Eq. (A.8).

A.4 SPH form of rate of change of Thermal energy

The rate of change of thermal energy in the absence of heat sources or sinks is given by

$$\rho \frac{DQ}{Dt} = \nabla \cdot (k \nabla T). \tag{A.16}$$

The SPH form of this equation is obtained by first deriving an integral approximation of the Laplacian of a function. This approximation is combined with the particle approximation to derive the final SPH form. The derivation is presented below.

Integral approximation form of the Laplacian of a function: Below is an Integral approximation form of the Laplacian of a function $f(\mathbf{r})$.

$$\nabla^2 f(\mathbf{r}^a) = 2 \int_\Omega \frac{f(\mathbf{r}^a) - f(\mathbf{r}^b)}{\mid \mathbf{r}^a - \mathbf{r}^b \mid^2} (\mathbf{r}^a - \mathbf{r}^b) \cdot \nabla W(\mathbf{r}^{ab}, h) \, d\Omega_{\mathbf{r}^b}. \tag{A.17}$$

This equation can be derived using the Taylor series expansion of a vector field and the properties of the kernel function. For ease of understanding, the derivation is presented for one-dimensional domain. The result can be generalized for three dimensions to obtain Eq. (A.17). The Taylor series expansion of the function $f(x^b)$ about x^a provides

$$f(x^b) - f(x^a) = (x^b - x^a) \frac{\partial f}{\partial x}\Big|_{x=x^a} + \frac{1}{2}(x^b - x^a)^2 \frac{\partial^2 f}{\partial x^{a2}}\Big|_{x=x^a} + \mathcal{O}[(x^a - x^b)^3]. \tag{A.18}$$

Next, the following operations are performed on Eq. (A.18):

1. multiply both sides of the equation by

$$\frac{(x^a - x^b) \, \nabla_a W(x^a - x^b, h)}{\mid x^a - x^b \mid^2},$$

2. denote $(x^a - x^b)$ by x^{ab} and $\nabla_a W(x^a - x^b, h)$ by $\nabla_a W^{ab}$,

3. ignore the higher order terms of the order $\mathcal{O}[(x^a - x^b)^3]$ and

4. integration over the domain.

The integral approximation form is derived after applying the above operations.

$$\begin{aligned}
&\int \Big[f(x^b) - f(x^a)\Big] \, \frac{x^{ab} \, \nabla_a W^{ab}}{\mid x^{ab} \mid^2} \, dx^b \\
&= -\int \frac{\partial f}{\partial x}\Big|_{x=x^a} x^{ab} \, \frac{x^{ab} \, \nabla_a W^{ab}}{\mid x^{ab} \mid^2} \, dx^b + \int \frac{1}{2} \, \frac{\partial^2 f}{\partial x^{a2}}\Big|_{x=x^a} (x^{ab})^2 \, \frac{x^{ab} \, \nabla_a W^{ab}}{\mid x^{ab} \mid^2} \, dx^b \\
&= -\frac{\partial f}{\partial x}\Big|_{x=x^a} \int \nabla_a W^{ab} \, dx^b + \frac{1}{2} \, \frac{\partial^2 f}{\partial x^{a2}}\Big|_{x=x^a} \int x^{ab} \, \nabla_a W^{ab} \, dx^b.
\end{aligned} \tag{A.19}$$

Since W^{ab} is an even function of x, ∇W^{ab} is an odd function. Therefore, $\int \nabla W^{ab} \, dx^b$ equals zero. The second integral can be simplified as below.

$$\begin{aligned}
\int x^{ab} \, \nabla_a W^{ab} \, dx^b &= -\int x^{ab} \, \nabla_b W^{ab} \, dx^b \\
&= -\int \nabla_b (x^{ab} W^{ab}) \, dx^b + \int W^{ab} \frac{d(x^a - x^b)}{dx^b} \, dx^b \\
&= 0 - \int W^{ab} \, dx^b \\
&= -1.
\end{aligned} \tag{A.20}$$

The first integral in the second step equals zero as $x^{ab} W^{ab}$ is an odd function. The integral $\int W^{ab} \, dx^b$ equals 1 due to the Normalization condition of the kernel function. Putting Eq. (A.20) into the Eq. (A.19) and then simplifying, we get the following Integral approximation for one-dimensional domain.

$$\frac{\partial^2 f}{\partial x^{a2}} = 2 \int \frac{f(x^a) - f(x^b)}{\mid x^{ab} \mid^2} x^{ab} \, \nabla_a W^{ab} \, dx^b. \tag{A.21}$$

The Eq. (A.21) can be generalized for three dimensions to obtain Eq. (A.17). The particle approximation form of the Eq. (A.17) is given by

$$< \nabla^2 f(\mathbf{r}^a) >= 2 \sum_{b=1}^{N} \frac{m^b}{\rho^b} \frac{f(\mathbf{r}^a) - f(\mathbf{r}^b)}{\mid \mathbf{r}^{ab} \mid^2} \mathbf{r}^{ab} \cdot \nabla W(\mathbf{r}^{ab}, h). \tag{A.22}$$

We derive the SPH form of Eq. (A.16) using the identity,

$$\nabla \cdot (k\nabla T) = \frac{1}{2}\big[\nabla^2(kT) - T\nabla^2 k + k\nabla^2 T\big]. \tag{A.23}$$

Writing all the Laplacian terms on the right hand side of the Eq. (A.23) in the particle approximation form using Eq. (A.22) and on simplification, the SPH form of rate of thermal energy Q^a can be shown to be

$$< Q^a > = \sum_{b=1}^{N} \frac{m^b}{\rho^a \rho^b} \frac{(k^a + k^b)(T^a - T^b)}{\mid \mathbf{r}^{ab} \mid^2} \mathbf{r}^{ab} \cdot \nabla W^{ab}. \tag{A.24}$$